

1

2

AEOLIAN SEDIMENT AVAILABILITY AND TRANSPORT

3

BAS HOONHOUT

4

“thesis” — 2016/12/13 — 10:12 — page ii — #2

4

5 Aeolian Sediment Availability and Transport © 2016, Bas Hoonhout

6 ISBN: XXX-XX-XXXX-XXX-X

7

8

AEOLIAN SEDIMENT AVAILABILITY AND TRANSPORT

9

PROEFSCHRIFT

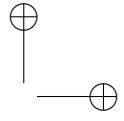
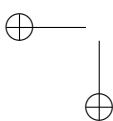
10 ter verkrijging van de graad van doctor
11 aan de Technische Universiteit Delft,
12 op gezag van de Rector Magnificus prof. ir. K.Ch.A.M. Luyben;
13 voorzitter van het College voor Promoties,
14 in het openbaar te verdedigen op
15 donderdag 16 maart 2016 om 15:00 uur.

16

door

17

Bastiaan Martin HOONHOUT
18 civiel technisch ingenieur
19 geboren te Amsterdam



²¹ This dissertation has been approved by the promotor prof. dr. ir. M.J.F. Stive and
²² copromotor dr. ir. S. de Vries.

²³ Composition of the doctoral committee:

Rector Magnificus	Chairman
prof. dr. ir. M.J.F. Stive	Delft University of Technology
dr. ir. S. de Vries	Delft University of Technology

²⁴ Independent members:

prof. dr. ir. A.J.H.M. Reniers	Delft University of Technology
prof. dr. ir. A.W. Heemink	Delft University of Technology
prof. dr. ir. J.A. Roelvink	UNESCO-IHE
prof. dr. ir. B.G. Ruessink	Utrecht University
dr. P. Ruggiero	Oregon State University

²⁵ Dr. ir. J. S. M. van Thiel de Vries has contributed as supervisor greatly to the realization
²⁶ of this research.

²⁷ This research was funded by the ERC-Advanced Grant 291206 – Nearshore Monitoring
²⁸ and Modeling (NEMO) and Deltares.

29 CONTENTS

30	1	INTRODUCTION	1
31	1.1	Motivation	1
32	1.2	Research objectives	3
33	1.3	Thesis outline	4
34	i	FIELD DATA	7
35	2	LARGE SCALE SEDIMENT BUDGETS	9
36	2.1	Introduction	9
37	2.2	Field Site	10
38	2.3	Methodology	11
39	2.3.1	Topographic measurements	14
40	2.3.2	Zonation	14
41	2.3.3	Spatial variations in porosity	16
42	2.4	Results	18
43	2.4.1	Morphological change and porosity	18
44	2.4.2	Aeolian sediment budgets	19
45	2.4.3	Alongshore variation	21
46	2.5	Discussion	21
47	2.5.1	Sources of inaccuracies	22
48	2.5.2	Beach armoring	24
49	2.5.3	Mega nourishments as coastal protection	25
50	2.6	Conclusions	26
51	3	SMALL SCALE SEDIMENT TRANSPORT	27
52	3.1	Introduction	27
53	3.2	Field Site	28
54	3.3	Methodology	30
55	3.3.1	Equipment	30
56	3.3.2	Deployments	32
57	3.3.3	Data analysis	33
58	3.4	Results	34
59	3.4.1	Relation between sediment transport and wind speed and water level	34
60	3.4.2	Wind direction and sediment source areas	36
61	3.4.3	Spatial gradients in sediment transport	38
62	3.4.4	Fetch vs. sediment availability	41
63	3.5	Discussion	41
64	3.6	Conclusions	44
66	ii	NUMERICAL MODELING	47
67	4	NUMERICAL MODEL	49
68	4.1	Introduction	49
69	4.2	Model Challenges: Bed Surface Properties	51
70	4.2.1	Temporal Variations in Bed Surface Properties	52

71	4.2.2 Spatial Variations in Bed Surface Properties	52
72	4.3 Model Concepts: Sediment Availability, Saturated Transport and En-	
73	trainment	53
74	4.4 Model Description	55
75	4.4.1 Advection Scheme	55
76	4.4.2 Multi-fraction Erosion and Deposition	56
77	4.4.3 Simulation of Sediment Sorting and Beach Armoring	58
78	4.4.4 Simulation of the Emergence of Non-erodible Roughness Ele-	
79	ments	59
80	4.4.5 Simulation of the Hydraulic Mixing, Infiltration and Evaporation	61
81	4.5 Results	61
82	4.5.1 Prototype cases	61
83	4.5.2 Wind tunnel experiments	66
84	4.5.3 Sensitivity	69
85	4.6 Discussion	71
86	4.6.1 Parameterization	71
87	4.6.2 Calibration	72
88	4.6.3 Validation	73
89	4.7 Conclusions	73
90	5 SAND MOTOR HINDCAST	75
91	5.1 Introduction	75
92	5.2 Field Site	76
93	5.3 Model approach	78
94	5.3.1 Reference model	78
95	5.3.2 Schematization	80
96	5.3.3 Calibration	83
97	5.4 Results	86
98	5.5 Discussion	91
99	5.5.1 Seasonal and local variations in sedimentation and erosion . . .	91
100	5.5.2 Beach armoring, sediment availability and the shear velocity	
101	threshold	92
102	5.6 Conclusions	93
103	iii DISCUSSION AND CONCLUSIONS	95
104	6 DISCUSSION	97
105	7 CONCLUSIONS	101
106	iv APPENDICES	105
107	A THEORETICAL SEDIMENT TRANSPORT VOLUMES	107
108	B NUMERICAL IMPLEMENTATION	109
109	B.1 Advection equation	109
110	B.2 Implicit solver	113
111	B.3 Shear velocity threshold	114
112	B.3.1 Moisture content	114
113	B.3.2 Roughness elements	115
114	B.3.3 Salt content	115
115	B.3.4 Masks	116

116	B.4 Basic Model Interface (BMI)	116
117	C MODEL SETTINGS	119
118	BIBLIOGRAPHY	121
119	ACKNOWLEDGMENTS	131
120	CURRICULUM VITAE	133
121	PUBLICATIONS	135
122	COLOPHON	137

"thesis" — 2016/12/13 — 10:12 — page iv — #8

123 DEFINITIONS

124 WIND TRANSPORT CAPACITY [kg/m/s] Transport capacity of the wind over an ide-
125 alized bed. The wind transport capacity is an upper limit of the (sediment)
126 transport capacity that includes the influence of bed surface properties.

127 (SEDIMENT) TRANSPORT CAPACITY [kg/m/s] Transport capacity of the wind over
128 a given bed. The (sediment) transport capacity accounts for the impact velocity
129 threshold. The (sediment) transport capacity is an upper limit of the actual
130 sediment transport.

131 EQUILIBRIUM SEDIMENT TRANSPORT Sediment transport capacity.

132 SATURATED SEDIMENT TRANSPORT Sediment transport capacity.

133 VELOCITY THRESHOLD [kg/m/s] Impact velocity threshold at which sediment trans-
134 port is sustained over a given bed. The threshold depends on bed surface prop-
135 erties that may hamper saltation, e.g. roughness, moist, salt, and represents the
136 difference between the wind and (sediment) transport capacity.

137 SEDIMENT AVAILABILITY [kg/m²] Sediment currently available for entrainment
138 (following Kocurek and Lancaster, 1999). The sediment availability includes
139 the fluid velocity threshold at which sediment transport is initiated. Sediment
140 availability may result in sediment supply if wind is sufficient.

141 SEDIMENT ENTRAINMENT [kg/m²/s] Entrainment of currently available sediment
142 by the wind and contributing to the sediment supply.

143 SEDIMENT SUPPLY [kg/m/s] Transport of entrained sediment from one location to
144 another, e.g. from marine sources to intertidal beach or from intertidal beach to
145 dunes.

146 TRANSPORT-LIMITED Transport is determined by the wind transport capacity. An
147 increase in wind speed will result in an increase in sediment transport as long
148 as sediment is still available. If insufficient sediment is available, the coastal
149 system becomes availability-limited.

150 AVAILABILITY-LIMITED Transport is determined by the availability of aeolian sed-
151 iment. An increase in wind speed will not result in an increase in sediment
152 transport as no additional sediment is available. A decrease in wind speed can
153 result in a transport-limited coastal system as the sediment availability might be
154 able to fulfill the demand from the reduced wind.

155 SUPPLY-LIMITED Availability-limited.

156 FETCH-LIMITED Transport is determined by the available fetch and therefore a wider
157 beach or more oblique wind will result in an increase in sediment transport. In

158 this thesis fetch is only considered a limiting factor on an idealized bed with
159 maximum sediment availability (i.e. flat, dry, loose and homogeneous). The
160 coastal system is considered fetch-limited if and only if the available fetch is
161 shorter than the fetch necessary for the development of a saturated saltation
162 cascade in these idealized conditions. In all other cases where the available fetch
163 influences the sediment transport, the coastal system is considered availability-
164 limited.

165 **SEDIMENT SORTING** Spatial sorting of (sandy) sediment, either horizontally or ver-
166 tically, due to differences in (sediment) transport capacity between sediment
167 fractions.

168 **BEACH ARMORING** Emergence of non-erodible roughness elements from the bed
169 that shelter (sandy) sediment from wind erosion, resulting in spatiotemporal
170 differences in sediment availability.

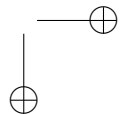
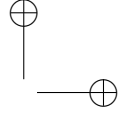
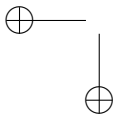
¹⁷¹ ACRONYMS

2DH	Two-Dimensional in a Horizontal plane
2DV	Two-Dimensional in a Vertical plane
ATV	All-Terrain Vehicle
AEOLIS	Aeolian sediment transport with Limited Supply
DN	Deployment Number
KNMI	Koninklijk Nederlands Meteorologisch Instituut
¹⁷² MCMC	Markov Chain Monte Carlo
MSL	Mean Sea Level
MEGAPEX	Mega Perturbation EXperiment
NEMO	Nearshore Modeling and Monitoring
R²	R-squared or Coefficient of Determination
RMSE	Root Mean Square Error
RTK-GPS	Real-Time Kinematic Global Positioning System

"thesis" — 2016/12/13 — 10:12 — page viii — #12

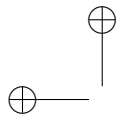
¹⁷³ SYMBOLS

Symbol	Units	Description
α	-	Factor to convert from wind velocity to shear velocity.
β	-	Ratio between drag coefficients of bare surface and roughness elements.
θ_u	-	Wind direction.
Γ	-	Implicitness parameter.
γ	-	Maximum wave height over depth ratio.
ζ	-	Bed interaction factor.
η	m+MSL	Still water level.
$\hat{\eta}$	m+MSL	Local water level.
κ	-	Von Kármán constant.
λ	-	Roughness density.
ξ	-	Surf similarity parameter.
ρ_a	kg/m ³	Air density.
ρ_p	kg/m ³	Grain density.
ρ_w	kg/m ³	Water density.
σ	-	Ratio between surface area and frontal area of roughness elements.
Φ	kg/m/s	Space-integrated entrainment function.
ϕ	kg/m ² /s	Entrainment function.
Ψ	kg/s	Sediment transport potential.
A	-	Empirical coefficient.
A_c	m ²	Surface area of control area.
C	-	Empirical coefficient to account for grain size distribution width.
C_c	kg/m ³	Sediment concentration in the air as used by de Vries et al. (2014b) . Relates to c as $c = h C_c$.
c	kg/m ²	Sediment concentration in the air.
c_{sat}	kg/m ²	Saturated sediment concentration in the air.
D	kg/m ²	Total deposition.
D_n	m	Reference median grain size (250 µm).
d	m	Water depth.
d_{50}	m	Median grain size.
d_n	m	Nominal grain size.
E	kg/m ²	Total erosion.
E_v	m/s	Evaporation rate.
F	m	Available fetch.
\hat{F}	m	Effective fetch.
F_c	m	Critical fetch.
$f_{\Delta z_d}$	-	Depth of disturbance factor.

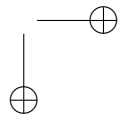
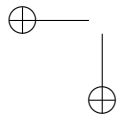
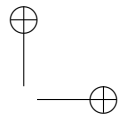


Symbol	Units	Description	(continued)
f_{θ_u}	-	Factor to include wind direction in sediment transport capacity.	
$f_{u_{*th},M}$	-	Factor to include the influence of moisture to the shear velocity threshold u_{*th} .	
$f_{u_{*th},R}$	-	Factor to include the influence of roughness elements to the shear velocity threshold u_{*th} . Relates to R_t as $R_t = \frac{1}{f_{u_{*th},R}}$.	
$f_{u_{*th},S}$	-	Factor to include the influence of salt to the shear velocity threshold u_{*th} .	
g	m/s^2	Gravitational constant.	
H	m	Offshore wave height.	
\hat{H}	m	Local wave height.	
h	m	Height of saltation layer.	
i	-	Cross-shore grid index.	
j	-	Alongshore grid index.	
K^+	-	Hydrodynamic addition mask.	
K^\times	-	Hydrodynamic multiplication mask.	
k	-	Grain size fraction index.	
k_0	-	Index of smallest non-erodible grain size fraction.	
l	-	Diagonal index.	
m	-	Factor to account for difference between mean and maximum shear stress.	
m_a	kg/m^2	Sediment availability.	
n	-	Time step index.	
n_k	-	Number of grain size fractions.	
n_{pc}	-	Number of counted particles.	
n_x	-	Number of grid cells in cross-shore direction.	
n_y	-	Number of grid cells in alongshore direction.	
p	-	Porosity.	
p_g	kg/kg	Geotechnical mass content of water.	
p_s	mg/g	Salt content.	
p_v	m^3/m^3	Volumetric water content.	
Q	m^3	Cumulative sediment transport capacity.	
q	kg/m/s	Sediment transport rate.	
q_{sat}	kg/m/s	Saturated sediment transport rate.	
R	m	Wave runup height.	
R_t	-	Ratio between velocity threshold on bare surface $u_{*th,S}$ and on surface including roughness elements $u_{*th,R}$.	
S_k	-	Degree of saturation of grain size fraction k .	
\hat{S}_k	-	Effective degree of saturation of grain size fraction k , including the bed interaction parameter ζ .	
T	s	Adaptation time scale in advection equation.	
t	s	Time.	
Δt^n	s	Size of time step n .	
u_*	m/s	Shear velocity.	
u_z	m/s	Wind velocity at height z .	

Symbol	Units	Description	(continued)
$u_{*th,R}$	m/s	Shear velocity threshold of surface including roughness elements.	
$u_{*th,S}$	m/s	Shear velocity threshold of bare surface.	
u_{*th}	m/s	Shear velocity threshold.	
u_{th}	m/s	Wind velocity threshold.	
$u_{z,x}$	m/s	Wind velocity component in x-direction and at height z .	
$u_{z,y}$	m/s	Wind velocity component in y-direction and at height z .	
V	m^3	Sediment volume.	
$V_{40\%}$	m^3	Sediment volume normalized to 40% porosity.	
ΔV^n	m^3	Change in sediment volume in time step n .	
w_k	-	Weighting factor for grain size fraction k in right-hand-side of the advection equation.	
w_k^{air}	-	Weighting factor for grain size fraction k based on the grain size distribution in the air.	
w_k^{bed}	-	Weighting factor for grain size fraction k based on the grain size distribution in the bed.	
x	m	Cross-shore distance.	
$\Delta x_{i,j}$	m	Size of grid cell i, j in cross-shore direction.	
y	m	Alongshore distance.	
$\Delta y_{i,j}$	m	Size of grid cell i, j in alongshore direction.	
z	m	Height above the bed.	
z'	m	Thickness of inner boundary layer.	
z_b	m+MSL	Bed level.	
Δz_d	m	Depth of disturbance.	



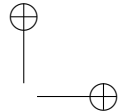
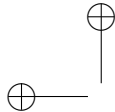
"thesis" — 2016/12/13 — 10:12 — page xii — #16



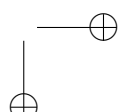
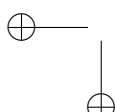
174 LIST OF FIGURES

175	Figure 2.1	Location, orientation, appearance and evolution of the Sand Motor between construction in 2011 and 2015. The box indicates the measurement domain used in the remainder of this paper. A 100 x 100 m grid aligned with the measurement domain is plotted in gray as reference.	12
180	Figure 2.2	Wind and hydrodynamic time series from 2011 to 2015. Hourly averaged wind speeds and directions are obtained from the KNMI meteorological station in Hoek van Holland (upper panels). Offshore still water levels, wave heights and wave periods are obtained from the Europlatform (lower panels). Runup levels are estimated following Stockdon et al. (2006).	13
186	Figure 2.3	Zonation of the Sand Motor domain into zones with net aeolian erosion and no marine influence, net aeolian deposition and no marine influence, mixed aeolian/marine influence and marine influence. Left panels: 2011. Right panels: 2015.	15
190	Figure 2.4	Yearly sedimentation and erosion above 0 m+MSL in the Sand Motor domain. Comparisons are made between the September surveys of each year.	17
193	Figure 2.5	Aeolian sediment budgets in the Sand Motor domain in the period between September 1, 2011 and September 1, 2015.	19
195	Figure 2.6	Cumulative change in sediment volume of all net aeolian erosion and net aeolian deposition zones and the volume deficit. For the linear fit the period prior to February 2012 is discarded (shaded).	20
199	Figure 2.7	Change in size of aeolian zone and mixed zones since construction of the Sand Motor in 2011.	20
201	Figure 2.8	Average height of the aeolian zone in the most recent contour.	21
202	Figure 2.9	Comparison sediment accumulation rates in dunes (>3 m+MSL) for Sand Motor domain and adjacent coasts. Airborne lidar measurements from January 2012 until January 2015 are used. Horizontal dashed lines indicate local averages. The box indicates the Sand Motor domain depicted in previous figures.	22
208	Figure 2.10	Aeolian sediment budget analysis of the Sand Motor	23
209	Figure 3.1	Location, orientation, appearance and evolution of the Sand Motor between construction 2011 and 2015. The box indicates the measurement domain used in the remainder of this paper. A 100 x 100 m grid aligned with the measurement domain is plotted in gray as reference.	29
214	Figure 3.2	Overview of measurement transects N, W, and SW and locations during the MEGAPEX field campaign.	30

216	Figure 3.3	Mast with 6 Wenglor fork laser sensors and a Gill 2D Wind-Sonic ultrasonic wind speed and direction sensor viewed in direction of the wind. The top 3 laser sensors are optional.	31
217			
218			
219	Figure 3.4	a) Wind time series, b) overall particle count rates during the deployments along the westerly transect, and c) offshore tidal elevation. Grey lines indicate the raw data, black lines the hourly averaged data. Colored bars refer to the deployments listed in Table 3.1. Deployments DNo2b and DNo6a are not included as these are located along different transects.	35
220			
221			
222			
223			
224			
225	Figure 3.5	a) Relations between overall particle count and wind speed or b) water level. Closed circles and continuous lines refer to non-storm deployments DNo2 to DNo9. Open circles and dashed lines refer to storm deployments DN10 and DN11. All deployments are listed in Table 3.1.	36
226			
227			
228			
229			
230	Figure 3.6	a) Per-mast particle count, wind speed and direction obtained from stationary mast (Figure 3.2) and b) available fetch and intertidal fetches.	37
231			
232			
233	Figure 3.7	a) Average per-mast particle count rates during the deployments along the westerly transect and b) beach profile at the beginning of the field campaign. Line colors refer to the partitioning of the time series in Figure 3.4.	38
234			
235			
236			
237	Figure 3.8	a) Average per-mast particle count rates during deployment DNo6a along the southwesterly transect and b) beach profile at the beginning of deployment DNo6.	39
238			
239			
240	Figure 3.9	Erosion measured using erosion pins during five tidal cycles during deployment DNo6a along the southwesterly transect.	40
241			
242	Figure 3.10	Cumulative particle count distribution over the vertical during deployment DNo8. The line indicates the percentage of particles that bypasses a certain height above the bed. The horizontal bars visualize the variability in time of the particle count per laser sensor.	41
243			
244			
245			
246			
247	Figure 3.11	Average overall particle count rates depending on governing wind speed and bed level at measurement location, and average still water level depending on governing wind speed.	42
248			
249			
250	Figure 3.12	Visual impression of armor layer at three locations in the Sand Motor region: a) intertidal beach, no armoring b) lower dry beach, minor armoring with shell fragments c) upper dry beach, severe armoring with many shells and coarse sand. Covered surface is approximately 40 x 40 cm in all cases.	42
251			
252			
253			
254			
255	Figure 3.13	Conceptual illustration of how temporal deposits facilitate a continuous sediment supply from the intertidal beach to the dunes.	43
256			
257			
258	Figure 4.1	Contributions of the grain size distribution in the bed and in the air to the weighting factors \hat{w}_k for the equilibrium sediment concentration in Equation 4.9 for different values of the bed interaction parameter.	58
259			
260			
261			



262	Figure 4.2	Schematic of bed composition discretisation and advection scheme. Horizontal exchange of sediment may occur solely through the air that interacts with the <i>bed surface layer</i> . The detail presents the simulation of sorting and beach armoring where the bed surface layer in the upwind grid cell becomes coarser due to non-uniform erosion over the sediment fractions, while the bed surface layer in the downwind grid cell becomes finer due to non-uniform deposition over the sediment fractions. Symbols refer to Equations 4.6 and 4.7.	60
271	Figure 4.3	Sediment transport in time and over the model domain for three scenarios with constant wind. Each line depicts a different location along the beach, starting from $x = 40$ m, which coincides with the high water line in cases P ₃ and P ₄ , and ends at the dune foot. Results are normalized using the transport rate in case P ₁ with almost constant transport (not shown). The difference between the sediment transport at dune foot (green) and the sediment transport at $x = 40$ m is visualized by the red dots and represents the sediment supply from the dry beach. In cases P ₃ and P ₄ the sediment transport at the high water line periodically exceeds the sediment transport at the dune foot, indicating local deposition of sediments originating from the intertidal beach.	63
284	Figure 4.4	Distribution of the shell fraction over the model domain and in time. Sediment supply is inversely related to the degree of beach armoring, indicated by the shell fraction. Median grain size increases with the increase in shell fraction indicating erosion of predominantly fines. High-energy wind events in case P ₄ even mobilize shell fractions resulting in a decrease in beach armoring and an increase in sediment availability.	64
291	Figure 4.5	Average reduction in sediment transport in prototype case P _{3b} compared to case P _{1b} depending on the hourly averaged wind velocity (left panel). The results are obtained using a synthetic variable wind time series following a Weibull distribution with a mean wind velocity of 12 m/s (right panel). The sediment transport reduction (scatter) is binned according to the wind velocity using 0.5 m/s bins. The median reduction per bin (triangles) is used to fit an exponential curve (line). The reduction tends to increase during the simulation (scatter colors).	66
301	Figure 4.6	Comparison between modeled and measured normalized sediment transport rates from wind tunnel experiments described in Nickling and McKenna Neuman (1995). The dashed line depicts the emergence of marbles in terms of increasing roughness density. The visualization of the measurement results is copied from Figure 4 in the original publication without digitization.	68



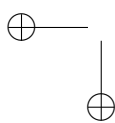
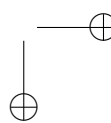
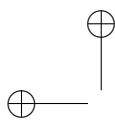
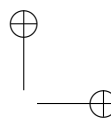
308	Figure 4.7	Comparison between model results and measurements from wind tunnel experiments described in Dong et al. (2004b) (left panel) and RMS errors relative to the mean measured transport rate (right panel). The measured transport rates with a wind velocity of 22 m/s are underestimated due to surpassing of sediment over the sediment trap (Dong et al., 2004b).	69
314	Figure 4.8	Sensitivity of the total normalized sediment transport with respect to case P ₃ for four newly introduced parameters and the wind velocity. The sensitivity of the wind velocity is expressed with respect to the transport rate in case P ₁	70
318	Figure 5.1	Location, orientation, appearance and evolution of the Sand Motor between construction in 2011 and 2015. The box indicates the measurement domain used in the remainder of this paper. A 100 x 100 m grid aligned with the measurement domain is plotted in gray as reference.	77
323	Figure 5.2	Wind and hydrodynamic time series from 2011 to 2015. Hourly averaged wind speeds and directions are obtained from the KNMI meteorological station in Hoek van Holland (upper panels). Offshore still water levels, wave heights and wave periods are obtained from the Europlatform (lower panels). Runup levels are estimated following Stockdon et al. (2006).	79
329	Figure 5.3	Comparison of the cumulative wind transport capacity according to a selection of equilibrium sediment transport formulations and measured total sedimentation in the Sand Motor domain. The equilibrium sediment transport is based on an hourly averaged wind speed and direction time series from September 1, 2011 until September 1, 2015. Offshore wind directions are discarded. For the upper boundary of each estimate all wind directions are weighted equally. For the lower boundary of each estimate the wind directions are weighted according to the magnitude of the onshore component.	80
339	Figure 5.4	Model grid and topography based on the topographic survey of August 3, 2011 (upper panel) and hydrodynamic mask used to limit tidal and wave motions in the dune lake and lagoon (middle and lower panels). Water levels and wave heights are uniformly imposed to the model and multiplied by the multiplication mask and subsequently increased with the addition mask.	81
346	Figure 5.5	Zonation of the Sand Motor domain into zones with net aeolian erosion and no marine influence, net aeolian deposition and no marine influence, mixed aeolian/marine influence and marine influence. Zonation is based on the 0, 3 and 5 m+MSL contour lines that roughly correspond with the mean water level, maximum runup level or berm edge and the dune foot respectively. Left panels: 2011. Right panels: 2015. Source: Hoonhout and de Vries (2016a).	85

354	Figure 5.6	Systematic variation of calibration parameters σ and T_{dry} with $T = 1$ s. The circles indicate the realizations made. The colored background depicts a linear interpolation of the R^2 values with respect to the data presented in Figure 2.6. The solid isolines depict R^2 values from 0.90 to 0.93, while the dashed isolines depict R^2 values from 0.0 to 0.9. The red lines depict the relative supply from the mixed zones ranging from 52% to 57%. The yellow star indicates the optimal value model settings.	86
355			87
356			88
357			88
358			88
359			89
360			
361			
362	Figure 5.7	Measured and modeled yearly sedimentation and erosion above 0 m+MSL. Model results only include aeolian sediment transport as hydrodynamic sediment transport is not computed. Comparisons are made between the September surveys of each year.	
363			
364			
365			
366			
367	Figure 5.8	Measured and simulated net volume change of erosion and deposition volumes as presented in Figure 2.6.	
368			
369	Figure 5.9	Total erosion and deposition volumes at the end of the simulation and measured total erosion and deposition volumes as presented in Figure 2.5.	
370			
371			
372	Figure 5.10	Measured and simulated average beach height in the aeolian zone as presented in Figure 2.8.	
373			
374	Figure 5.11	Simulated shell fraction in the aeolian zone at the end of the simulation.	
375			
376	Figure 5.12	The influence of time-varying and space-varying shear velocity thresholds on the total sedimentation volume. The two leftmost bars depict the measured and modeled sedimentation volume as obtained from the calibrated model (Figure 5.9). The middle two bars depict results from two separate model simulations in which a space-averaged threshold time series or a time-averaged threshold field is imposed respectively. The threshold averages are based on the result from the calibrated model. The two rightmost columns depict a result from a separate model simulation with a constant uniform threshold based on only a constant uniform median grain size and the estimated equilibrium sediment transport following Bagnold (1937b) respectively (Table 5.1).	90
377			
378			
379			
380			
381			
382			
383			
384			
385			
386			
387			
388			
389	Figure 5.13	Relation between shear velocity threshold, shell coverage and σ according to Raupach et al. (1993, Equation 4.13). The shaded areas indicate the relevant parameter ranges from McKenna Neuman et al. (2012) (blue) and the model results (green).	93
390			
391			
392			
393			

"thesis" — 2016/12/13 — 10:12 — page xviii — #22

394 LIST OF TABLES

395	Table 2.1	Zonation of the Sand Motor domain into seven zones with and without marine influence. See also Figure 2.3.	16
396	Table 2.2	Measured porosity values in the Sand Motor domain. Each area is sampled at three different locations. The results per area are presented in ascending order. The last column presents the average porosity for each area that is used to convert the sediment volumes presented in this paper to a hypothetical porosity of 40%.	18
403	Table 3.1	Deployments of measurement masts during the MEGAPEX field campaign. Maximum measured wind speeds are in between brackets.	33
406	Table 5.1	Equilibrium sediment transport formulations, coefficient values* and the ratio between measurements and model results. .	82
407			



"thesis" — 2016/12/13 — 10:12 — page xx — #24

408 ABSTRACT

409 This thesis explores the nature of aeolian sediment availability and its influence on
410 aeolian sediment transport with the aim to improve large scale and long term aeolian
411 sediment transport estimates in (nourished) coastal environments. The generally poor
412 performance of aeolian sediment transport models in coastal environments is often
413 accredited to limitations in sediment availability. Sediment availability can be limited
414 by particular properties of the bed surface. For example, if the beach is moist or
415 covered with non-erodible elements, like shells. If sediment availability is limited, the
416 aeolian sediment transport rate is governed by the sediment availability rather than
417 the wind transport capacity.

418 Aeolian sediment availability is rather intangible as sediment availability is not only
419 affected by aeolian processes, but also by marine and meteorological processes that
420 act on a variety of spatial and temporal scales. The Sand Motor mega nourishment
421 provides a unique opportunity to quantify the spatiotemporal variations in aeolian
422 sediment availability and its effect on aeolian sediment transport. Aeolian sediment
423 accumulation in the Sand Motor region is low compared to the wind transport ca-
424 pacity, while the Sand Motor itself is virtually permanently exposed to wind and
425 accommodates large fetches. Aeolian sediment accumulation is therefore largely de-
426 termined by the sediment availability rather than the wind transport capacity.

427 Multi-annual bi-monthly measurements of the Sand Motor's topography are used
428 for a large scale aeolian sediment budget analysis. The analysis revealed that aeo-
429 lian sediment supply from the dry beach area, that is permanently exposed to wind,
430 diminished a half year after construction of the Sand Motor in 2011 due to the devel-
431 opment of a beach armor layer. From early 2012, two-third of the aeolian sediment
432 deposits originate from the intertidal beach area. The source of aeolian sediment in
433 the Sand Motor region is remarkable as the intertidal beach is periodically flooded
434 and permanently moist.

435 The importance of the intertidal beach area in the Sand Motor region is tested dur-
436 ing a six-week field campaign. Gradients in aeolian sediment transport are measured
437 during the field campaign as to localize aeolian sediment source and sink areas. A
438 consistent supply from the intertidal beach area was measured that was temporarily
439 deposited at the dry beach. The temporary deposits were transported further during
440 high water, when sediment supply from the intertidal beach ceased, resulting in a
441 continuous sediment supply to the dunes. The temporary deposition of sediment at
442 the dry beach was likely promoted by the presence of a berm that affects the local
443 wind shear. Moreover, the berm edge coincided with the onset of the beach armor
444 layer that might have further promoted deposition of sediment.

445 The measurements on spatiotemporal variations in aeolian sediment availability
446 and supply inspired an attempt to capture the characteristics of aeolian sediment avail-
447 ability in coastal environments in a comprehensive model approach. The resulting
448 model simulates spatiotemporal variations in bed surface properties and their com-
449 bined influence on aeolian sediment availability and transport. The implementation
450 of multi-fraction aeolian sediment transport in the model introduces the recurrence

451 relation between aeolian sediment availability and transport through self-grading of
452 sediment.

453 The model was applied in a four-year hindcast of the Sand Motor mega nourish-
454 ment as first attempt to field validation. The model reproduces the multi-annual
455 aeolian sediment erosion and deposition volumes, and the relative importance of the
456 intertidal beach area as source of aeolian sediment well. Seasonal variations in aeo-
457 lian sediment transport are incidentally missed by the model. The model accuracy
458 is reflected in a R^2 value of 0.93 when comparing time series of measured and mod-
459 eled total aeolian sediment transport volumes in the four years since construction of
460 the Sand Motor. The results suggest that indeed significant limitations in sediment
461 availability, due to soil moisture content and beach armoring, govern aeolian sedi-
462 ment transport in the Sand Motor region. A comparison with a simulation without
463 limitation in sediment availability suggests that aeolian sediment availability in the
464 Sand Motor region is limited to about 25% of the wind transport capacity. Moreover,
465 both spatial and temporal variations in aeolian sediment availability as well as the
466 recurrence relation between aeolian sediment availability and transport are essential
467 to accurate long term and large scale aeolian sediment transport estimates.

468 SAMENVATTING

469 Dit proefschrift onderzoekt de invloed van beschikbaarheid van eolisch sediment op
470 eolisch sediment transport met als doel het verbeteren van grootschalige en lange ter-
471 mijn voorspellingen van eolisch sediment transport in (gesuppleerde) kustgebieden.
472 Bestaande modellen voor eolisch sediment transport presteren in het algemeen slecht
473 in kustgebieden. De slechte prestaties worden dikwijls geweten aan een beperkte be-
474 schikbaarheid van eolisch sediment. De beschikbaarheid van eolisch sediment kan
475 worden beperkt door specifieke eigenschappen van het strandoppervlak. Als bijvoor-
476beeld het strand vochtig is of bedekt met niet-erodeerbare elementen, zoals schelpen,
477 kan de beschikbaarheid van sediment worden beperkt. In dat geval wordt de eoli-
478 sche sediment flux bepaald door de beschikbaarheid van sediment in plaats van de
479 transportcapaciteit van de wind.

480 De beschikbaarheid van eolisch sediment is een redelijk ongrijpbaar fenomeen, om-
481 dat deze niet alleen wordt beïnvloed door eolische processen, maar ook door marine
482 en meteorologische processen die op verschillende ruimtelijke en temporele schalen
483 actief zijn. De Zandmotor megasuppletie biedt een unieke gelegenheid om de tem-
484 porele en ruimtelijke variaties in de beschikbaarheid van eolisch sediment en het ef-
485 effect daarvan op eolisch sediment transport te kwantificeren. Instuifvolumes rond de
486 Zandmotor zijn klein in vergelijking met de transportcapaciteit van de wind, terwijl
487 de Zandmotor met haar grote strijklengetjes zelf vrijwel permanent blootgesteld is aan
488 wind. De instuiving van sediment wordt daar dus grotendeels bepaald door de be-
489 schikbaarheid van sediment in plaats van de transportcapaciteit van de wind.

490 Meerjarige tweemaandelijks metingen van de topografie van de Zandmotor zijn
491 gebruikt voor een grootschalige eolische sediment budget analyse. Uit de analyse
492 bleek dat de aanvoer van eolisch sediment vanaf het droge strand, dat permanent
493 blootgesteld is aan de wind, vanaf een half jaar na de aanleg van de Zandmotor in
494 2011 sterk is verminderd als gevolg van het ontstaan van een schelpenlaag. Vanaf het
495 begin van 2012 is tweederde van het instuivvolume afkomstig uit het intergetijdenge-
496 bied. Deze bron van eolische sediment rond de Zandmotor is opmerkelijk omdat het
497 intergetijdenstrand periodiek overstroomd en permanent vochtig is.

498 Het belang van het intergetijdengebied strand rond de Zandmotor wordt beves-
499 tigd tijdens een zes weken durende veld campagne. Tijdens deze campagne zijn
500 gradi enten in eolisch sediment transport gemeten de bron van eolisch sediment te
501 bepalen. De gemeten constante aanvoer vanuit het intergetijdengebied bleek tijde-
502 lijk te sedimenteren op het droge strand. Deze tijdelijke afzettingen werden tijdens
503 hoogwater verder getransporteerd wanneer de sediment aanvoer vanaf het intergetij-
504 denstrand stagneerde. Hierdoor ontstond een continue toevoer van sediment naar de
505 duinen. De tijdelijke afzetting van sediment op het droge strand werd vermoedelijk
506 bevorderd door de aanwezigheid van een berm die de lokale schuifspanning van de
507 wind beïnvloedt. Bovendien viel de rand van de berm samen met het begin van de
508 schelpenlaag die het neerslaan van sediment mogelijk verder bevorderd heeft.

509 De gemeten ruimtelijke en temporele variaties in de beschikbaarheid van eolisch
510 sediment hebben een poging geïnspireerd om de kenmerken van beschikbaarheid

511 van eolisch sediment aan de kust te vatten in een alomvattende model aanpak. Het
512 resulterende model simuleert variaties in tijd en ruimte van eigenschappen van het
513 strandoppervlak en hun gezamenlijke invloed op de beschikbaarheid en transport van
514 eolisch sediment. De implementatie van eolisch sediment transport over meerdere
515 korrelgrootte fracties in het model introduceert de recurrente betrekking tussen de
516 beschikbaarheid en het transport van eolisch sediment door middel van zelfgradering
517 van sediment.

518 Het model is toegepast in een vierjarige hindcast van de Zandmotor megasuppletie
519 als eerste poging tot veldvalidatie. Het model reproduceert de meerjarige erosie
520 en depositie volumes van eolisch sediment, en het relatieve belang van het interge-
521 tijdengebied als bron van eolisch sediment, goed. Seizoensafhankelijke variaties in
522 eolisch sediment transport worden soms gemist door het model. De nauwkeurigheid
523 van het model is weerspiegeld in een R^2 waarde van 0,93 wanneer gemeten en gemo-
524 delleerde tijdseries voor het totaal door de wind getransporteerde sedimentvolume
525 in de vier jaar na constructie van de Zandmotor worden vergeleken. De resultaten
526 suggereren dat significante beperkingen in sediment beschikbaarheid, als gevolg van
527 het vochtgehalte van het strand en het vormen van een schelpenlaag, inderdaad be-
528 palend zijn voor het eolisch sediment transport rond de Zandmotor. Een vergelijking
529 met een simulatie zonder beperking in beschikbaarheid van sediment suggereert dat
530 de beschikbaarheid van eolisch sediment rond de Zandmotor is beperkt tot ongeveer
531 25% van de transportcapaciteit van de wind. Bovendien zijn zowel de ruimtelijke en
532 temporele variaties in de beschikbaarheid van eolisch sediment, evenals de recurrente
533 betrekking tussen de beschikbaarheid en transport van eolisch sediment essentieel
534 voor een nauwkeurige lange termijn en grootschalige voorspellingen van eolisch sedi-
535 ment transport.

1

536

537

538 INTRODUCTION

539 1.1 MOTIVATION

540 Aeolian sediment transport is a prerequisite to growth and resilience of coastal dunes.
541 Coastal dunes function as a natural protection against flooding from the sea. As hu-
542 man societies are particularly attracted to low-lying areas near the sea, the reliability
543 and resilience of the protective coastal dune systems becomes vital for economic ac-
544 tivities and human well-being. This societal demand for a safe and comfortable living
545 space, that initiated the discipline of coastal engineering, developed our understand-
546 ing of coastal safety tremendously in the past decades. The increased understanding
547 of our coastal systems resulted in structural mitigation of coastal risks using rigid
548 solutions or local nourishments (Hamm et al., 2002) and the engineering of entire
549 coastlines worldwide (Donchyts et al., 2016).

550 With the increased confidence in our ability to mitigate coastal risks, additional de-
551 mands and functions for coastal flood protections arose. Soft engineering solutions
552 with limited environmental and ecological impact gained preference over rigid so-
553 lutions. Recently, the exponent of soft engineering emerged as nature-based coastal
554 flood protections (Waterman, 2010; de Vriend et al., 2015). Nature-based flood pro-
555 tections pursue the idea of stimulating natural processes with the aim of increasing
556 coastal safety and is based on the assumption that the incidental or concentrated
557 interventions necessary for the stimulation of nature are less intrusive than classic
558 solutions to coastal safety. Moreover, nature-based solutions tend to accommodate
559 long-term monitoring and periodic adaptation and intervention that increases flex-
560 ibility with respect to planning and execution as well as the occurrence of coastal
561 hazards. The increased flexibility can make nature-based flood protection also cost-
562 effective (Van Sloot et al., 2013).

563 An innovative example of a nature-based solution to coastal safety is the Sand Mo-
564 tor (or Sand Engine, Stive et al., 2013). The Sand Motor is an artificial sandy peninsula
565 that was constructed along the Dutch coast in 2011. The Sand Motor provides a 21
566 Mm³ sediment source to the Dutch coast that is to be dispersed by natural processes,
567 like tides and waves, over a period of about two decades. Although the construction
568 of the Sand Motor clearly disturbs the coastal system, the disturbance is incidental
569 and concentrated. In addition, the presence of the Sand Motor theoretically decreases
570 the necessity of measures to mitigate coastal risks at other locations along the Dutch
571 coast.

572 The Sand Motor is the provisional pinnacle of the evolution of soft engineering so-
573 lutions to coastal safety in The Netherlands. Soft engineering solutions started with

574 the dynamic preservation act of 1990 that prescribes extensive nourishment program
575 initiated to protect The Netherlands from flooding from the sea (Min. V&W, 1990).
576 Since the start of the program the distance between nourishments and dunes increased
577 steadily. The initial dune and beach nourishments were replaced by foreshore nour-
578 ishments as these are more cost-effective and less intrusive to the environmental and
579 recreational functions of the coastal dune system. Nature-based solutions, like the
580 Sand Motor, typically place nourishments kilometers away from the dune system that
581 needs to be enforced.

582 With the increasing distance between nourishments and dunes, the effectiveness of
583 nourishments in mitigating coastal risks becomes more difficult to assess. Ultimately
584 the reliability of coastal dune systems is related to the sediment volume that is con-
585 tained by the system. However, also the location in the coastal profile where the
586 sediment resides is important. Sediment in the dunes provides a direct buffer against
587 flooding in case of storm erosion, while sediment on the beach and foreshore influ-
588 ences coastal safety indirectly by depth-induced breaking of waves and consequently
589 a reduction of the critical dune volume required to withstand a normative storm (Wal-
590 stra, 2016). The sediment volume that resides in the dunes provides arguably a more
591 persistent protection against flooding as the volume is typically only affected by se-
592 vere storms. In contrast, the sediment volume that resides on the foreshore and beach
593 is affected by seasonal nearshore bar cycles and mild storms, which increase the un-
594 certainty of its contribution to coastal safety. It is therefore relevant to understand
595 how sediment arrives in the dunes and provide a persistent contribution to coastal
596 safety.

597 A key issue is to understand sediment transport pathways from nourishment to
598 dunes. Many studies and sophisticated numerical models are available that describe
599 hydrodynamic sediment transport. However, only a small fraction of the sediment
600 moved in the nearshore ultimately arrives in the dunes (Aagaard et al., 2004). It is this
601 small wind-induced sediment flux that provides us with the natural and persistent
602 coastal flood protection that nature-based solutions aim for. In addition, this small
603 wind-induced sediment flux gives coastal dune systems the natural resilience to storm
604 impacts and the conditions for survival of persistent dune vegetation that strengthens
605 the coastal dune systems, like marram grass (Borsje et al., 2011). It is also this small
606 wind-induced sediment flux that is least understood and consistently overestimated
607 by existing sediment transport models.

608 Aeolian sediment transport models describe the wind-induced sediment transport
609 rate. In coastal environments these models tend to overestimate the aeolian sediment
610 accumulation volumes, which is often accredited to limitations in sediment availabil-
611 ity (Houser, 2009; Delgado-Fernandez et al., 2012; de Vries et al., 2014a). Sediment
612 availability can be limited by particular properties of the bed surface. For example,
613 if the beach is moist or covered with non-erodible elements, like shells (Wiggs et al.,
614 2004; Edwards and Namikas, 2009; Namikas et al., 2010; McKenna Neuman et al.,
615 2012). If sediment availability is limited, the aeolian sediment transport rate is gov-
616 erned by the sediment availability rather than the wind transport capacity, which
617 violates the common assumption in aeolian sediment transport models.

618 This thesis explores the nature of aeolian sediment availability and its influence on
619 aeolian sediment transport with the aim to improve large scale and long term aeolian
620 sediment transport estimates in nourished coastal environments. This work is per-

621 formed within the framework of *ERC-Advanced Grant 291206 – Nearshore Monitoring*
622 *and Modeling (NEMO)* that aims at an integrated modeling strategy for large scale
623 and long term coastal sediment transport that extends from foreshore to backshore.
624 Improving aeolian sediment transport estimates helps the completion of the sediment
625 transport pathways from foreshore to backshore and from nourishment to dunes and
626 thereby the assessment of measures that attempt to mitigate coastal risks, including
627 nature-based coastal flood protections, on their effectiveness.

628 1.2 RESEARCH OBJECTIVES

629 This thesis pursues four main research objectives. Each chapter is dedicated to one re-
630 search objective. The research objectives are elaborated in research questions that are
631 addressed in the concluding chapter of this thesis (Chapter 7). The research objectives
632 and questions are formulated as:

633 RESEARCH OBJECTIVE #1 Identify the main sources for aeolian sediment in coastal
634 environments and particularly at the Sand Motor mega nourishment (Chapter
635 2).

636 The research questions related to objective #1 are:

- 637 1.1 What is the total aeolian sediment supply at the Sand Motor mega nour-
638 ishment?
- 639 1.2 What are the main deposition areas of aeolian sediment at the Sand Motor
640 mega nourishment?
- 641 1.3 What are the main source areas of aeolian sediment at the Sand Motor
642 mega nourishment?
- 643 1.4 What bed surface characteristics can explain any spatial variations in aeo-
644 lian sediment supply at the Sand Motor mega nourishment?
- 645 1.5 What is the relevance of these bed surface characteristics for coastal sys-
646 tems in general?
- 647 1.6 What characteristics of a coastal system determine aeolian sediment supply
648 and dune growth?

649 RESEARCH OBJECTIVE #2 Identify the main processes that govern aeolian sediment
650 availability and supply in coastal environments and particularly at the Sand
651 Motor mega nourishment (Chapter 3).

652 The research questions related to objective #2 are:

- 653 2.1 What bed surface characteristics are related to aeolian sediment supply?
- 654 2.2 What processes govern the supply of aeolian sediment from the source
655 areas?
- 656 2.3 What processes govern the deposition of aeolian sediment in the deposition
657 areas?

658 RESEARCH OBJECTIVE #3 Develop a numerical model approach to describe the in-
659 fluence of spatiotemporal variations in aeolian sediment availability on aeolian
660 sediment transport and harmonize existing model approaches to aeolian sedi-
661 ment availability where possible (Chapter 4).

662 The research questions related to objective #3 are:

- 663 3.1 What are existing model approaches to describe the influence of aeolian
664 sediment availability on aeolian sediment transport, what are the similar-
665 ities and differences among them and which approaches are mutually ex-
666 clusive?
- 667 3.2 What processes that were identified to be relevant to aeolian sediment
668 availability are not covered with sufficient accuracy by existing model ap-
669 proaches?
- 670 3.3 What are the requirements for a model approach that harmonizes existing,
671 mutual inclusive model approaches and is conceptually able to describe all
672 processes relevant to aeolian sediment availability and transport?

673 RESEARCH OBJECTIVE #4 Validate the numerical model approach to reproduce the
674 location and size of sources for aeolian sediment in coastal environments and
675 particularly at the Sand Motor mega nourishment (Chapter 5).

676 The research questions related to objective #4 are:

- 677 4.1 Can the calibrated numerical model reproduce the total aeolian sediment
678 supply at the Sand Motor mega nourishment with any statistical signifi-
679 cance?
- 680 4.2 Can the calibrated numerical model reproduce the main source and depo-
681 sition areas at the Sand Motor mega nourishment?
- 682 4.3 What implemented processes are in retrospect significant to the model re-
683 sult?

684 1.3 THESIS OUTLINE

685 This thesis constitutes four parts:

686 Part I presents field data dedicated to the aeolian sediment supply and transport
687 at the Sand Motor mega nourishment.

688 Chapter 2 presents a large scale aeolian sediment budget analysis that iden-
689 tifies the main suppliers of aeolian sediment in the Sand Motor region.

690 The large scale sediment budget analysis inspired the six-week field cam-
691 paign presented in Chapter 3. Gradients in aeolian sediment transport were
692 measured during the field campaign. Gradients in aeolian sediment trans-
693 port reveal areas with net erosion and thereby the sources of aeolian sedi-
694 ment. The measurements therefore enable a detailed analysis of processes

695 governing the spatiotemporal variations in aeolian sediment availability as
696 identified in the aeolian sediment budget analysis.

697 Part II presents a numerical model for aeolian sediment availability and transport
698 that is inspired by the field observations.

699 The field data show that significant spatial variations in aeolian sediment
700 availability can exist and can affect net aeolian sediment transport rates. The
701 variations in aeolian sediment availability coincide with changes in bed sur-
702 face properties, like soil moisture content and beach armoring. In coastal
703 environments these bed surface properties typically also vary in time. As-
704 suming that the spatiotemporal variations in bed surface properties indeed
705 influence the aeolian sediment availability and transport, a numerical aeolian
706 sediment transport model is developed.

707 Chapter 4 presents the model philosophy and design. The model focuses on
708 the incorporation of spatiotemporal variability in aeolian sediment availabil-
709 ity, which is illustrated using the process of beach armoring. Beach armoring
710 occurs when roughness elements emerge from the bed and is a typical pro-
711 cess that causes spatiotemporal variations in aeolian sediment availability.
712 Both conceptual cases and wind tunnel experiments are used to illustrate
713 the basic model behavior.

714 Chapter 5 describes the calibration and application of the model to the field
715 data presented in Chapter 2 as a first attempt to field validation of the nu-
716 mercial model.

717 Part III concludes this thesis by addressing the research objectives and questions,
718 and a discussion on the nature of aeolian sediment availability and corre-
719 sponding modeling strategies.

720 Part IV contains appendices with specifics on the reference model, the numerical
721 model implementation and available model settings presented in Chapter 4.

722

Part I

723

FIELD DATA

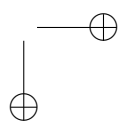
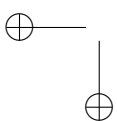
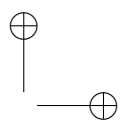
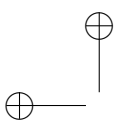
724

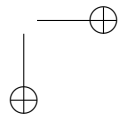
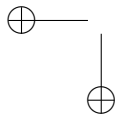
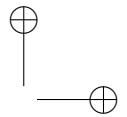
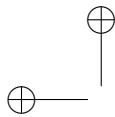
Field data is collected at the Sand Motor mega nourishment in The Netherlands. The Sand Motor showed a peculiar morphological development since its construction as it is permanently exposed to wind and yet its sub-aerial morphology is remarkably static.

725

726

727





2

728

729

730 LARGE SCALE SEDIMENT BUDGETS

731 *This chapter is based on a previous publication: Hoonhout, B. M. and de Vries, S. (2016a).*
732 *Aeolian sediment supply at a mega nourishment. Coastal Engineering. Submitted.*

733 **2.1 INTRODUCTION**

734 Aeolian sediment supply is a prerequisite to growth and resilience of coastal dunes
735 that function as a natural protection against flooding from the sea. Expanding hu-
736 man activities in coastal areas and growing uncertainties related to climate change,
737 increase coastal risks. Mitigation of these risks resulted in the engineering of entire
738 coastlines (Donchyts et al., 2016). Rigid solutions and local nourishments are tradi-
739 tional solutions to a societal demand for coastal safety (Hamm et al., 2002). With the
740 increased confidence in our ability to mitigate coastal risks, additional demands and
741 functions for coastal flood protections arose. Soft engineering solutions with limited
742 environmental and ecological impact (Waterman, 2010; de Vriend et al., 2015) gained
743 preference over rigid solutions or local nourishments. Recently, the exponent of soft
744 engineering emerged as mega nourishments (Stive et al., 2013). Mega nourishments
745 pursue the idea of stimulating natural sediment transport processes with the aim of
746 increasing coastal safety. The idea is based on the assumption that the incidental or
747 concentrated interventions necessary for the stimulation of nature are less intrusive
748 than classic solutions to coastal safety. Moreover, mega nourishments tend to accom-
749 modate long-term monitoring and periodic adaptation and intervention that increases
750 flexibility with respect to planning and execution as well as the occurrence of coastal
751 hazards. The increased flexibility can make mega nourishments also cost-effective
752 (Van Slobee et al., 2013).

753 The effectiveness of a mega nourishment depends on the sediment transport path-
754 ways from nourishment to dunes. A small fraction of the sediment moved in the
755 nearshore ultimately arrives in the dunes (Aagaard et al., 2004). It is this small aeo-
756 lian sediment supply that provides us with the natural and persistent coastal safety
757 that mega nourishments aim for. In addition, this small aeolian sediment supply
758 gives coastal dune systems the natural resilience to storm impacts and the conditions
759 for survival of persistent dune vegetation that strengthens the dunes, like marram
760 grass (Borsje et al., 2011). It is also this small aeolian sediment supply that is least
761 understood.

762 Mega nourishments affect aeolian sediment supply to coastal dunes in various ways.
763 First, sand used for nourishment is typically obtained from offshore borrowing pits
764 and differs from the original beach sand in terms of size and composition, affect-

ing the erodibility of the beach (van der Wal, 1998, 2000). Second, aeolian sediment availability (following the definition of Kocurek and Lancaster, 1999) at beach nourishments that are constructed above storm surge level can be significantly reduced by deflation lag deposits (Jackson et al., 2010). The absence of regular flooding and wave-reworking allows lag deposits to develop a beach armor layer, resulting in compartmentalization of the nourishment in armored and unarmored surfaces. McKenna Neuman et al. (2012) illustrated how deflation lag deposits increase the shear velocity threshold significantly and reduce aeolian sediment availability and subsequently supply from the higher supratidal beach. Deflation lag deposits can therefore cause intertidal and low-lying supratidal beaches to gain importance over the high and dry beach as source of aeolian sediment. Third, the placement of a nourishment is known to affect nearshore processes (Grunnet and Ruessink, 2005; Ojeda et al., 2008; De Schipper et al., 2013). Synchronization between aeolian and nearshore processes, like onshore bar migration and welding, is reported to stimulate aeolian sediment supply to coastal dunes (Houser, 2009; Anthony, 2013). The importance of low-lying beaches as source of aeolian sediment might therefore also be affected by changing bar dynamics.

Jackson and Nordstrom (2011) emphasized the necessity for the quantification of the effect of large scale beach nourishment designs on aeolian sediment supply. Quantitative predictions of aeolian sediment availability and supply in coastal environments has proven to be challenging (Sherman et al., 1998; Sherman and Li, 2012). Limitations in aeolian sediment availability are often identified as reason for the discrepancy between measured and predicted sediment transport rates (Delgado-Fernandez et al., 2012; de Vries et al., 2014a; Lynch et al., 2016).

Mega nourishments inherently cause spatiotemporal variations in aeolian sediment availability. The spatial variations are caused by compartmentalization of the beach. The temporal variations are induced by adaptation of the large coastal disturbance to the wave and wind climate, resulting in changing in beach width, slope and composition (de Schipper et al., 2016). Consequently, quantification of aeolian sediment availability and supply from mega nourishments requires differentiation in space and time.

This paper presents an aeolian sediment budget analysis of the 21 Mm³ Sand Motor mega nourishment based on four years of bi-monthly topographic surveys. The sediment budget analysis quantifies the net aeolian sediment supply to the dunes, dune lake and lagoon accommodated by the Sand Motor. The Sand Motor constitutes distinct areas that are either influenced by marine processes, by aeolian processes or by a combination of both. Therefore, the influence of marine and aeolian processes on aeolian sediment supply can be separated and spatiotemporal variations in aeolian sediment availability can be identified with reasonable accuracy. The observed compartmentalization of the Sand Motor is discussed in relation to limitations in aeolian sediment availability, as well as the design of mega nourishments like the Sand Motor as solution to coastal safety.

2.2 FIELD SITE

The Sand Motor (or Sand Engine) is an artificial 21 Mm³ sandy peninsula protruding into the North Sea off the Delfland coast in The Netherlands (Figure 2.1, Stive et al.,

810 2013). The Sand Motor is an example of a mega nourishment and is intended to nourish
811 the Holland coast for a period of two decades, while stimulating both biodiversity
812 and recreation.

813 The Sand Motor was constructed in 2011 and its bulged shoreline initially extended
814 about 1 km seaward and stretched over approximately 2 km along the original coast-
815 line. The original coast was characterized by an alongshore uniform profile with a
816 vegetated dune with an average height of 13 m and a linear beach with a 1:40 slope.
817 The dune foot is located at a height of approximately 5 m+MSL.

818 Due to natural sediment dynamics the Sand Motor distributes about 1 Mm³ of
819 sand per year to the adjacent coasts (Figure 2.1). The majority of this sand volume
820 is transported by tides and waves. However, the Sand Motor is constructed up to 5
821 m+MSL and locally up to 7 m+MSL, which is in either case well above the maximum
822 surge level of 3 m+MSL (Figure 2.2c). Therefore, the majority of the Sand Motor area
823 is uniquely shaped by wind.

824 The Sand Motor comprises both a dune lake and a lagoon that act as large traps
825 for aeolian sediment (Figure 2.1). The lagoon is affected by tidal forcing, although
826 the tidal amplitude quickly diminished over time as the entry channel elongated. The
827 tidal range of about 2 m that is present at the Sand Motor periphery (Figure 2.2c), is
828 nowadays damped to less than 20 cm inside the lagoon (de Vries et al., 2015). Con-
829 sequently, the tidal currents at the closed end of the lagoon, where most aeolian
830 sediment is trapped, are negligible.

831 Sand used for construction of the Sand Motor is obtained from an offshore borrow-
832 ing pit in the North Sea. The sand is predominantly Holocene sand with a significant
833 amount of fines. The median grain size is slightly coarser than found originally along
834 the Delfland coast. Apart from sand fractions, the sediment contains a large amount
835 of shells, shell fractions, some pebbles and cobbles and an occasional fraction of a
836 mammoth bone.

837 The dominant wind direction at the Sand Motor is south to southwest (Figure 2.2a).
838 However, during storm conditions the wind direction tends to be southwest to north-
839 west. During extreme storm conditions the wind direction tends to be northwest.
840 Northwest storms are typically accompanied by significant surges as the fetch is
841 virtually unbounded to the northwest, while surges from the southwest are limited
842 due to the presence of the narrowing of the North Sea at the Strait of Dover (Figure
843 2.1, inset).

844 2.3 METHODOLOGY

845 Spatiotemporal variations in aeolian sediment supply in the Sand Motor domain are
846 identified using an aeolian sediment budget analysis. A sediment budget analysis can
847 be performed if frequent topographic measurements are available (Davidson-Arnott
848 and Law, 1990) and sediment exchange over the border of the measurement domain
849 is limited. In a sediment budget analysis the morphological change in predetermined
850 areas are converted to volumetric changes (budgets) that are compared in a sediment
851 volume balance.

852 A sediment budget analysis is particularly suitable for coastal sites with a complex
853 and dynamic topography, like the Sand Motor. The use of (dense) topographic mea-
854 surements ensures that any local variations in the topography are included. Moreover,

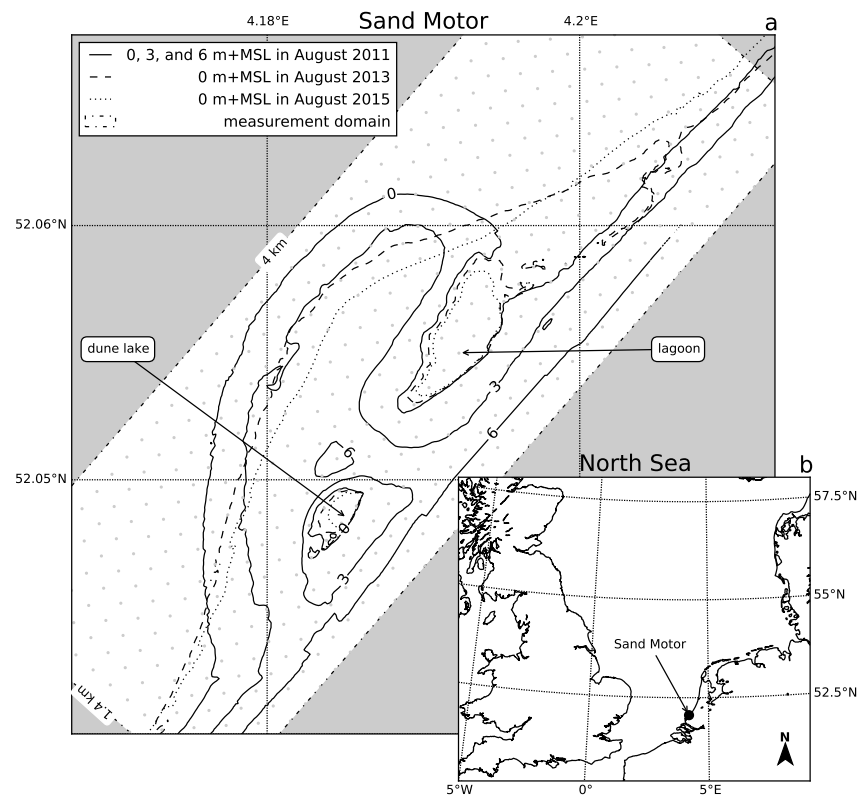


Figure 2.1: Location, orientation, appearance and evolution of the Sand Motor between construction in 2011 and 2015. The box indicates the measurement domain used in the remainder of this paper. A 100 x 100 m grid aligned with the measurement domain is plotted in gray as reference.

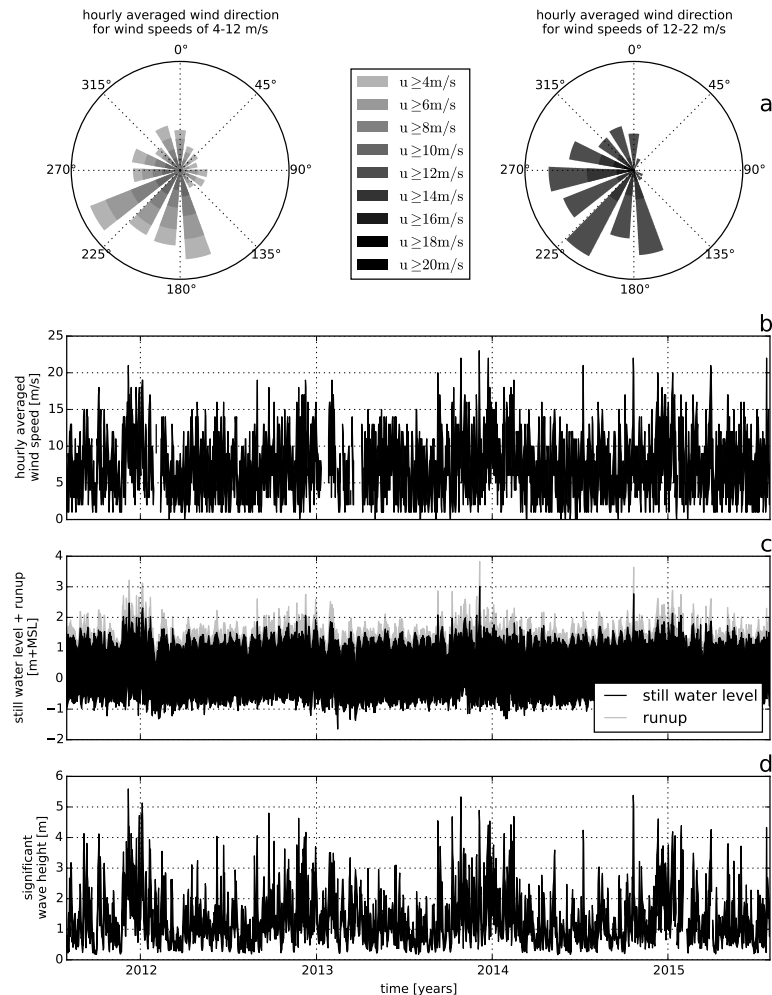


Figure 2.2: Wind and hydrodynamic time series from 2011 to 2015. Hourly averaged wind speeds and directions are obtained from the KNMI meteorological station in Hoek van Holland (upper panels). Offshore still water levels, wave heights and wave periods are obtained from the Europlatform (lower panels). Runup levels are estimated following Stockdon et al. (2006).

no assumptions on the local representativeness of the measurements are needed and the methodology is applicable to a wide range of spatial or temporal scales.

In the Sand Motor domain it is possible to separate the marine and aeolian influence on erosion and deposition of sediment directly from a sediment budget analysis. The high construction height of the Sand Motor and the absence of regular storm surges in the first four years after construction make that distinct areas exist that are either influenced by marine or aeolian processes. The sediment budgets are determined along the borders of these marine and aeolian zones.

2.3.1 Topographic measurements

32 topographic measurements of the Sand Motor domain obtained over a period of four years are used to determine the overall sediment budget of the Sand Motor domain (de Schipper et al., 2016). The measurement area covers 1.4 km cross-shore and 4 km alongshore (Figure 2.1). The nearshore bathymetry is surveyed using a jetski equipped with an echo sounder and RTK-GPS receiver. The topography of the Sand Motor from the waterline up to the dune foot is surveyed using an all-terrain vehicle (ATV) that is also equipped with a RTK-GPS receiver. Inundated areas that are too shallow for the jetski, like the tidal channel and the dune lake, are surveyed using a manually pushed RTK-GPS wheel. The survey is performed along cross-shore transects that are 20 m apart. The resulting trajectories are interpolated to a regular 10 m x 10 m grid for the sediment budget analysis. Surveys that show a morphological rate of change that is more than two standard deviations from the average are considered outliers. The measurements of September 4, 2011 and June 21, 2012 are discarded as outliers.

The topography in the dune area, which is not included in the RTK-GPS surveys, is monitored by airborne lidar. Half-yearly measurements from the southern Holland coast (Delfland coast) are available since 2011, prior to the construction of the Sand Motor. The lidar measurements have a spatial resolution of 2 m or 5 m. The measurements are corrected for the presence of vegetation and artificial objects, like beach pavilions, and interpolated to the same 10 m x 10 m grid and the same moments in time as the RTK-GPS measurements.

2.3.2 Zonation

The Sand Motor domain is divided into seven zones for the aeolian sediment budget analysis (Table 2.1 and Figure 2.3). The zonation aims to separate areas with marine influences from areas without marine influences, and separate areas with net aeolian erosion from areas with net aeolian deposition.

The zonation is based on the 0 m+MSL, 3 m+MSL and 5 m+MSL contour lines that roughly correspond to mean sea level, the edge of the berm or maximum runup level (Figure 2.2c) and the dune foot respectively. The contours are determined such that the spatial variance in the bed level change of the zones is minimized. The minimization ensures that the optimal division between erosion and deposition areas is found. Moreover, the 3 m+MSL and 5 m+MSL contour lines have been relatively static since construction of the Sand Motor.

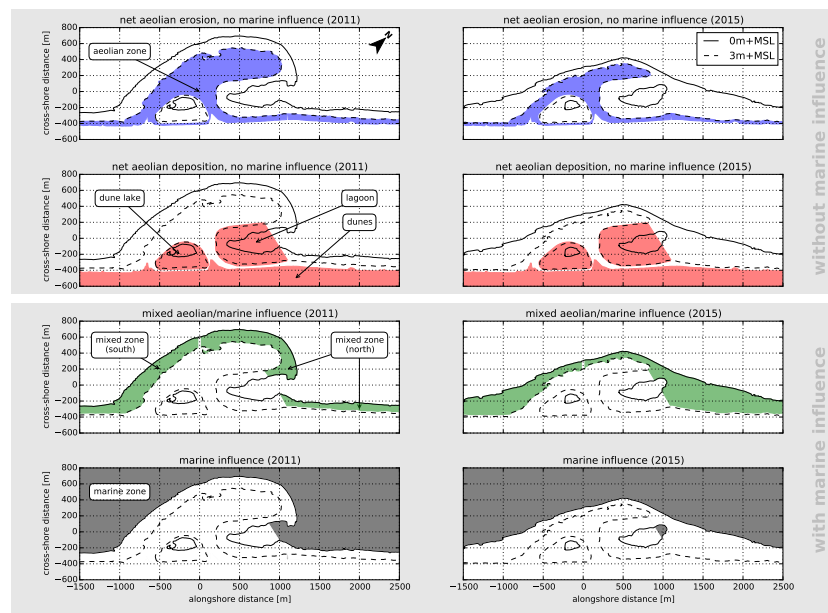


Figure 2.3: Zonation of the Sand Motor domain into zones with net aeolian erosion and no marine influence, net aeolian deposition and no marine influence, mixed aeolian/marine influence and marine influence. Left panels: 2011. Right panels: 2015.

Table 2.1: Zonation of the Sand Motor domain into seven zones with and without marine influence. See also Figure 2.3.

<i>without</i> marine influence	<i>with</i> marine influence
aeolian zone	mixed zone (north)
dunes	mixed zone (south)
dune lake	marine zone
lagoon	

897 To ensure a constant shape and size of the zones during the analysis, the convex
 898 hull of all 3 m+MSL contour lines is used as zone boundary for the lake and lagoon.
 899 Also for the dunes minimal variations over time in zone shape and size are removed
 900 by using the most seaward position of all contour lines. Consequently, only the ae-
 901 olian zone and mixed zones change in shape and size over time. The volumetric
 902 change between two consecutive measurements is determined for these zones within
 903 the smaller contour:

$$\Delta V^n = \hat{A}_c \cdot (\bar{z}_b^n - \bar{z}_b^{n-1}) \quad \text{where } \hat{A}_c = \min(A_c^n; A_c^{n-1}) \quad (2.1)$$

904 with ΔV^n the volume change, A_c^n the surface area of the zone and \bar{z}_b^n the average
 905 bed level in the zone, all in time interval n . The (cumulative) sum over all time
 906 intervals of the volume changes in each zone is used in the analysis. By using the
 907 smaller of two contours in a comparison, a part of the larger contour is neglected:

$$A_{c,\text{neglected}}^n = \max(A_c^n; A_c^{n-1}) - \hat{A}_c \quad (2.2)$$

908 The neglected area of the zone with the largest change in size, the aeolian zone, is on
 909 average 2% and never larger than 8%.

910 2.3.3 Spatial variations in porosity

911 The change in sediment volume is susceptible to changes in porosity. In order to
 912 relate the changes in sediment volume to the transport of sediment mass, variations
 913 in porosity need to be accounted for. Porosity values in the Sand Motor domain are
 914 obtained from core samples and used to account for the spatial variations in porosity.
 915 The core samples have a diameter of 8 cm and depth of 10 cm from the bed surface
 916 in an attempt to capture the porosity in the aeolian active layer of the bed. Each
 917 sample is dried and submerged in water to determine the porosity. For comparison,
 918 all presented sediment volumes in this paper are converted to a hypothetical porosity
 919 of 40% according to:

$$V_{40\%} = V \cdot \frac{1-p}{1-40\%} \quad (2.3)$$

920 where V [m^3] is the measured sediment volume and p [-] the porosity.

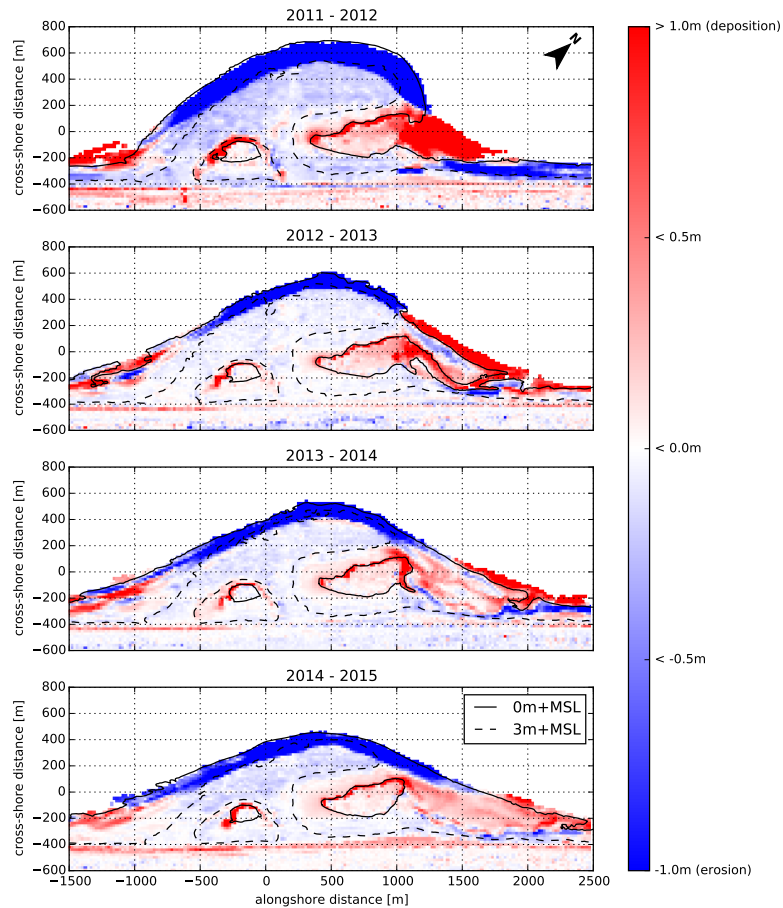


Figure 2.4: Yearly sedimentation and erosion above 0 m+MSL in the Sand Motor domain. Comparisons are made between the September surveys of each year.

Table 2.2: Measured porosity values in the Sand Motor domain. Each area is sampled at three different locations. The results per area are presented in ascending order. The last column presents the average porosity for each area that is used to convert the sediment volumes presented in this paper to a hypothetical porosity of 40%.

Area	Porosity		
	min.	max.	avg.
Aeolian zone	39.0%	39.4%	40.2%
Mixed zone (north)	38.4%	39.8%	40.8%
Mixed zone (south)	37.1%	38.4%	38.4%
Dunes	36.1%	36.3%	37.1%
Dune lake	34.7%	34.9%	36.3%
Lagoon	46.3%	47.3%	49.0%
			47.6%

921 2.4 RESULTS

922 The overall sediment budget of the Sand Motor domain is determined given mor-
 923 phological change in the net aeolian erosion and net aeolian deposition zones for the
 924 period between September 1, 2011 and September 1, 2015 (Figure 2.4).

925 2.4.1 *Morphological change and porosity*

926 The net morphological change within the 3 m+MSL contour can be accredited en-
 927 tirely to aeolian sediment transport as this area is not significantly affected by marine
 928 processes since the construction of the Sand Motor. Also the net contribution of along-
 929 shore sediment fluxes are assumed to be relatively small given that the beach width
 930 (< 100 m) is small compared to the alongshore span of the measurement domain (4
 931 km). Within the 3 m+MSL contour sediment is deposited in the dunes and eroded
 932 from the aeolian zone.

933 The morphological change in the dune lake and the closed end of the lagoon is
 934 assumed to be driven predominantly by wind. Hydrodynamic forcing and conse-
 935 quently marine deposits in these zones diminished quickly over time, while significant
 936 amounts of fine aeolian deposits are found along the southwestern to northwestern
 937 shores.

938 The aeolian contribution to the morphological change in the mixed zones cannot be
 939 determined directly due to the presence of both marine and aeolian forces. However,
 940 by balancing the changes in sediment volume in the net aeolian deposition zones with
 941 the changes in sediment volume in the net aeolian erosion zones the aeolian sediment
 942 supply from the mixed zones is estimated.

943 18 porosity measurements from six zones (Table 2.2) are used to convert all mea-
 944 sured sediment volumes to a hypothetical porosity of 40%.

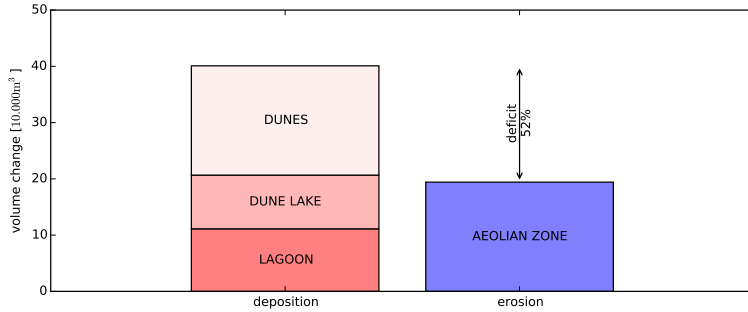


Figure 2.5: Aeolian sediment budgets in the Sand Motor domain in the period between September 1, 2011 and September 1, 2015.

945 2.4.2 Aeolian sediment budgets

946 The aeolian zone consistently provides less sediment than is deposited in the dunes,
 947 dune lake and lagoon (Figure 2.5). Over the four years since construction of the
 948 Sand Motor the volume deficit accumulates to $21 \cdot 10^4 \text{ m}^3$, which is 52% of the total
 949 sediment accumulation of $40 \cdot 10^4 \text{ m}^3$. The total wind transport capacity (or cumu-
 950 lative theoretical sediment transport volume) in this period is roughly estimated as
 951 $110 \cdot 10^4 \text{ m}^3$ (Appendix A). As the actual sediment transport rates appear to be only
 952 about 35% of the wind transport capacity, the Sand Motor can be classified as an
 953 availability-limited system.

954 Late January 2012, the surveys show a net volume deficit of zero, while subsequent
 955 surveys show a more or less linear growth of the volume deficit (Figure 2.6). Fitting
 956 a linear trend reveals an average growth rate of $5.2 \cdot 10^4 \text{ m}^3/\text{yr}$, which is 67% of
 957 the total sediment accumulation rate of $7.7 \cdot 10^4 \text{ m}^3/\text{yr}$ ($R^2 = 0.96$). The increase
 958 in growth rate of the volume deficit is likely caused by a significant decrease of the
 959 sediment contribution from the aeolian zone. The erosion from the aeolian zone in
 960 the first half year after construction of the Sand Motor exceeds the total erosion in the
 961 four years thereafter, while sediment continued to be accumulated in the dunes, dune
 962 lake and lagoon. The surface area of the aeolian zone decreased continuously (Figure
 963 2.7).

964 The diminishing of the aeolian sediment supply from the aeolian zone is also re-
 965 flected in the average bed level within the 3 m+MSL contour of September 22, 2015
 966 (Figure 2.8). The bed level within this contour has been almost constant since the
 967 volume deficit started to grow steadily from late January 2012. Only a few periods
 968 of significant erosion can be distinguished that can be related to storm events. Most
 969 notably, the event of December 5, 2013 with wind speeds up to 34 m/s. That day
 970 $1.5 \cdot 10^4 \text{ m}^3$ of sediment was eroded from within the 3 m+MSL contour of Septem-
 971 ber 22, 2015, which is 52% of the total erosion that year. Although this event is among
 972 the few events during which the runup levels exceeded the 3 m+MSL level (Figure
 973 2.2), the erosion can still be accredited to wind as the 3 m+MSL contour of September
 974 22, 2015 was located about 100 m landward of the 3 m+MSL contour at the time of the

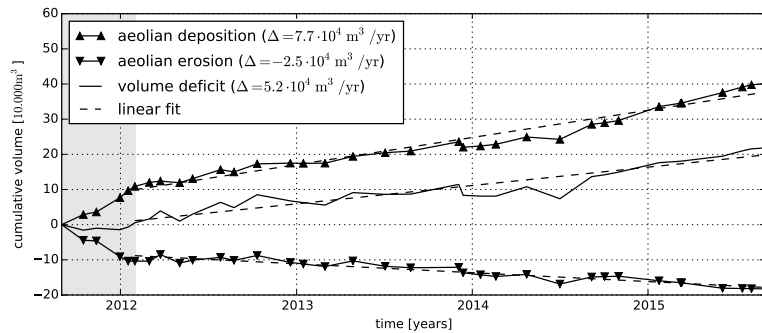


Figure 2.6: Cumulative change in sediment volume of all net aeolian erosion and net aeolian deposition zones and the volume deficit. For the linear fit the period prior to February 2012 is discarded (shaded).

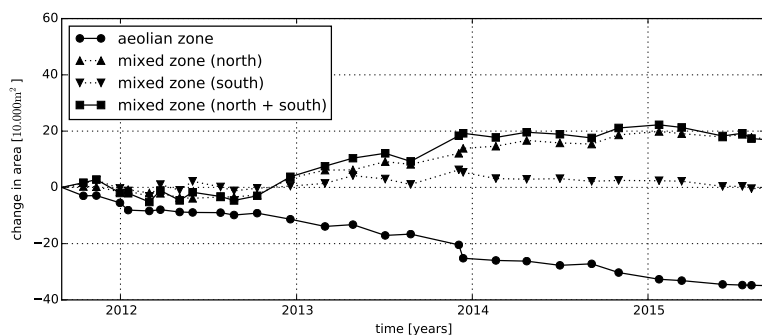


Figure 2.7: Change in size of aeolian zone and mixed zones since construction of the Sand Motor in 2011.

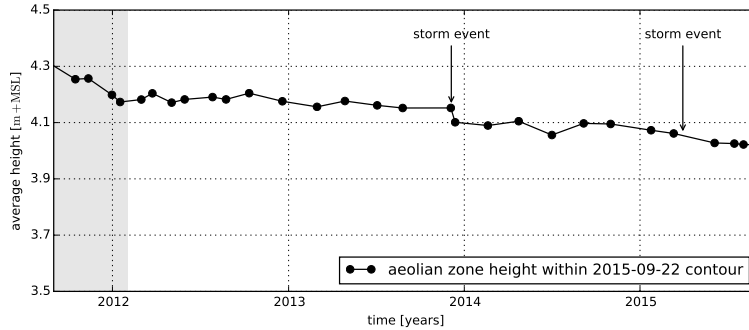


Figure 2.8: Average height of the aeolian zone in the most recent contour.

975 storm event. Therefore the bed level in the more recent contour was not affected by
976 the surge, which is confirmed by observations from a local permanent camera station.

977 In general, the use of the 3 m+MSL contour as divide between the areas with and
978 without marine influence appears to be valid for almost the entire four years after
979 construction of the Sand Motor. Only four events have been registered in which runup
980 levels exceeded the 3 m+MSL level (Figure 2.2). Observations from a local permanent
981 camera station indicate that only during the event of December 5, 2013 the surface of
982 the aeolian zone was significantly affected by tides and waves. Pre- and post-storm
983 topographic surveys that are available for this event indicate that the marine erosion
984 from the flooded areas above the 3 m+MSL level was less than $1 \cdot 10^4 \text{ m}^3$.

985 2.4.3 Alongshore variation

986 The sediment deposits in the dunes show an alongshore variation. A depression in
987 dune growth is observed in the lee of the dune lake and lagoon (Figure 2.9). South of
988 the dune lake and in between the dune lake and lagoon a passage for aeolian sediment
989 transport is present, which seems to result in a locally elevated dune growth. The
990 average dune growth of $14 \text{ m}^3/\text{m}/\text{yr}$ in the Sand Motor domain is low compared to
991 the dune growth rate along the adjacent southern ($15 \text{ m}^3/\text{m}/\text{yr}$) and northern (19
992 $\text{m}^3/\text{m}/\text{yr}$) beach stretches. However, aeolian deposits in the dune lake and lagoon
993 are of the same order of magnitude resulting in a total average sediment deposition of
994 $27 \text{ m}^3/\text{m}/\text{yr}$ in the Sand Motor domain, which is on average 56% higher than along
995 the adjacent coasts.

996 2.5 DISCUSSION

997 The volume deficit between the net aeolian erosion and net aeolian deposition zones
998 can be accredited to the mixed zones that are affected by both marine and aeolian
999 processes. The mixed zones in the Sand Motor domain are consequently estimated to
1000 provide 67% of the aeolian sediment in the Sand Motor domain. The aeolian sediment
1001 supply from the mixed zones is therefore significant, but still small compared to the

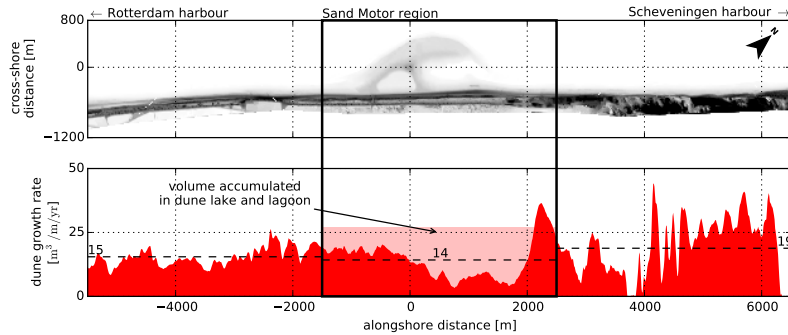


Figure 2.9: Comparison sediment accumulation rates in dunes (>3 m+MSL) for Sand Motor domain and adjacent coasts. Airborne lidar measurements from January 2012 until January 2015 are used. Horizontal dashed lines indicate local averages. The box indicates the Sand Motor domain depicted in previous figures.

98% reported by Jackson et al. (2010). The importance of the mixed zone cannot be explained by the size of the surface area as the mixed zones are initially smaller than the other main sediment source: the aeolian zone (Figure 2.7). Only from 2013 onward the surface area of the mixed zones exceed the area of the aeolian zone. However, the increase in surface area of the mixed zones is concentrated in the north where a low-lying spit develops (Figure 2.4). Given the dominant south to southwesterly wind direction and their position with respect to the lagoon that separates the spit from the dunes, it is unlikely that these intertidal beaches, provide a significant amount of sediment to dunes, dune lake and lagoon. Therefore, despite the periodic flooding and a size that is 40% – 60% smaller than the aeolian zone, the mixed zone (south) appears to provide the majority of the aeolian sediment in the Sand Motor domain.

2.5.1 Sources of inaccuracies

By accrediting the volume deficit to the mixed zones it is assumed that no sediment is exchanged over the boundaries of the Sand Motor domain and the sediment volume balance is thus closed. This assumption is not strictly valid, but the external sediment exchange with the Sand Motor domain is limited compared to the total sediment accumulation of $40 \cdot 10^4$ m³.

The predominantly southwesterly wind direction might blow sediment over the lateral borders that is not taken into account. However, the net alongshore sediment supply to the Sand Motor domain is estimated to be two orders smaller than the net onshore sediment supply, or less than 1% of the total sediment accumulation (Figure 2.10), because:

1. The onshore and alongshore sediment flux *per meter width* are estimated to be of the same order of magnitude (Appendix A), but the lateral beach cross-section (< 100 m) through which the alongshore flux enters the Sand Motor domain

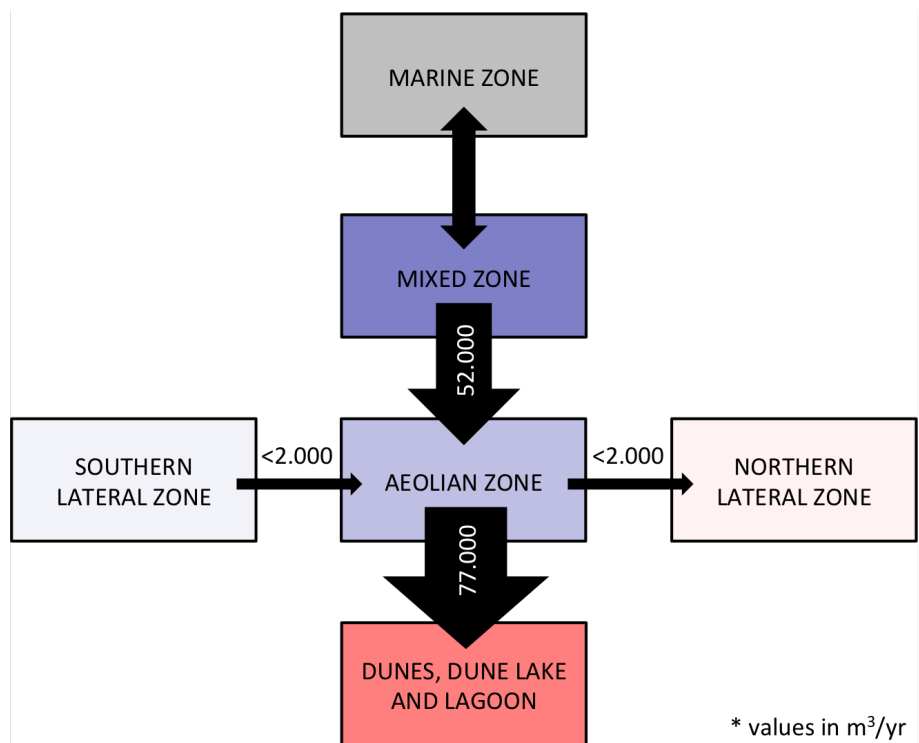


Figure 2.10: Aeolian sediment budget analysis of the Sand Motor

at the southern border is an order of magnitude smaller than the alongshore span of the Sand Motor domain (4 km) through which the onshore flux enters the domain. Therefore, the absolute alongshore contribution to the total sediment volume balance is likely an order of magnitude smaller than the onshore contribution.

2. The contribution of the net alongshore sediment flux that enters the Sand Motor domain at the southern border is at least partially compensated by a net alongshore sediment flux of the same order of magnitude that leaves the domain at the northern border. Therefore, the contribution to the total sediment volume balance of the southern and northern alongshore sediment fluxes combined (alongshore sediment transport gradient) is likely two orders of magnitude smaller than the contribution of the onshore sediment flux.

In reality the contribution of the alongshore sediment fluxes is likely to be even smaller as the sediment fluxes can locally be more onshore directed due to local wind steering. In addition, the estimates of the order of magnitude of the sediment fluxes are likely to be overestimated as possible limitations in sediment availability are ignored.

The influence of marine deposits in the lagoon is estimated to be less than 4% of the total sediment accumulation. 85% of the deposited sediment in the lagoon has the form of a southwesterly infill protruding above water and consisting of loosely packed, fine sediment and is therefore likely from aeolian origin (Figure 2.4 and Table 2.2). 15% of the deposited sediment in the lagoon, or 4% of the total sediment accumulation, is spread over a wider area and is possibly from marine origin.

The influence of marine erosion of the aeolian zone during the limited number of storm surges is estimated to be less than $1 \cdot 10^4 \text{ m}^3$ (Section 2.4.2), or 2.5% of the total sediment accumulation. Similarly, the influence of the changing size of the aeolian zone is estimated to be 2% of the total erosion in this area (Section 2.3.2), or less than 1% of the total sediment accumulation.

In summary, the error that is introduced by assuming a closed sediment volume balance is estimated to be less than 9% of the total sediment accumulation. The volume deficit of 67% of the total sediment accumulation that is accredited to aeolian erosion from the mixed zones therefore needs to be nuanced and is estimated to be more than 58%.

2.5.2 Beach armoring

The relative importance of the mixed zones for aeolian sediment supply can likely be explained by a visually observed beach armor layer that developed in the aeolian zone since construction of the Sand Motor. A beach armor layer can reduce the availability of aeolian sediment significantly (McKenna Neuman et al., 2012). Because the Sand Motor was constructed several meters above common storm surge level, the aeolian zone has never been influenced by waves or tides. Consequently, no process is present that regularly resets the armor layer, except for the occasional high-energy wind event. Moreover, salt crusts that form due to salt spray have a similar effect on the sediment availability as an armor layer. Small concentrations of salt ($\leq 7 \text{ mg/g}$) can already reduce the sediment availability by a factor two (Nickling and Ecclestone, 1981).

1071 In contrast, no beach armor layer or salt crusts develop in the mixed zones as pe-
1072 riodic flooding and related wave-reworking regularly deposit marine sediments, mix
1073 the top layer of the bed, and wash shells and shell fragments away. In addition,
1074 onshore bar migration and welding periodically provide additional unarmored sed-
1075 iment that can be entrained by the wind during low water (Houser, 2009; Anthony,
1076 2013). However, aeolian sediment availability in the mixed zones is also limited due
1077 to the relatively high soil moisture contents in these areas. Also soil moisture content
1078 is known to increase the shear velocity threshold (Wiggs et al., 2004; Edwards and
1079 Namikas, 2009; Namikas et al., 2010) and limit the local aeolian sediment availability.
1080 Given that the mixed zones appear to be a more important supplier of aeolian sedi-
1081 ment than the aeolian zone, limitations in sediment availability due to beach armoring
1082 seems to outweigh limitations due to high moisture contents.

1083 During a storm event even shell fragments and shells can be mobilized. Conse-
1084 quently, the beach armor layer itself might be transported and its reducing effect on
1085 the sediment availability is (partially) neutralized. Storm events are regularly accom-
1086 panied with surges that prevent wind erosion of the mixed zones. Entrainment of
1087 sediment therefore starts at a relatively high point along the fetch and much of the
1088 sediment transport capacity can be used for erosion of the aeolian zone, which con-
1089 tributes to the removal of the beach armor layer. If the surge is high enough it can
1090 also remove the beach armor layer by wave action or bury it by deposition of marine
1091 sediments. The removal or burial of the beach armor layer can elevate sediment avail-
1092 ability from the aeolian zone also after the the storm passed. Only after development
1093 of a new beach armor layer the sediment availability and transport rates approach the
1094 pre-storm situation.

1095 2.5.3 *Mega nourishments as coastal protection*

1096 The Sand Motor mega nourishment shows a morphological development that is signif-
1097 icantly different from natural beaches or the original Delfland coast. Aeolian sediment
1098 supply at the Sand Motor shows larger spatial variations compared to natural beaches,
1099 while dune growth rates lag behind compared to the adjacent coastal stretches. It can
1100 be questioned if such exotic behavior is desired for a coastal protection that aims
1101 to stimulate natural processes, or that, for example, it would be beneficial not to
1102 construct future mega nourishments above local storm surge level and prevent com-
1103 partmentalization of the beach.

1104 In this context, it is interesting to consider what would happen if the Sand Motor
1105 was constructed up to local storm surge level (3 m+MSL). The vast aeolian zone would
1106 not exist as the entire Sand Motor would be flooded at least once a year. Compart-
1107 mentalization would be minimized and aeolian sediment availability be maximized as
1108 the formation of deflation lag deposits is counteracted by wave-reworking. The dune
1109 lake and lagoon would be filled in up to three times faster due to transport-limited
1110 aeolian sediment supply. Soon, all aeolian sediment transport pathways would end
1111 in the dunes, resulting in an up to six times larger dune growth than currently ob-
1112 served. Marine sediment transport would enhance these relatively rapid changes as
1113 more sediment is redistributed within the Sand Motor domain to the lagoon, dune
1114 lake and offshore by overwash.

1115 A lower construction height of the Sand Motor would therefore result in a more
1116 rapid and more localized redistribution of sediment. Both rapid and localized redis-
1117 tribution are at odds with the purpose of the Sand Motor to nourish the entire Holland
1118 coast over a period of two decades. The static behavior of the supratidal areas of Sand
1119 Motor might therefore prove to be a crucial design criterion of a mega nourishment.

1120 2.6 CONCLUSIONS

1121 A sediment budget analysis is used to identify spatial variations in aeolian sediment
1122 deposition and supply, and dune growth in the Sand Motor domain. From the analy-
1123 sis the following conclusions can be drawn regarding aeolian sediment transport and
1124 supply in the Sand Motor domain:

- 1125 1. The (southern) low-lying beaches that are affected by both aeolian and marine
1126 processes (mixed zone) currently supply more than 58% of all aeolian sediment
1127 deposits in the Sand Motor domain, despite that this area is periodically flooded
1128 and 40% – 60% smaller than the upper dry beach areas (aeolian zone) that
1129 are only affected by aeolian processes and supply less than 42% of the aeolian
1130 deposits;
- 1131 2. The aeolian sediment supply from the aeolian zone diminished in the first half
1132 year after construction of the Sand Motor, likely due to the development of a
1133 beach armor layer;
- 1134 3. The aeolian sediment supply from the aeolian zone tends to increase temporar-
1135 ily during and after a storm event, likely due to (partial) removal of the beach
1136 armor layer;
- 1137 4. The dune growth in the Sand Motor domain is low compared to the adjacent
1138 coasts, likely due to blocking of aeolian sediment transport pathways by the
1139 dune lake and lagoon.

1140 From the analysis the following conclusions can be drawn regarding mega nourish-
1141 ments in general:

- 1142 1. The construction height should be a design criterion of any mega nourishment
1143 as it governs compartmentalization of the beach due to beach armoring;
- 1144 2. Compartmentalization of the beach can influence the lifetime and region of in-
1145 fluence of a mega nourishment as it affects the balance between local aeolian
1146 deposition and regional marine spreading of sediment.
- 1147 3. The consequences of compartmentalization is not yet fully understood as the
1148 contribution of the upper dry beach (aeolian zone) to local aeolian sediment
1149 supply can range from 42% as observed at the Sand Motor to less than 2% as
1150 reported by Jackson et al. (2010).

3

1151

1152

1153 SMALL SCALE SEDIMENT TRANSPORT

1154 This chapter is based on a previous publication: Hoonhout, B. M. and de Vries, S. (2016c).
1155 Field measurements on spatial variations in aeolian sediment availability at the sand motor
1156 mega nourishment. Aeolian Research. Submitted.

1157 **3.1 INTRODUCTION**

1158 The Sand Motor (or Sand Engine) is an innovative solution to counteract the anticipated coastal recession due to sea level rise (Stive et al., 2013). The Sand Motor is a 21
1159 Mm³ mega nourishment along the Dutch coast that is constructed well above storm
1160 surge level and therefore largely shaped by wind. While the Sand Motor accommodates fetches up to 1.0 km and is permanently exposed to wind, the dry surface
1161 area is remarkably stable (Hoonhout and de Vries, 2016a). An armor layer consisting
1162 of shells, pebbles and cobbles prevent erosion by wind and thus limit the sediment
1163 availability (following the definition of Kocurek and Lancaster, 1999). Consequently,
1164 the aeolian sediment transport rates at the Sand Motor are limited to approximately
1165 35% of the wind transport capacity (Hoonhout and de Vries, 2016a) making the Sand
1166 Motor an availability-limited coastal system.
1167

1168 In an availability-limited coastal system, not the wind transport capacity, but the
1169 sediment availability governs the sediment supply towards the dunes (Houser and Ellis, 2013). Sediment availability can be limited by various bed surface properties, like
1170 shells, salt crusts, moisture and vegetation. Studies on the influence of bed surface
1171 properties on aeolian sediment availability and transport started as wind tunnel experiments
1172 (e.g. Belly, 1964; Howard, 1977; Dyer, 1986; Gillette and Stockton, 1989). These
1173 studies typically determine an adapted threshold velocity that relates the theoretical
1174 wind transport capacity to a measured sediment transport capacity (Bagnold, 1937a).
1175 In the field, the influence of different bed surface properties on sediment availability
1176 cannot easily be distinguished and the sediment availability is often presented spatially aggregated (Jackson and Nordstrom, 1998; Arens et al., 2001; Wiggs et al., 2004).
1177 The concept of critical fetch is a widely used approach for spatial aggregation of sediment
1178 supply (e.g. Jackson and Cooper, 1999; Davidson-Arnott et al., 2005, 2008; Bauer
1179 et al., 2009). The critical fetch is the distance over which the saltation cascade develops
1180 and aeolian sediment transport becomes saturated (Bauer and Davidson-Arnott, 2002). Since the saltation cascade develops slower when sediment is scarce, the critical
1181 fetch is inversely proportional to the sediment supply (Delgado-Fernandez, 2010).

1182 Expressing the sediment supply in terms of critical fetch assumes that saturated
1183 transport is reached if the available fetch is sufficient. Hoonhout and de Vries (2016a)

1188 showed that sediment supply can be severely limited even with fetches as large as
 1189 at the Sand Motor. Consequently, critical fetches may become very large or even
 1190 undefined and the definition and interpretation of the critical fetch impractical (Lynch
 1191 et al., 2016; de Vries et al., 2014a). Moreover, significant spatial variations in sediment
 1192 supply were found in the Sand Motor region that challenges the spatial aggregation
 1193 of sediment availability. Alternatively, aeolian sediment transport is expressed in
 1194 terms of local sediment availability without the need for spatial aggregation (de Vries
 1195 et al., 2014b; Hoonhout and de Vries, 2016d). Such approach would require detailed
 1196 measurements on spatiotemporal variations in aeolian sediment availability.

1197 This paper presents detailed measurements of aeolian sediment transport rates
 1198 from the Sand Motor during a six week field campaign in the fall of 2014. Spatial
 1199 differences in sediment transport rates reveal the main erosion and deposition areas
 1200 of aeolian sediment. Temporal variations in aeolian sediment transport are still ex-
 1201 pected to be correlated with the wind speed, but spatial variations are expected to be
 1202 correlated with local variations in sediment availability. Understanding local sediment
 1203 availability ultimately helps improving gross aeolian sediment transport estimates in
 1204 availability-limited coastal systems.

1205 **3.2 FIELD SITE**

1206 The Sand Motor mega nourishment was constructed in 2011 along the Delfland coast
 1207 in The Netherlands (Figure 3.1, Stive et al., 2013). The Delfland coast was originally
 1208 characterized by an alongshore uniform profile with an average dune height of 13 m,
 1209 a dune foot at about 5 m+MSL and a beach slope of about 1:40.

1210 The Sand Motor is constructed as a 21 Mm³ hook-shaped peninsula that initially
 1211 protruded about 1 km into the sea and stretched over approximately 2 km alongshore.
 1212 The original crest height of the Sand Motor was on average about 5 m+MSL and lo-
 1213 cally 7 m+MSL; both are well above common surge level. Consequently, a significant
 1214 part of the Sand Motor is uniquely shaped by aeolian processes that redistribute sig-
 1215 nificant amounts of sediments within the Sand Motor region (Hoonhout and de Vries,
 1216 2016a).

1217 Sand used for construction of the Sand Motor is medium sand with a median di-
 1218 ameter of about 350 µm. The sand is obtained from an offshore borrowing pit in
 1219 the North Sea and contains many shells and some pebbles, cobbles and other non-
 1220 erodible material.

1221 The predominant wind direction is south to southwest. Storms have a tendency to
 1222 be oriented either southwest or northwest. Also the sediment transport potential (Ψ),
 1223 defined as:

$$\Psi \propto \int u^3 dt \quad (3.1)$$

1224 in which u is the wind speed, is predominantly southwesterly or northwesterly ori-
 1225 ented. The northwesterly storms are generally accompanied with significant surges
 1226 as the North Sea is virtually unbounded in northwesterly direction (Figure 3.1b).

1227 The contour of the Sand Motor changed significantly in the four years after con-
 1228 struction. Tidal forces diffuse about 1 Mm³ per year along the coast (de Schipper

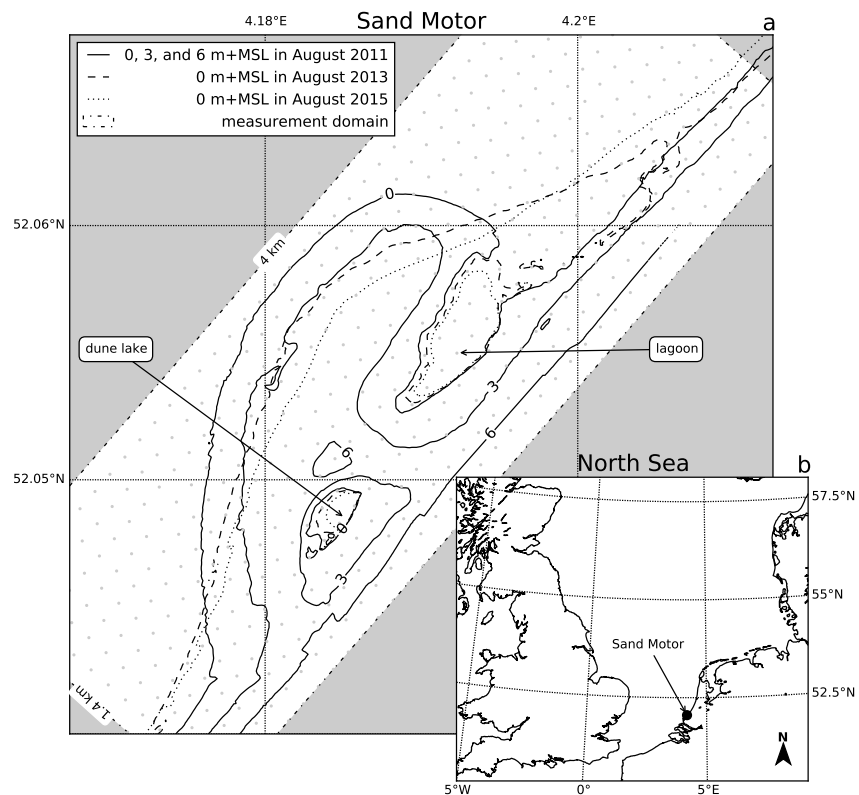


Figure 3.1: Location, orientation, appearance and evolution of the Sand Motor between construction 2011 and 2015. The box indicates the measurement domain used in the remainder of this paper. A 100 x 100 m grid aligned with the measurement domain is plotted in gray as reference.

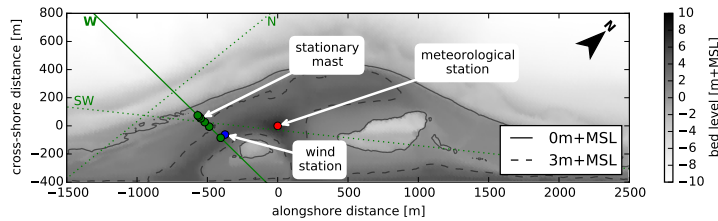


Figure 3.2: Overview of measurement transects N, W, and SW and locations during the MEGAPEX field campaign.

et al., 2016). Four years after construction, the peninsula protrudes about 800 m into the sea and stretches over 4 km alongshore (Figure 3.1).

The Sand Motor provides a unique opportunity to perform measurements on spatial variations in aeolian sediment availability and transport. It accommodates vast and armored beaches next to dynamic intertidal beaches of varying width, while limitations in fetch are negligible.

3.3 METHODOLOGY

Sediment transport measurements were performed to investigate the role of the southern intertidal beaches as supplier of aeolian sediment in the Sand Motor region (Hoonhout and de Vries, 2016a). The change in sediment transport in downwind direction (spatial gradient) was measured along cross-shore transects running from the water line until the dry beach at approximately 5 m+MSL. Spatial gradients in saltation transport are positive in areas with net erosion and negative in areas with net deposition of sediment. The measurements were performed during the six week field campaign MEGAPEX (Mega Perturbation EXperiment) from September 17, 2014 until October 23, 2014.

3.3.1 Equipment

The measurement set-up consists of 8 masts with battery power and data loggers. Each mast was equipped with at least three Wenglor fork laser sensors (P/N: YHo8PCT8) for saltation measurements at 3, 10 and 25 cm above the bed (Figure 3.3). An additional three laser sensors were added to the most landward mast at 40, 55 and 70 cm above the bed to estimate the amount of particles bypassing the lower three sensors. Other masts could be equipped with three additional laser sensors as well. All except the lowest sensor were placed horizontally with the arms directed towards the wind as to minimize the disturbance of the wind field. The lowest sensor was placed vertically with the arms directed upwards, and partially buried as to further

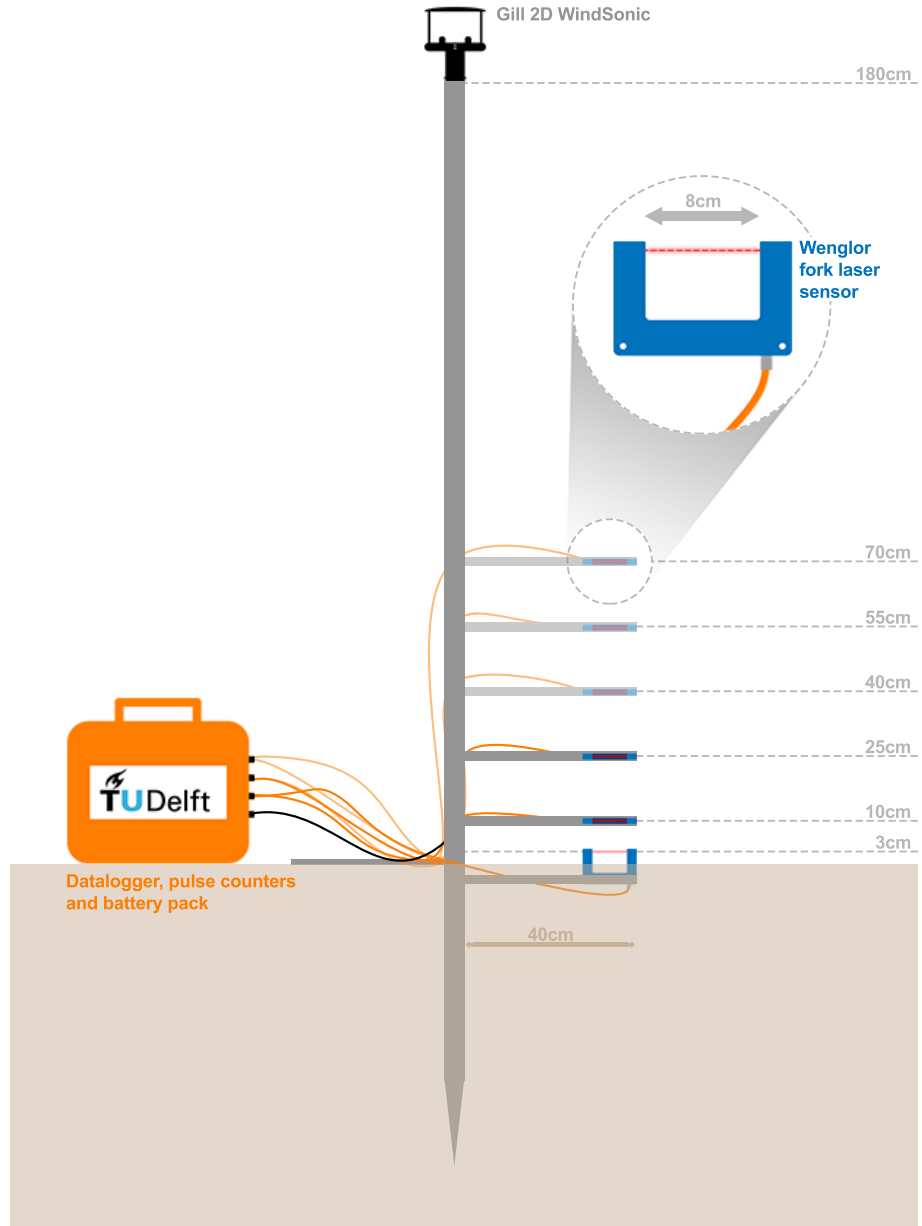


Figure 3.3: Mast with 6 Wenglor fork laser sensors and a Gill 2D WindSonic ultrasonic wind speed and direction sensor viewed in direction of the wind. The top 3 laser sensors are optional.

1255 minimize the disturbance of the wind field. The Wenglor fork laser sensors register
1256 passing particles of 50 µm and larger with a frequency of 10 kHz using a laser beam
1257 of 0.6 mm. As the particle count is linearly related to the sediment flux ([Hugenholz and Barchyn, 2011](#)), both are used indiscriminately in this study. The particle count is
1258 accumulated by a HOBO pulse counter (P/N: S-UCC-Moo1). A HOBO Energy data
1259 logger (P/N: H22-001) logged all sensors, including the pulse counters, at 1 Hz. In
1260 addition, three masts were equipped with a Gill 2D WindSonic ultrasonic wind speed
1261 and direction sensor (P/N: 1405-PK-040) at a height of 180 cm above the bed.
1262

1263 The masts can be rotated, but are not self-rotating to the wind as the masts were
1264 relocated depending on the wind direction. One stationary mast was present during
1265 almost the entire field campaign (Figure [3.2](#)).

1266 A separate Eijkelkamp wind station with three cup anemometers (P/N: 16.98.31)
1267 at heights 50, 100 and 180 cm and a wind vane (P/N: 16.98.34) at height 180 cm was
1268 present at a stationary location at the high beach for the entire duration of the field
1269 campaign. A Campbell Scientific meteorological station was present at the heart of
1270 the Sand Motor providing measurements on precipitation, humidity, solar radiation
1271 and wind speed and direction (Figure [3.2](#)).

1272 Qualitative small scale measurements on bed level change were performed by press-
1273 ing erosion pins (nails) in the beach with falling tide. The erosion pins were placed
1274 along a cross-shore transect and about 10 cm apart with their heads flush to the bed.
1275 The erosion around the pins was measured manually with a ruler at the onset of flood.

1276 Daily topographic surveys are performed along cross-shore transects using a Leica
1277 Viva GS10 RTG-GPS receiver. Offshore water levels and wave heights are obtained
1278 from gauges at the permanent offshore Europlatform.

1279 3.3.2 Deployments

1280 The measurement masts were deployed continuously during the field campaign, but
1281 have been relocated according to the governing wind direction. An overview of the
1282 measurement locations is given in Figure [3.2](#).

1283 A single measurement transect consists of at least four masts: two in the intertidal
1284 beach area in order to capture the entrainment rate from the assumed sediment source
1285 region, one above the high water mark to capture the sediment flux from the intertidal
1286 beach area onto the dry upper beach and one higher up the beach to capture any
1287 additional sediment supply from the dry beach itself.

1288 Table [3.1](#) lists the partitioning of the field campaign in 10 deployments with constant
1289 location and orientation of the measurement equipment. Most deployments were
1290 located along the westerly transect at the southern flank of the Sand Motor (Figure [3.2](#)).
1291 Deployments DNo2a and DNo6a were aligned along alternative transects concurrent
1292 with deployments DNo2b and DNo6b respectively. During deployment DN11 all
1293 masts were clustered at high grounds as to provide a safe buffer from the expected
1294 surge during the storm event of October 23. Consequently, no transport gradients
1295 were measured during deployment DN11.

Table 3.1: Deployments of measurement masts during the MEGAPEX field campaign.
Maximum measured wind speeds are in between brackets.

	wind speed [m/s]	wind dir. [°]	laser dir. [°]	transect	duration [h]	sensors [-]	well oriented* [%]
DNo2a	3 (10)	358	262	W	22	3	0
DNo2b	3 (10)	359	360	N	22	3	100
DNo4	5 (13)	343	360	W	42	3	92
DNo5	3 (15)	196	270	W	312	3	40
DNo6a	5 (17)	166	225	SW	170	3	55
DNo6b	5 (17)	180	225	W	170	3	77
DNo8	5 (16)	199	225	W	160	6	89
DNo9	9 (21)	240	270	W	32	6	87
DNo10	15 (22)	301	315	W	9	6	100
DNo11	10 (24)	322	315	-	25	6	44

* The last column indicates the percentage of time in which the laser sensors were well oriented with respect to the wind. Raw data from all deployments is published as Hoonhout et al. (2016c). DNo1 is omitted from this list as it involved a test run of the equipment only. DNo2a is listed only for convenience when interpreting the published dataset. DNo2b and DNo6b were originally named DNo3 and DNo7 respectively and can be found by these names only in the published dataset.

1296 3.3.3 Data analysis

1297 Particle count time series obtained from individual Wenglor laser sensors are summed
1298 up

- 1299 1. per mast, to obtain *per-mast* particle count time series for each measurement
1300 mast, and
- 1301 2. over all masts, to obtain *overall* particle count time series over all measurement
1302 masts.

1303 The per-mast particle counts are totaled rather than averaged, and therefore not cor-
1304 rected for the number of Wenglor laser sensors per mast. All masts deployed sim-
1305 taneously in a single transect were equipped with an equal number of sensors. Only
1306 the most landward mast in the westerly transect was permanently equipped with six
1307 sensors. However, the upper three sensors of the latter mast registered negligible par-
1308 ticle counts. Averaging would result in approximately halving the per-mast particle
1309 counts. The halving of the particle count does not reflect any physical behavior and is
1310 therefore averted. Particle count time series are interchangeably referred to as particle
1311 count rates as the measurement interval was 1 Hz.

1312 The overall particle count time series are used for comparison with the governing
1313 wind speed. For comparison with the wind direction per-mast particle count time
1314 series are discretized in bins according to the governing wind direction and subse-
1315 quently summed over time. Also for comparison with water and bed levels, the
1316 per-mast particle count time series are discretized in bins and summed over time. Dis-
1317 cretization is then done according to the global water level and local bed level at the
1318 measurement location.

1319 Horizontal gradients in particle counts are computed from the per-mast particle
 1320 count time series and the distance between the measurement masts. Vertical distribu-
 1321 tions in particle counts are computed from the per-sensor particle count time series
 1322 for each measurement mast.

1323 Particle counts are converted into sediment fluxes following Barchyn et al. (2014a):

$$q_{\text{wenglor}} = n_{\text{wenglor}} \left(\frac{6 \cdot \gamma}{\rho \pi D^3} \cdot l_{\text{fork}} \cdot (l_{\text{laser}} + D) \right)^{-1} \quad (3.2)$$

1324 with $\rho = 2650 \text{ kg/m}^3$, $l_{\text{fork}} = 8 \cdot 10^{-2} \text{ m}$, $l_{\text{laser}} = 6 \cdot 10^{-4} \text{ m}$, $D = 335 \text{ m}$ and
 1325 $\gamma = 1$.

1326 Variations in wind direction of more than 45° resulted in adjustment of the ori-
 1327 entation of the Wenglor fork laser sensors. Particle counts with a discrepancy between
 1328 wind direction and laser orientation ($\Delta\theta_u$) of more than 60° are considered not well
 1329 oriented and are discarded from the presented analysis. Other particle counts (n_{pc})
 1330 are corrected for orientation inaccuracies (\hat{n}_{pc}) using the basic geometric correction:

$$\hat{n}_{pc} = \frac{n_{pc}}{\cos(\Delta\theta_u)} \quad (3.3)$$

1331 Periods without significant particle counts are not discarded from the analysis, ex-
 1332 cept for the determination of the average wind direction as the wind direction tends
 1333 to show random behavior for low wind conditions. The last column in Table 3.1 states
 1334 the percentage of time in the laser sensors were well oriented with respect to the wind
 1335 direction.

1336 3.4 RESULTS

1337 The conditions during the field campaign were characterized by calm and sunny
 1338 weather and negligible precipitation, which is unusual for the time of the year. The
 1339 average wind speed over the entire experiment was 6 m/s (Figure 3.4a). The maxi-
 1340 mum wind speed was registered at 24 m/s at the end of the campaign on October
 1341 23 during the only measured storm event (DN10). The average overall particle count
 1342 rate over the entire experiment was 120 s^{-1} or $< 0.1 \text{ kg/m}^2/\text{s}$ averaged over all de-
 1343 ployed sensors (Figure 3.4b). The maximum overall particle count rate was registered
 1344 on October 7 at 5800 s^{-1} or $4 \text{ kg/m}^2/\text{s}$ (DN06b). Therefore, the maximum registered
 1345 overall particle count rate did not coincide with the maximum wind speed.

1346 The experiment covered two spring-neap cycles with a tidal range varying between
 1347 1.5 and 2.0 m (Figure 3.4c). The maximum still water level of 2.8 m+MSL was mea-
 1348 sured during storm deployment DN11 on October 22. This surge flooded the southern
 1349 flank of the Sand Motor up to 5 m+MSL.

1350 3.4.1 Relation between sediment transport and wind speed and water level

1351 Periods with low wind conditions seem to coincide with periods with a negligible
 1352 overall particle count, whereas periods with fair wind conditions seem to coincide
 1353 with periods with a significant overall particle count (Figure 3.4a,b). Also the occur-
 1354 rence of peaks in overall particle count show a correspondence with peaks in wind
 1355 speed. However, the highest peaks in wind speed do not necessarily coincide with the

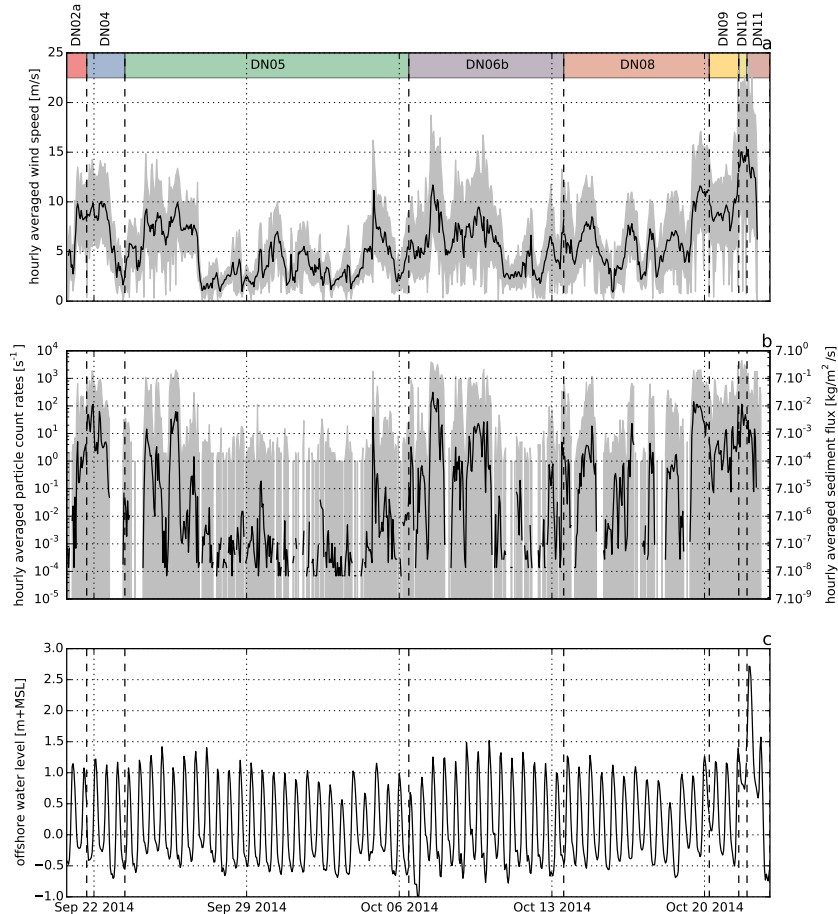


Figure 3.4: a) Wind time series, b) overall particle count rates during the deployments along the westerly transect, and c) offshore tidal elevation. Grey lines indicate the raw data, black lines the hourly averaged data. Colored bars refer to the deployments listed in Table 3.1. Deployments DN02b and DN06a are not included as these are located along different transects.

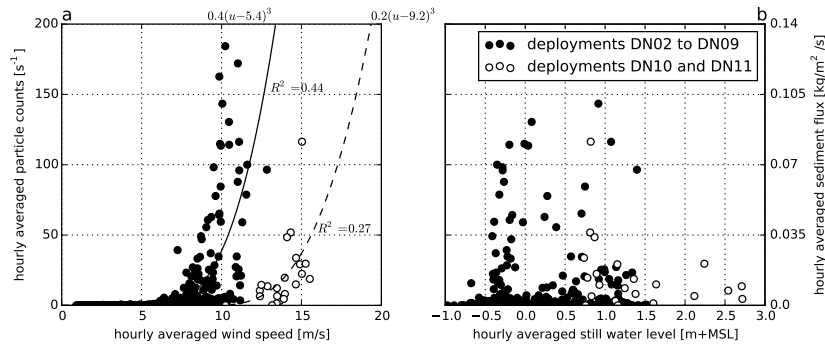


Figure 3.5: a) Relations between overall particle count and wind speed or b) water level. Closed circles and continuous lines refer to non-storm deployments DN02 to DN09. Open circles and dashed lines refer to storm deployments DN10 and DN11. All deployments are listed in Table 3.1.

1356 highest peaks in overall particle count, resulting in an overall poor correlation between
 1357 wind speed and overall particle count (Figure 3.5a). The poor correlation is reflected
 1358 in a Spearman rank correlation coefficient (Spearman, 1904) of zero, indicating that
 1359 the data cannot be described by a monotonic function of any kind.

1360 In the remainder of this paper it is shown that the storm deployments DN10 and
 1361 DN11 provide signals with respect to wind direction, sediment availability and fetch
 1362 that are consistently different from the non-storm deployments DN02 to DN09. In
 1363 anticipation to these findings, correlations between wind speed and overall particle
 1364 count are computed for the storm and non-storm deployments separately, resulting
 1365 in a weak positive relation between wind speed and overall particle count. Fitting
 1366 a third-power curve through these separate datasets results in R^2 -values of 0.43 and
 1367 0.27 respectively. The low R^2 -values indicate that much of the variance in the overall
 1368 particle count is not explained by wind speed.

1369 No relation between the still water level and the overall particle count is found
 1370 (Figure 3.5b). There is no evidence that the spring-neap modulation of the high water
 1371 level of about 0.5 m influenced the overall particle count significantly.

1372 3.4.2 Wind direction and sediment source areas

1373 The vast majority of per-mast particle counts registered at the stationary mast, that
 1374 was located at the high water line during almost the entire field campaign (Figure
 1375 3.2), was registered from a limited number of wind directions. These directions do
 1376 not coincide with the prevailing wind direction or the wind direction with the largest
 1377 transport potential (Figure 3.6a).

1378 Figure 3.6a shows that the prevailing wind direction was south, but that the largest
 1379 transport potential (Equation 3.1) came from the southwesterly and northwesterly
 1380 directions. The per-mast particle count does not align with the prevailing wind direc-

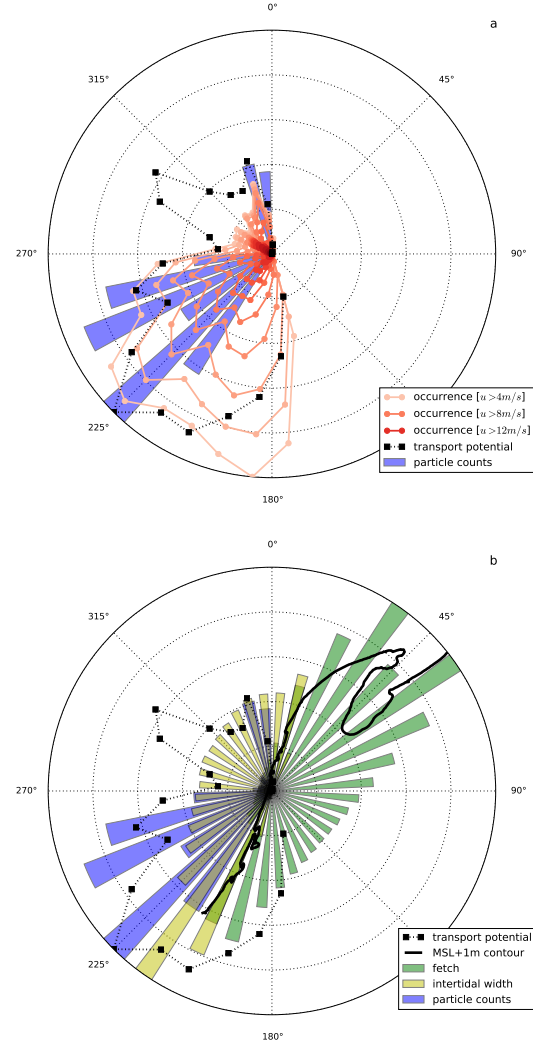


Figure 3.6: a) Per-mast particle count, wind speed and direction obtained from stationary mast (Figure 3.2) and b) available fetch and intertidal fetches.

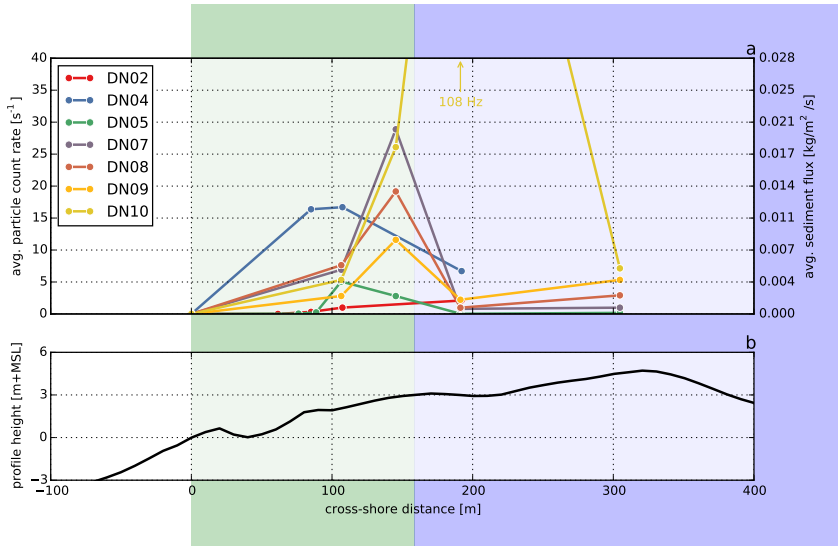


Figure 3.7: a) Average per-mast particle count rates during the deployments along the westerly transect and b) beach profile at the beginning of the field campaign. Line colors refer to the partitioning of the time series in Figure 3.4.

tion or the directions with the largest transport potential as both the southerly and northwesterly wind directions did not induce a significant particle count.

Figure 3.6b shows that most particles are registered from the wind directions with the shortest fetches. However, these wind directions provide among the largest intertidal beach widths along the Dutch coast. The exception is the northwesterly wind direction, that does accommodate a fair intertidal beach width, but did not register a per-mast particle count close to what could be expected from the transport potential. The northwesterly wind directions were solely present during the storm deployment DN10.

3.4.3 Spatial gradients in sediment transport

Significant variations in per-mast particle count along the measurement transects is found. Figure 3.7 shows that the largest increase in per-mast particle count in downwind direction (positive gradients) is consistently located in the intertidal beach area. Positive gradients in sediment transport indicate a net erosion of the beach surface and thus entrainment of sediment.

A significant decrease in per-mast particle count in downwind direction (negative gradients) is consistently found at the transition between intertidal and dry beach. Negative gradients in sediment transport indicate net deposition of sediment. Only during storm deployment DN10 the negative gradients at the transition were absent

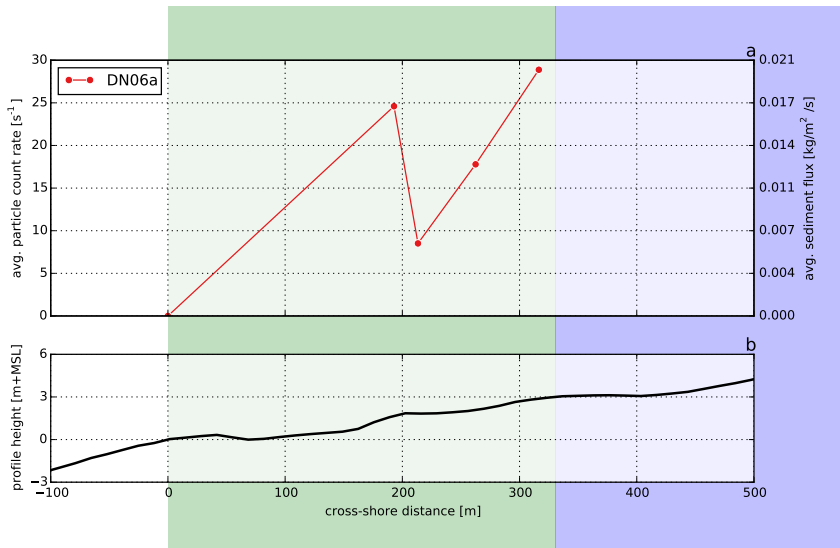


Figure 3.8: a) Average per-mast particle count rates during deployment DN06a along the southwesterly transect and b) beach profile at the beginning of deployment DN06.

1400 and large positive gradients in both the intertidal and dry beach area were found
1401 (Figure 3.7).

1402 The negative gradients coincide with the transition from the berm slope to the
1403 berm flat. Local deposition of aeolian sediment at the edge of a berm appears to
1404 be consistent behavior as it is also observed within the intertidal beach area.
1405 Four masts were deployed along a southwesterly transect within the intertidal beach area
1406 (DN06a, Figure 3.8) concurrent with deployment DN06b. These measurements show
1407 a significant decrease in per-mast particle count over a minor berm-like feature ($x =$
1408 200 m) in the intertidal beach area. Downwind of this feature the per-mast particle
1409 count increased again with a rate comparable to what was found upwind of the berm-
1410 like feature. In addition, small scale measurements on bed level change confirm that
1411 erosion by wind is concentrated on the berm slope (Figure 3.9), while the berm flat
1412 tends to accrete. The maximum erosion of 1.2 cm in a single tidal cycle was measured
1413 with wind speeds above 10 m/s and little precipitation.

1414 Measured negative gradients might also be caused by sediment locally bypassing
1415 the measurement equipment. To ensure that the number of bypassing particles is
1416 limited, the most landward mast in each transect was permanently equipped with
1417 six laser sensors up to 70 cm above the bed. The number of particles counted in the
1418 upper laser sensor was consistently low ($\leq 1\%$), suggesting that only a small number
1419 of particles bypassed the equipment at this point.

1420 At the location downwind of the negative gradients more sediment might have by-
1421 passed than at the most landward measurement location. During deployment DN08
1422 all four masts were equipped with six laser sensors in order to capture the vertical
1423 distribution of the particle count across the beach (Figure 3.10). It appears that the cen-

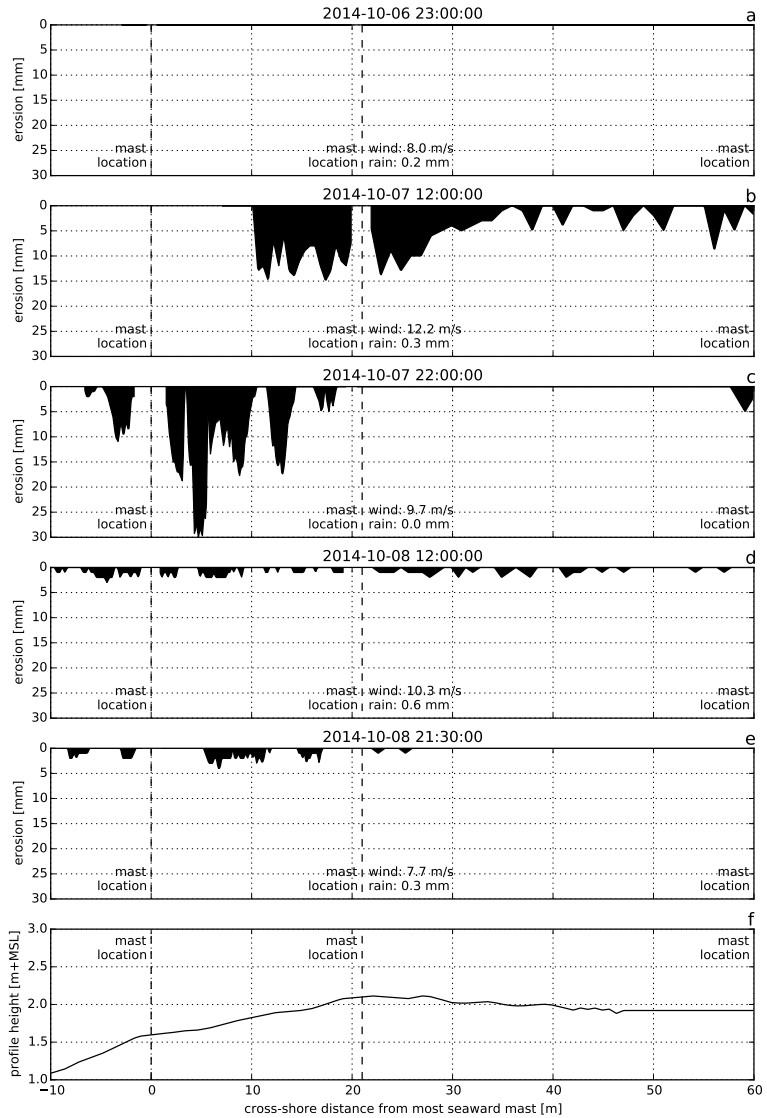


Figure 3.9: Erosion measured using erosion pins during five tidal cycles during deployment DNo6a along the southwesterly transect.

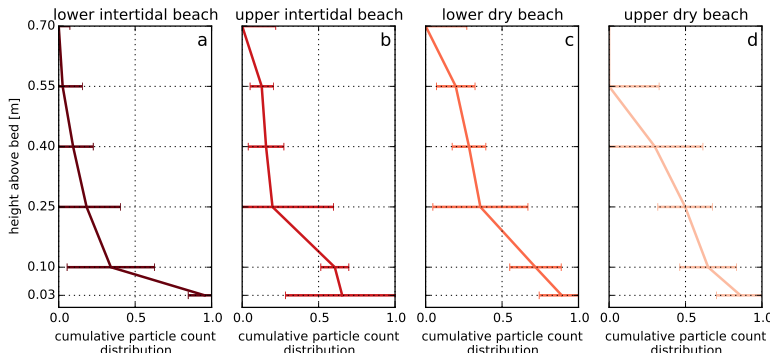


Figure 3.10: Cumulative particle count distribution over the vertical during deployment DNo8. The line indicates the percentage of particles that bypasses a certain height above the bed. The horizontal bars visualize the variability in time of the particle count per laser sensor.

1424 ter of gravity of the particle count moves upward in downwind direction. Downwind
 1425 of the negative transport gradient the percentage of particles counted by the upper
 1426 laser sensor is 20% compared to $\leq 10\%$ at the other locations, suggesting that most
 1427 particles bypassed at this location. The difference between the fraction of bypassing
 1428 particles is too small to explain the large negative gradients, but are likely to cause
 1429 the measured negative gradients to be overestimated.

1430 3.4.4 Fetch vs. sediment availability

1431 In Figure 3.11 the overall particle count obtained during the field campaign is binned
 1432 according to the prevailing wind speed and the bed level at the measurement location.
 1433 The average still water level is an indication of available fetch. The peak in overall par-
 1434 ticle count is at 3 m+MSL irrespective of the wind speed and available fetch. Therefore
 1435 the overall particle count seems to be limited by location rather than wind speed or
 1436 available fetch. The specific location at which the particle count peaks corresponds
 1437 to the high water line and the onset of the shell pavement that largely covers the dry
 1438 beach.

1439 3.5 DISCUSSION

1440 The positive gradients in per-mast particle count in the intertidal beach area and minor
 1441 positive gradients in the dry beach area suggest that the intertidal beach is a primary
 1442 source of aeolian sediment in the Sand Motor region. This observation is in accor-
 1443 dance with the large scale sediment budgets of the Sand Motor region (Hoonhout and
 1444 de Vries, 2016a). Armoring of the dry beach surface, due to formation of lag deposits,
 1445 might lead to a significant reduction in local aeolian sediment availability. Similarly,
 1446 sediment availability might also be limited in the intertidal beach area due to periodic
 1447 flooding and consequently high soil moisture contents. From the differences in per-

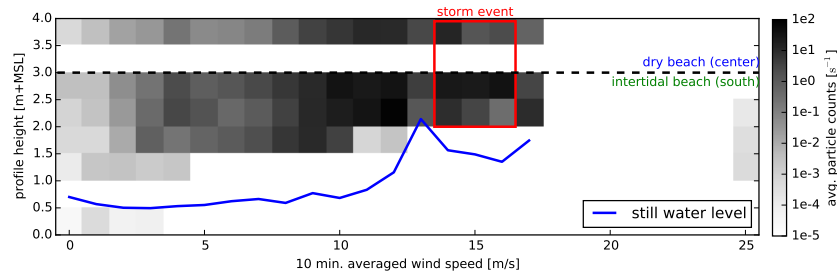


Figure 3.11: Average overall particle count rates depending on governing wind speed and bed level at measurement location, and average still water level depending on governing wind speed.



Figure 3.12: Visual impression of armor layer at three locations in the Sand Motor region: a) intertidal beach, no armoring b) lower dry beach, minor armoring with shell fragments c) upper dry beach, severe armoring with many shells and coarse sand. Covered surface is approximately 40 x 40 cm in all cases.

1448 mast particle count gradients between the intertidal and dry beach it can be assumed
 1449 that the reduction of sediment availability due to armoring outweighs the influence
 1450 of soil moisture. Local differences in bed surface properties would therefore induce
 1451 relative differences in sediment availability that govern aeolian sediment transport in
 1452 the Sand Motor region.

1453 The negative gradients in per-mast particle count at the transition between intertidal
 1454 and dry beach indicate that sediment eroded from the intertidal beach is deposited
 1455 locally on the dry beach. Morphological feedback with the wind might cause the
 1456 sediment transport capacity to peak at the berm edge due to the presence of a lo-
 1457 cally accelerated wind (i.e. jet flow; [Hesp and Smyth, 2016](#)), resulting in deposition at
 1458 the berm flat. In addition, the berm edge coincides with the visually observed onset
 1459 of a shell pavement (Figure 3.12). The shell pavement emerged from the nourished
 1460 sediment in the first half year after construction of the Sand Motor ([Hoonhout and](#)

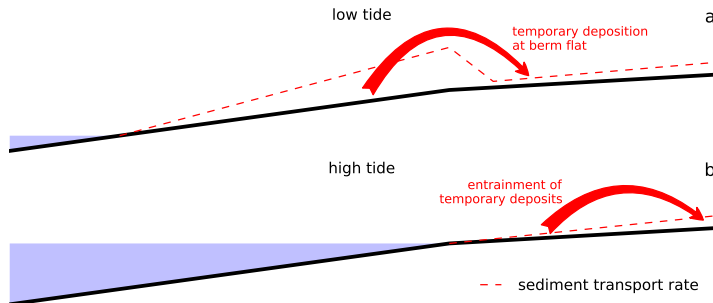


Figure 3.13: Conceptual illustration of how temporal deposits facilitate a continuous sediment supply from the intertidal beach to the dunes.

1461 de Vries, 2016a) due to winnowing of sand from the bed. Roughness elements, like
 1462 shells and cobbles, might trap impacting grains, and hamper saltation, or cause fully
 1463 elastic collisions, and enhance saltation. The shell pavement at the measurement lo-
 1464 cations is relatively open and therefore both processes are likely to be relevant. The
 1465 consistent negative gradients in particle count at the onset of the shell pavement sug-
 1466 gest that trapping of sediment is dominant over the enhancement of saltation due to
 1467 fully elastic collisions.

1468 The local deposition of sediment at the berm flat is temporary as no accumulation
 1469 of sand is observed on top of the shell pavement during the MEGAPEX field cam-
 1470 paign. This suggests that sediment supply from marine sources and deposition in
 1471 dunes, dune lake and lagoon is a phased process. In a phased system the local sed-
 1472 iment deposits at the berm flat might act as temporary sediment source during high
 1473 water (Figure 3.13). Consequently, measured aeolian sediment transport rates would
 1474 be continuous and independent of the instantaneous water level. The phasing of ero-
 1475 sion and deposition can therefore explain the weak correlations between measured
 1476 overall particle count and the instantaneous water level, which seemed to contrast the
 1477 conclusion that the intertidal beach is a primary source of aeolian sediment.

1478 The phasing of erosion and deposition increases the duration of transport from the
 1479 intertidal beach to the dunes. The environmental conditions therefore needs to be fa-
 1480 vorable for aeolian sediment transport over a longer period for the sediment to reach
 1481 the dunes. This requirement for dune growth closely relates to the need for synchro-
 1482 nization between sediment availability and wind transport capacity emphasized by
 1483 Houser (2009); Anthony (2013).

1484 During a high wind event the relative importance of limitations in sediment avail-
 1485 ability might change. Strong winds can mobilize even the largest sediment fractions
 1486 and shell fragments. Consequently, the beach armor layer itself might be transported
 1487 and its reducing effect on sediment availability might be (partially) neutralized. Also
 1488 the trapping of sediment due to an increase in bed roughness might be less effective
 1489 and the influence of the berm on the wind flow reduced. In addition, high wind
 1490 events are regularly accompanied with surges that prevent erosion of the intertidal
 1491 beach by wind. Instead, the wind energy can be used for erosion of the dry beach,

1492 which contributes to the removal of the beach armor layer. The surge itself might
1493 also remove the beach armor layer by wave action or bury it by deposition of marine
1494 sediments. The removal or burial of the beach armor layer might elevate sediment
1495 availability from the dry beach also after the the storm passed. Only after develop-
1496 ment of a new beach armor layer the sediment availability and transport rates then
1497 equal the pre-storm situation.

1498 The significant spatial variations in sediment transport gradients reflect significant
1499 variations in aeolian sediment availability. The formation of beach armor layers is
1500 known to limit aeolian sediment availability ([McKenna Neuman et al., 2012](#)) and cause
1501 spatial variations in aeolian sediment supply ([Jackson et al., 2010](#)). In case of the Sand
1502 Motor the formation of the beach armor layer is particularly accommodated by:

- 1503 1. the high number of shells and other roughness elements that is generally con-
1504 tained by nourishment sand ([van der Wal, 1998, 2000](#)), and
- 1505 2. the high construction height of the Sand Motor.

1506 As the majority of the Sand Motor's subaerial surface has never been influenced by
1507 hydrodynamics, the beach surface in these areas is never reworked. Consequently, the
1508 majority of the Sand Motor's subaerial surface does not directly contribute to dune
1509 growth or beach-dune interactions ([Houser and Ellis, 2013](#)). The vast beach surface
1510 seems to stimulate dune growth only indirectly by sheltering the dunes from storm
1511 erosion.

1512 Large scale nourishments are typically presented as natural solution to improve
1513 coastal safety. The natural dynamics of beach-dune systems depend on the periodic
1514 reworking of the beach surface as it prevents the formation of lag deposits. Large
1515 scale nourishments with a construction height above regular storm level can disrupt
1516 these natural dynamics as the formation of lag deposits is accommodated. The result-
1517 ing compartmentalization of the beach can result in a phased process that decelerates
1518 dune growth and make dune growth more dependent on incidental storm events.
1519 Besides, also marine erosion would likely be limited, contributing to the lifetime of
1520 the nourishment. In contrast, limiting the construction height of large scale nour-
1521 ishments would reduce the lifetime of a nourishment, but result in a larger source
1522 area of aeolian sediment and the stimulation of dune growth and natural beach-dune
1523 interactions.

1524 3.6 CONCLUSIONS

1525 The Sand Motor (or Sand Engine) is a 21 Mm³ mega nourishment along the Dutch
1526 coast that is constructed well above storm surge level ([Stive et al., 2013](#)) and therefore
1527 largely shaped by wind. During the six week MEGAPEx field campaign in the fall of
1528 2014, spatial gradients in aeolian sediment transport were measured. The gradients
1529 identified the intertidal beach as the primary source of aeolian sediment. In addition,
1530 local temporal deposition of sediment at the berm flat occurred. The deposition is
1531 likely caused by a combination of morphological feedback with the wind and an in-
1532 crease in bed roughness due to the presence of a shell pavement. The local deposition
1533 of sediment causes the transport of sediment from intertidal beach to dunes, dune
1534 lake and lagoon to be phased.

1535 From the measurements the following conclusions can be drawn:

- 1536 1. In the Sand Motor region, the (southern) intertidal beach area is a more impor-
1537 tant source of aeolian sediment than the dry beach area.
- 1538 2. The relative importance of the intertidal beach as supplier of aeolian sediment
1539 could be explained by the development of a beach armor layer in the dry beach
1540 area that outweighs the influence of high soil moisture contents in the intertidal
1541 beach area.
- 1542 3. Aeolian sediment originating from the intertidal beach seems to settle on the
1543 berm flat and to be gradually transported further resulting in an continuous
1544 sediment flux from the intertidal beach area and into the dunes, even if the
1545 intertidal beach is flooded.
- 1546 4. During high wind events, aeolian sediment availability in the intertidal beach
1547 area tends to be reduced by high water levels, while the sediment availability in
1548 the dry beach area tends to be increased due to mobilization of the beach armor
1549 layer;
- 1550 5. The construction height of a mega nourishment is important to its lifetime as it
1551 is governs compartmentalization of the beach due to beach armoring.

1552

Part II

1553

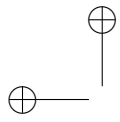
NUMERICAL MODELING

1554

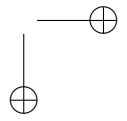
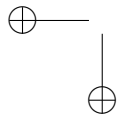
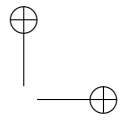
Inspired by the field observations a numerical model is developed and applied to hindcast the sub-aerial morphological evolution of the Sand Motor for the 4 years after construction.

1555

1556



"thesis" — 2016/12/13 — 10:12 — page 48 — #76



4

1557
1558

1559 NUMERICAL MODEL

1560 This chapter is based on a previous publication: Hoonhout, B. M. and de Vries, S. (2016d).
 1561 A process-based model for aeolian sediment transport and spatiotemporal varying sediment
 1562 availability. Journal of Geophysical Research: Earth Surface. doi:[10.1002/2015JF003692](https://doi.org/10.1002/2015JF003692).
 1563 2015JF003692.

1564 The numerical implementation of the model presented in this chapter and experimental features
 1565 not discussed are elaborated in Appendix B.

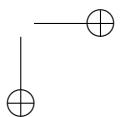
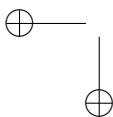
1566 4.1 INTRODUCTION

1567 Aeolian sediment transport is influenced by a variety of bed surface properties that
 1568 are commonly found in coastal environments, like: moisture, shells, strandlines, salt
 1569 crusts, bed slopes, vegetation, non-erodible elements and anthropogenic disturbances.
 1570 The bed surface properties influence aeolian sediment transport by changing the sed-
 1571 iment transport capacity and/or the sediment availability ([Kocurek and Lancaster,](#)
 1572 [1999](#)). In current aeolian sediment transport models the effects on the sediment trans-
 1573 port capacity and sediment availability are generally incorporated through a single
 1574 parameter: the velocity threshold. This approach appears to be a critical limitation
 1575 in existing aeolian sediment transport models for simulation of real-world cases with
 1576 spatiotemporal variations in bed surface properties.

1577 The velocity threshold was introduced by [Bagnold \(1935\)](#), and incorporated in his
 1578 initial aeolian sediment transport model ([Bagnold, 1937b](#)) according to:

$$\underbrace{q_{\text{sat}}}_{\substack{\text{sediment} \\ \text{transport} \\ \text{capacity}}} = \alpha C \underbrace{\frac{\rho_a}{g} \sqrt{\frac{d_n}{D_n}}}_{\substack{\text{properties} \\ \text{of sediment} \\ \text{in transport}}} (u_z - u_{\text{th}})^3 \quad (4.1)$$

1579 in which q_{sat} [kg/m/s] is the equilibrium or saturated sediment transport rate and
 1580 represents the sediment transport capacity. u_z [m/s] is the wind velocity at height z
 1581 [m] and u_{th} the velocity threshold [m/s]. The properties of the sediment in transport
 1582 are represented by a series of parameters: C [-] is a parameter to account for the
 1583 grain size distribution width, ρ_a [kg/m³] is the density of the air, g [m/s²] is the
 1584 gravitational constant, d_n [m] is the nominal grain size and D_n [m] is a reference grain
 1585 size. α is a constant to account for the conversion of the measured wind velocity to the
 1586 near-bed shear velocity following Prandtl-Von Kármán's Law of the Wall: $\left(\frac{\kappa}{\ln z/z'}\right)^3$



1587 in which z' [m] is the height at which the idealized velocity profile reaches zero and κ
 1588 [-] is the Von Kármán constant. Many studies following the work of [Bagnold \(1937b\)](#)
 1589 effectively proposed different parameterizations for sediment properties (e.g. [Owen,](#)
 1590 [1964; Hsu, 1971; Sørensen, 2004](#)) or changed the weight of the velocity threshold (e.g.
 1591 [Kawamura, 1951; Lettau and Lettau, 1978](#)). However, the characteristic structure and
 1592 application of these models stayed essentially the same.

1593 [Sherman et al. \(1998\)](#) and [Sherman and Li \(2012\)](#) summarized the performance of
 1594 eight aeolian sediment transport models compared to field measurements on a sandy
 1595 beach. All the models systematically overpredict the measured aeolian sediment trans-
 1596 port rates, which is in agreement with other coastal field studies (e.g. [Jackson and](#)
 1597 [Cooper, 1999; Lynch et al., 2008; Davidson-Arnott and Bauer, 2009; Aagaard, 2014](#)).
 1598 Besides, the original model of [Bagnold \(1937b\)](#) appeared to outperform the models of
 1599 later date. In an attempt to explain the poor performance of aeolian sediment trans-
 1600 port models in coastal environments, many authors emphasized the importance of
 1601 bed surface properties. Typical bed surface properties that are found along the coast
 1602 and assumed to explain at least partially the poor performance of aeolian sediment
 1603 transport models are high moisture contents (e.g. [Wiggs et al., 2004; Davidson-Arnott](#)
 1604 [et al., 2008; Darke and McKenna Neuman, 2008; McKenna Neuman and Sanderson,](#)
 1605 [2008; Udo et al., 2008; Bauer et al., 2009; Edwards and Namikas, 2009; Namikas et al.,](#)
 1606 [2010; Scheidt et al., 2010](#)), salt crusts (e.g. [Nickling and Ecclestone, 1981](#)), bed slopes
 1607 (e.g. [Iversen and Rasmussen, 2006](#)), vegetation (e.g. [Arens, 1996; Lancaster and Baas,](#)
 1608 [1998; Okin, 2008; Li et al., 2013; Dupont et al., 2014](#)), shell pavements (e.g. [van der](#)
 1609 [Wal, 1998; McKenna Neuman et al., 2012](#)) and sorted and armored beach surfaces (e.g.
 1610 [Gillette and Stockton, 1989; Gillies et al., 2006; Tan et al., 2013; Cheng et al., 2015](#)). The
 1611 influence of these bed surface properties on aeolian sediment transport has been inves-
 1612 tigated and often resulted in modified values for the velocity threshold (e.g. [Howard,](#)
 1613 [1977; Dyer, 1986; Belly, 1964; Johnson, 1965; Hotta et al., 1984; Nickling and Ecclestone,](#)
 1614 [1981; Arens, 1996; King et al., 2005](#)).

1615 A critical limitation of the use of the velocity threshold alone to cope with the
 1616 influence of bed surface properties is that it changes inherently in time and space
 1617 ([Stout, 2004](#)) and that it accounts for two fundamentally different phenomena:

- 1618 1. The change in the sediment transport capacity which represents the ease of
 1619 sediment transport *over* a given bed; and
- 1620 2. The change in sediment availability, which represents the ease of sediment en-
 1621 trainment *from* a given bed.

1622 Although in uniform and constant situations, like often used in wind tunnel experi-
 1623 ments, the difference might be negligible, in real-world field conditions it is not. The
 1624 difference is most apparent when observing transport over a bed with spatial vari-
 1625 ations in bed surface properties. For example due to tidal motions in the intertidal
 1626 beach area, emergence of roughness elements in the dry beach area and vegetation in
 1627 the dune area. In addition, temporal variations in bed surface properties, for example
 1628 due to tidal spring/neap cycles, rain showers, storm surges, seasonal variations in
 1629 vegetation and progressive armoring of the beach, increase the need for simulation
 1630 rather than parameterization of bed surface properties and sediment availability (as
 1631 discussed in section [4.2](#)).

1632 This paper presents a new model approach for aeolian sediment transport. The
 1633 model simulates rather than parameterizes bed surface properties and sediment avail-
 1634 ability. The model explicitly defines sediment availability following [de Vries et al.](#)
 1635 ([2014b](#)) and introduces multi-fraction aeolian sediment transport in order to simulate
 1636 processes that limit the availability of sediment, like beach armoring, and processes
 1637 that enhance the availability of sediment, like hydraulic mixing. Consequently, the
 1638 model can cope with arbitrary spatiotemporal configurations of bed surface proper-
 1639 ties. Although validation of the model is ongoing, the performance of the model
 1640 is illustrated using four prototype cases, the simulation of two wind tunnel experi-
 1641 ments from literature ([Nickling and McKenna Neuman, 1995](#); [Dong et al., 2004b](#)) and
 1642 a sensitivity analysis of newly introduced parameters.

1643 In literature the *velocity threshold* is used interchangeably to describe the (change
 1644 in) sediment transport capacity and sediment availability. In this paper the term *ve-
 1645 locity threshold* is strictly used to describe the (change in) sediment transport capacity
 1646 (Equation 4.1). The term *sediment availability* is used in accordance with the terminol-
 1647 ogy proposed by [Kocurek and Lancaster \(1999\)](#), which is often referred to as *sediment*
 1648 *supply* in literature.

1649 4.2 MODEL CHALLENGES: BED SURFACE PROPERTIES

1650 The importance of spatiotemporal variations in bed surface properties for aeolian
 1651 sediment transport is most apparent when observing transport over a bed consist-
 1652 ing of both erodible and non-erodible fractions. Many studies have investigated the
 1653 influence of varying grain sizes on aeolian sediment transport. In most cases it in-
 1654 volved studies on the influence of non-erodible or roughness elements using either
 1655 field experiments (e.g. [Davidson-Arnott et al., 1997](#); [Gillies et al., 2006](#); [Tan et al.,](#)
 1656 [2013](#)) or wind tunnel experiments (e.g. [Gillette and Stockton, 1989](#); [Nickling and](#)
 1657 [McKenna Neuman, 1995](#); [McKenna Neuman and Nickling, 1995](#); [Dong et al., 2004b](#);
 1658 [McKenna Neuman et al., 2012](#)) and occasionally numerical modeling (e.g. [Turpin et al.,](#)
 1659 [2010](#)). The studies typically use granular material with a clear bi-modal distribution.
 1660 A flat sandy surface is then partially covered by a significantly larger grain size frac-
 1661 tion ranging from shells and gravel to pebbles and cobbles. Typically the coverage
 1662 of non-erodible elements is expressed using the roughness density λ as described by
 1663 [Raupach et al. \(1993\)](#). [Raupach et al. \(1993\)](#) uses the roughness density to determine
 1664 the relative increase in the shear velocity threshold according to:

$$R_t = \frac{u_{*th,S}}{u_{*th,R}} = \frac{1}{\sqrt{(1 - m\sigma\lambda)(1 + m\beta\lambda)}} \quad (4.2)$$

1665 in which $u_{*th,S}$ is the shear velocity threshold with a bare surface, $u_{*th,R}$ is the shear
 1666 velocity threshold with a surface including non-erodible elements and m , σ and β
 1667 are calibration coefficients that account for the size and shape of the non-erodible
 1668 elements.

1669 4.2.1 *Temporal Variations in Bed Surface Properties*

1670 The concept of the roughness density is useful to describe the instantaneous influence
1671 of roughness elements in the bed on aeolian sediment transport. However, it does
1672 not account for the fact that roughness elements tend to emerge from the bed over
1673 time due to winnowing of fines. Following Gillette and Stockton (1989), Nickling
1674 and McKenna Neuman (1995) and McKenna Neuman and Nickling (1995) showed
1675 that the winnowing of fines and the emergence of roughness elements result in a
1676 time-dependent aeolian sediment transport rate. The time-dependency is caused by
1677 a recurrence relation between sediment transport and sediment availability. Conse-
1678 quently, neither the roughness density nor the sediment availability can be determined
1679 a-priori. We argue that process-based simulation of bed surface properties rather than
1680 parameterization is needed to solve the instantaneous sediment availability.

1681 McKenna Neuman et al. (2012) shows that even small shell fragments cause a sandy
1682 surface to be armored over time. But even in the absence of non-erodible roughness
1683 elements, spatiotemporal variations in bed surface properties may develop as the
1684 transport capacity is inversely related to the grain size (Bagnold, 1937b) resulting in
1685 sediment sorting: a coarsening of the bed surface and downwind deposition of fines
1686 (Bagnold, 1937b; van der Wal, 2000; Arens et al., 2002).

1687 4.2.2 *Spatial Variations in Bed Surface Properties*

1688 Spatial variations in bed surface properties occur naturally in coastal environments.
1689 For example, strandlines locally cover the erodible bed and reduce the sediment avail-
1690 ability. However, strandlines not necessarily reduce the sediment transport capacity
1691 to the same extent and may even increase the transport capacity due to fully elastic
1692 collisions with the sediment in transport. The distinction between sediment availabil-
1693 ity and sediment transport capacity in relation to bed surface properties is not offered
1694 by existing models.

1695 Dong et al. (2004b) describes a similar situation in a wind tunnel. In their exper-
1696 iment a patch of gravel (10 - 40 mm) is positioned downwind of a patch of sandy
1697 material. Dong et al. (2004b) show how the gravel patch reduces the aeolian sedi-
1698 ment transport rate downwind of the domain compared to the situation without the
1699 gravel. However, in all conditions sediment passes the patch, while sediment avail-
1700 ability from the patch is zero. There seems to be a tendency of an increase in sediment
1701 transport rate with increasing patch size when the patch size is relatively small. This
1702 is attributed to the change in transport characteristics due to fully elastic collisions
1703 between the sand grains and the gravel. Consequently, the saltation height and re-
1704 bound angle increase and in turn influence the sediment transport capacity. Only for
1705 large patch sizes the trapping of sand grains in the gravel pores becomes a dominant
1706 process resulting in a decrease in the sediment transport rate downwind of the gravel
1707 patch.

1708 Dong et al. (2004b) acknowledged the limitations of the use of the shear velocity
1709 threshold to describe the results of his wind tunnel experiments. Therefore they in-
1710 troduced a factor in the aeolian sediment transport formulation of Dymin (1954) that
1711 depends on the length of the gravel patch squared. Although an important obser-
1712 vation, the method is hardly generalizable to more realistic situations where moist

1713 intertidal beaches are located adjacent to strandlines and armored beaches that sub-
1714 sequently border a vegetated dune. Therefore, to cope with spatially varying bed
1715 surface properties an aeolian sediment transport model is needed that provides a
1716 generic distinction between the effect of bed surface properties on the sediment trans-
1717 port capacity and sediment availability.

1718 4.3 MODEL CONCEPTS: SEDIMENT AVAILABILITY, SATURATED TRANSPORT AND
1719 ENTRAINMENT

1720 The sediment transport capacity and sediment availability together determine the sed-
1721 iment entrainment. Sediment availability differs from entrainment in that the avail-
1722 ability defines the *potential* erosion of the bed, while the entrainment defines the *actual*
1723 erosion of the bed. If aeolian sediment transport is transport-limited, the sediment
1724 availability is larger than entrainment and not all available sediment will be trans-
1725 ported. Consequently, entrainment is governed by the sediment transport capacity. If
1726 aeolian sediment transport is availability-limited, entrainment is equal to the sediment
1727 availability. Whether aeolian sediment transport is transport- or availability-limited
1728 depends on the balance between the sediment transport capacity and the sediment
1729 availability that are both influenced by bed surface properties. In the literature vari-
1730 ous concepts to incorporate the influence of bed surface properties in aeolian sediment
1731 transport models can be found:

- 1732 1. the concept of the shear velocity threshold (e.g. Howard, 1977; Dyer, 1986; Belly,
1733 1964; Johnson, 1965; Hotta et al., 1984; Nickling and Ecclestone, 1981; Arens,
1734 1996);
- 1735 2. the concept of critical fetch (e.g. Bauer and Davidson-Arnott, 2002; Delgado-
1736 Fernandez, 2010);
- 1737 3. the concept of explicit availability (or supply; de Vries et al., 2014b).

1738 From these concepts the shear velocity threshold is typically applied in conjunction
1739 with a formulation for the aeolian sediment transport capacity (e.g. Equation 4.1).
1740 The sediment transport capacity described by these formulations is the equilibrium
1741 or saturated sediment transport rate. The saturated sediment transport rate is the
1742 maximum transport rate reached in case of a fetch (F) beyond the critical fetch (F_c ,
1743 Bauer and Davidson-Arnott, 2002). In case of abundant sediment availability and
1744 fetches beyond the critical fetch the saturated sediment transport rate seems to be
1745 an appropriate indicator for the actual sediment flux downwind of the observed do-
1746 main. However, in coastal environments fetches can be limited due to limited beach
1747 widths (e.g. Jackson and Cooper, 1999; Bauer et al., 2009; Davidson-Arnott et al., 2005;
1748 Delgado-Fernandez, 2010; Dong et al., 2004a) and sediment availability is limited due
1749 to beach armoring as well as other bed surface properties. Consequently, in reality
1750 the saturated sediment transport rate is not necessarily an appropriate indicator for
1751 the sediment flux downwind of the observed domain.

1752 The concept of critical fetch therefore introduces a measure to distinguish between
1753 saturated ($F \geq F_c$) and unsaturated sediment transport situations ($F < F_c$). In this
1754 approach the aeolian sediment transport rate, (critical) fetch distance, entrainment
1755 and sediment availability are related following:

$$q = \int_0^{\hat{F}} \phi(u_*, u_{*th}, m_a) dx \quad \text{with } \hat{F} = \min(F, F_c) \quad (4.3)$$

where q [kg/s/m] is the instantaneous sediment transport rate per unit width, F [m] is the fetch distance and F_c [m] the critical fetch distance, ϕ is the entrainment function that depends on the shear velocity u_* [m/s], the shear velocity threshold u_{*th} [m/s] and the available sediment mass m_a [kg/m²]. x [m] is the downwind distance from a zero-transport boundary. This integral is solved for by assuming a pre-defined entrainment rate. Equation 4.3 then simplifies to:

$$q = \Phi(u_*, u_{*th}, m_a, \hat{F}) \quad (4.4)$$

where Φ is the analytically integrated solution to Equation 4.3. Delgado-Fernandez and Davidson-Arnott (2011) use the critical fetch concept to incorporate the effect of spatiotemporal variations in soil moisture. However, due to the recurrence relation in time between the aeolian sediment transport rate q and the sediment availability m_a , neither the sediment availability nor the entrainment can be determined a-priori and the integral in Equation 4.3 cannot easily be solved analytically.

Equation 4.3 can be simplified by observing the difference between availability-limited and transport-limited situations. In availability-limited situations the entrainment function simplifies to $\frac{\partial m_a}{\partial t}$, while in transport-limited situations the sediment availability is abundant. Equation 4.3 can therefore be rewritten as:

$$q = \begin{cases} \int_0^{\hat{F}} \frac{\partial m_a}{\partial t} dx & \text{if availability-limited} \\ \int_0^{\hat{F}} \phi(u_*, u_{*th}) dx & \text{if transport-limited} \end{cases} \quad (4.5)$$

The wind velocity can influence sediment availability indirectly through beach armoring. Given constant wind velocity, the development of a beach armor layer can turn a transport-limited situation into an availability-limited situation, which subsequently influences the instantaneous aeolian sediment transport rate. In an availability-limited situation, entrainment does not depend on the wind velocity since the wind velocity is sufficiently high to mobilize all available sediment.

The distinction between availability-limited and transport-limited situations in Equation 4.5 naturally reveals the fundamental difference between sediment availability and the sediment transport capacity and shows why these two phenomena cannot be represented by a single parameter like the shear velocity threshold. Moreover, Equation 4.5 provides an opportunity to model availability-limited and transport-limited situations separately as proposed by de Vries et al. (2014b), who uses a 1D advection formulation in combination with the concept of a spatiotemporal varying sediment availability m_a (or supply S_e according to the terminology of de Vries et al. (2014b)) to regulate the entrainment, transport and deposition of sediment by wind.

The disadvantage of the use of an explicit term for the sediment availability is that little is known about the quantitative relation between availability and the different availability-limiting bed surface properties. Moreover, also in the approach of de Vries et al. (2014b) sediment availability is not quantified by the model, but is input to the model. Due to the recurrence relation between the sediment transport rate and

1792 sediment availability the governing input parameter to this model is unknown and the
 1793 resulting instantaneous sediment transport rate cannot be computed. Therefore we
 1794 propose to extend the approach of [de Vries et al. \(2014b\)](#) with numerical simulation
 1795 of spatiotemporal varying bed surface properties and sediment availability.

1796 **4.4 MODEL DESCRIPTION**

1797 The model approach of [de Vries et al. \(2014b\)](#) is extended to compute the spatiotemporal
 1798 varying sediment availability through simulation of the process of beach armoring.
 1799 For this purpose the bed is discretized in horizontal grid cells and in vertical bed layers
 1800 (2DV). Moreover, the grain size distribution is discretized into fractions. This allows
 1801 the grain size distribution to vary both horizontally and vertically. A bed composition
 1802 module is used to compute the sediment availability for each sediment fraction in-
 1803 dividually. This model approach is a generalization of existing model concepts, like
 1804 the shear velocity threshold and critical fetch, and therefore compatible with these
 1805 existing concepts.

1806 **4.4.1 Advection Scheme**

1807 A 1D advection scheme is adopted in correspondence with [de Vries et al. \(2014b\)](#) in
 1808 which c [kg/m²] is the instantaneous sediment mass per unit area in transport:

$$\frac{\partial c}{\partial t} + u_z \frac{\partial c}{\partial x} = E - D \quad (4.6)$$

1809 t [s] denotes time and x [m] denotes the cross-shore distance from a zero-transport
 1810 boundary. E and D [kg/m²/s] represent the erosion and deposition terms and hence
 1811 combined represent the net entrainment of sediment. Note that Equation 4.6 differs
 1812 from Equation 9 in [de Vries et al. \(2014b\)](#) as they use the saltation height h [m] and the
 1813 sediment concentration C_c [kg/m³]. As h is not solved for, the presented model com-
 1814 putes the sediment mass per unit area $c = hC_c$ rather than the sediment concentration
 1815 C_c . For conciseness we still refer to c as the *sediment concentration*.

1816 The net entrainment is determined based on a balance between the equilibrium
 1817 or saturated sediment concentration c_{sat} [kg/m²] and the instantaneous sediment
 1818 transport concentration c and is maximized by the available sediment in the bed m_a
 1819 [kg/m²] according to:

$$E - D = \min \left(\frac{\partial m_a}{\partial t} ; \frac{c_{sat} - c}{T} \right) \quad (4.7)$$

1820 T [s] represents an adaptation time scale that is assumed to be equal for both erosion
 1821 and deposition. A time scale of 1 second is commonly used ([de Vries et al., 2014b](#)).

1822 The saturated sediment concentration c_{sat} is computed using an empirical sediment
 1823 transport formulation (e.g. Equation 4.1) where the transport rate q_{sat} is divided by
 1824 the wind velocity u_z to obtain a mass per unit area (per unit width):

$$c_{sat} = \max \left(0 ; \alpha C \frac{\rho_a}{g} \sqrt{\frac{d_n}{D_n}} \frac{(u_z - u_{th})^3}{u_z} \right) \quad (4.8)$$

in which C [–] is an empirical constant to account for the grain size distribution width, ρ_a [kg/m³] is the air density, g [m/s²] is the gravitational constant, d_n [m] is the nominal grain size, D_n [m] is a reference grain size, u_z [m/s] is the wind velocity at height z [m] and α [–] is a constant to convert from measured wind velocity to shear velocity.

Note that at this stage the spatial variations in wind velocity are not solved for and hence no morphological feedback is included in the simulation. The model is initially intended to provide accurate sediment fluxes from the beach to the dunes rather than to simulate subsequent dune formation.

4.4.2 Multi-fraction Erosion and Deposition

The formulation for the equilibrium or saturated sediment concentration c_{sat} (Equation 4.8) is capable of dealing with variations in grain size through the variables u_{th} , d_n and C (Bagnold, 1937b). However, the transport formulation only describes the saturated sediment concentration assuming a fixed grain size distribution, but does not define how multiple fractions coexist in transport. If the saturated sediment concentration formulation would be applied to each fraction separately and summed up to a total transport, the total sediment transport would increase with the number of sediment fractions. Since this is unrealistic behavior the saturated sediment concentration c_{sat} for the different fractions should be weighted in order to obtain a realistic total sediment transport. Equation 4.7 therefore is modified to include a weighting factor \hat{w}_k in which k represents the sediment fraction index:

$$E_k - D_k = \min \left(\frac{\partial m_{a,k}}{\partial t} ; \frac{\hat{w}_k \cdot c_{sat,k} - c_k}{T} \right) \quad (4.9)$$

It is common to use the grain size distribution in the bed as weighting factor for the saturated sediment concentration (e.g. Delft3D-FLOW Manual, 2014, section 11.6.4). Using the grain size distribution at the bed surface as a weighting factor assumes, in case of erosion, that all sediment at the bed surface is equally exposed to the wind.

Using the grain size distribution at the bed surface as weighting factor in case of deposition would lead to the behavior where deposition becomes dependent on the bed composition. Alternatively, in case of deposition, the saturated sediment concentration can be weighted based on the grain size distribution in the air. Due to the nature of saltation, in which continuous interaction with the bed forms the saltation cascade, both the grain size distribution in the bed and in the air are likely to contribute to the interaction between sediment fractions. The ratio between both contributions in the model is determined by a bed interaction parameter ζ .

The weighting of erosion and deposition of individual fractions is computed according to:

$$\hat{w}_k = \frac{w_k}{\sum_{k=1}^{n_k} w_k} \quad (4.10a)$$

$$\text{where } w_k = (1 - \zeta) \cdot w_k^{\text{air}} + (1 - \hat{S}_k) \cdot w_k^{\text{bed}} \quad (4.10b)$$

in which k represents the sediment fraction index, n_k the total number of sediment fractions, w_k is the unnormalized weighting factor for fraction k , \hat{w}_k is its normalized

1862 counterpart, w_k^{air} and w_k^{bed} are the weighting factors based on the grain size distribution
 1863 in the air and bed respectively and \hat{S}_k is the effective sediment saturation of the
 1864 air. The weighting factors based on the grain size distribution in the air and the bed
 1865 are computed using mass ratios:

$$w_k^{\text{air}} = \frac{c_k}{c_{\text{sat},k}} ; w_k^{\text{bed}} = \frac{m_{a,k}}{\sum_{k=1}^{n_k} m_{a,k}} \quad (4.11)$$

1866 The sum of the ratio w_k^{air} over the fractions denotes the degree of saturation of the
 1867 air column for fraction k . The degree of saturation determines if erosion of a fraction
 1868 may occur. Also in saturated situations erosion of a sediment fraction can occur due
 1869 to an exchange of momentum between sediment fractions, which is represented by
 1870 the bed interaction parameter ζ . The effective degree of saturation is therefore also
 1871 influenced by the bed interaction parameter and defined as:

$$\hat{S}_k = \min \left(1 ; (1 - \zeta) \cdot \sum_{k=1}^{n_k} w_k^{\text{air}} \right) \quad (4.12)$$

1872 When the effective saturation is greater than or equal to unity the air is
 1873 (over)saturated and no erosion will occur. The grain size distribution in the bed is
 1874 consequently less relevant and the second term in Equation 4.10b is thus minimized
 1875 and zero in case $\zeta = 0$. In case the effective saturation is less than unity erosion may
 1876 occur and the grain size distribution of the bed also contributes to the weighting over
 1877 the sediment fractions. The weighting factors for erosion are then composed from
 1878 both the grain size distribution in the air and the grain size distribution at the bed
 1879 surface. Finally, the resulting weighting factors are normalized to sum to unity over
 1880 all fractions (\hat{w}_k).

1881 The composition of weighting factors for erosion is based on the saturation of the
 1882 air column. The non-saturated fraction determines the potential erosion of the bed.
 1883 Therefore the non-saturated fraction can be used to scale the grain size distribution
 1884 in the bed in order to combine it with the grain size distribution in the air according
 1885 to Equation 4.10b. The non-saturated fraction of the air column that can be used for
 1886 scaling is therefore $1 - \hat{S}_k$.

1887 For example, if bed interaction is disabled ($\zeta = 0$) and the air is 70% saturated,
 1888 then the grain size distribution in the air contributes 70% to the weighting factors
 1889 for erosion, while the grain size distribution in the bed contributes the other 30%
 1890 (Figure 4.1, upper left panel). In case of (over)saturation the grain size distribution
 1891 in transport contributes 100% to the weighting factors and the grain size distribution
 1892 in the bed is of no influence. Transport progresses in downwind direction without
 1893 interaction with the bed.

1894 To allow for bed interaction in saturated situations in which no net erosion can
 1895 occur, the bed interaction parameter ζ is used (Figure 4.1). The bed interaction pa-
 1896 rameter can take values between 0.0 and 1.0 in which the weighting factors for the
 1897 equilibrium or saturated sediment concentration in an (over)saturated situation are
 1898 fully determined by the grain size distribution in the bed or in the air respectively.
 1899 A bed interaction value of 0.2 represents the situation in which the grain size distri-
 1900 bution at the bed surface contributes 20% to the weighting of the saturated sediment
 1901 concentration over the fractions. In the example situation where the air is 70% sat-
 1902 urated such value for the bed interaction parameter would lead to weighting factors

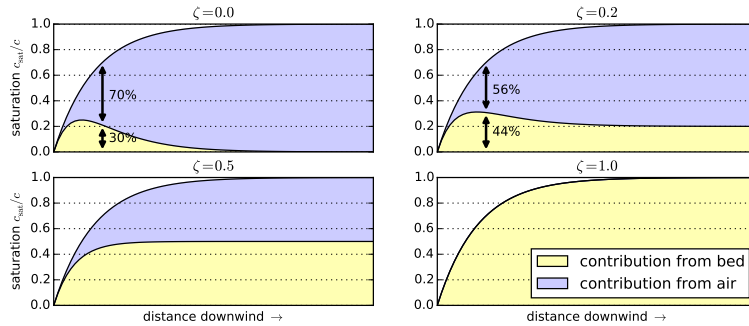


Figure 4.1: Contributions of the grain size distribution in the bed and in the air to the weighting factors \hat{w}_k for the equilibrium sediment concentration in Equation 4.9 for different values of the bed interaction parameter.

1903 that are constituted for $70\% \cdot (100\% - 20\%) = 56\%$ based on the grain size distribution
 1904 in the air and for the other 44% based on the grain size distribution at the bed surface
 1905 (Figure 4.1, upper right panel).

1906 The parameterization of the exchange of momentum between sediment fractions
 1907 is an aspect of saltation that is still poorly understood. Therefore calibration of the
 1908 bed interaction parameter ζ is necessary. The model parameters in Equation 4.8 can
 1909 be chosen in accordance with the assumptions underlying multi-fraction sediment
 1910 transport. C should be set to 1.5 as each individual sediment fraction is well-sorted, d_n
 1911 should be chosen equal to D_n as the grain size dependency is implemented through
 1912 u_{th} . u_{th} typically varies between 1 and 6 m/s for sand.

1913 4.4.3 Simulation of Sediment Sorting and Beach Armoring

1914 Since the equilibrium or saturated sediment concentration $c_{sat,k}$ is weighted over mul-
 1915 tiple sediment fractions in the extended advection model, also the instantaneous sed-
 1916 iment concentration c_k is computed for each sediment fraction individually. Conse-
 1917 quently, grain size distributions may vary over the model domain and in time. These
 1918 variations are thereby not limited to the horizontal, but may also vary over the verti-
 1919 cal since fine sediment may be deposited on top of coarse sediment or, reversely, fines
 1920 may be eroded from the bed surface leaving coarse sediment to reside on top of the
 1921 original mixed sediment. In order to allow the model to simulate the processes of
 1922 sediment sorting and beach armoring the bed is discretized in horizontal grid cells
 1923 and vertical bed layers (2DV; Figure 4.2).

1924 The discretization of the bed consists of a minimum of three vertical bed layers with
 1925 a constant thickness and an unlimited number of horizontal grid cells. The top layer
 1926 is the *bed surface layer* and is the only layer that interacts with the wind and hence
 1927 determines the spatiotemporal varying sediment availability and the contribution of
 1928 the grain size distribution in the bed to the weighting of the saturated sediment con-
 1929 centration. One or more *bed composition layers* are located underneath the bed surface

layer and form the upper part of the erodible bed. The bottom layer is the *base layer* and contains an infinite amount of erodible sediment according to the initial grain size distribution. The base layer cannot be eroded, but can supply sediment to the other layers.

Each layer in each grid cell describes a grain size distribution over a predefined number of sediment fractions (Figure 4.2, detail). Sediment may enter or leave a grid cell only through the bed surface layer. Since the velocity threshold depends among others on the grain size, erosion from the bed surface layer will not be uniform over all sediment fractions, but will tend to erode fines more easily than coarse sediment (Figure 4.2, detail, upper left panel). If sediment is eroded from the bed surface layer, the layer is repleted by sediment from the lower bed composition layers. The repleted sediment has a different grain size distribution than the sediment eroded from the bed surface layer. If more fines are removed from the bed surface layer in a grid cell than repleted, the median grain size increases. If erosion of fines continues the bed surface layer becomes increasingly coarse. Deposition of fines or erosion of coarse material may resume the erosion of fines from the bed.

In case of deposition the process is similar. Sediment is deposited in the bed surface layer that then passes its excess sediment to the lower bed layers (Figure 4.2, detail, upper right panel). If more fines are deposited than passed to the lower bed layers the bed surface layer becomes increasingly fine.

1950 4.4.4 Simulation of the Emergence of Non-erodible Roughness Elements

1951 Sediment sorting may lead to the emergence of non-erodible elements from the bed.
 1952 Non-erodible roughness elements may shelter the erodible bed from wind erosion
 1953 due to shear partitioning, resulting in a reduced sediment availability (Raupach et al.,
 1954 1993). Therefore Equation 4.2 is implemented according to:

$$u_{*th,R} = u_{*th} \cdot \sqrt{\left(1 - m \cdot \sum_{k=k_0}^{n_k} w_k^{\text{bed}}\right) \left(1 + \frac{m\beta}{\sigma} \cdot \sum_{k=k_0}^{n_k} w_k^{\text{bed}}\right)} \quad (4.13)$$

1955 in which σ is the ratio between the frontal area and the basal area of the roughness
 1956 elements and β is the ratio between the drag coefficients of the roughness elements
 1957 and the bed without roughness elements. m is a factor to account for the difference
 1958 between the mean and maximum shear stress and is usually chosen 1.0 in wind tunnel
 1959 experiments and may be lowered to 0.5 for field applications. The roughness density
 1960 λ in the original equation of Raupach et al. (1993, Equation 4.2) is obtained from the
 1961 mass fraction in the bed surface layer w_k^{bed} (Equation 4.11) according to:

$$\lambda = \frac{\sum_{k=k_0}^{n_k} w_k^{\text{bed}}}{\sigma} \quad (4.14)$$

1962 in which k_0 is the index of the smallest non-erodible sediment fraction in current
 1963 conditions and n_k is the total number of sediment fractions. It is assumed that the
 1964 sediment fractions are ordered by increasing size. Whether a fraction is erodible
 1965 depends on the sediment transport capacity.

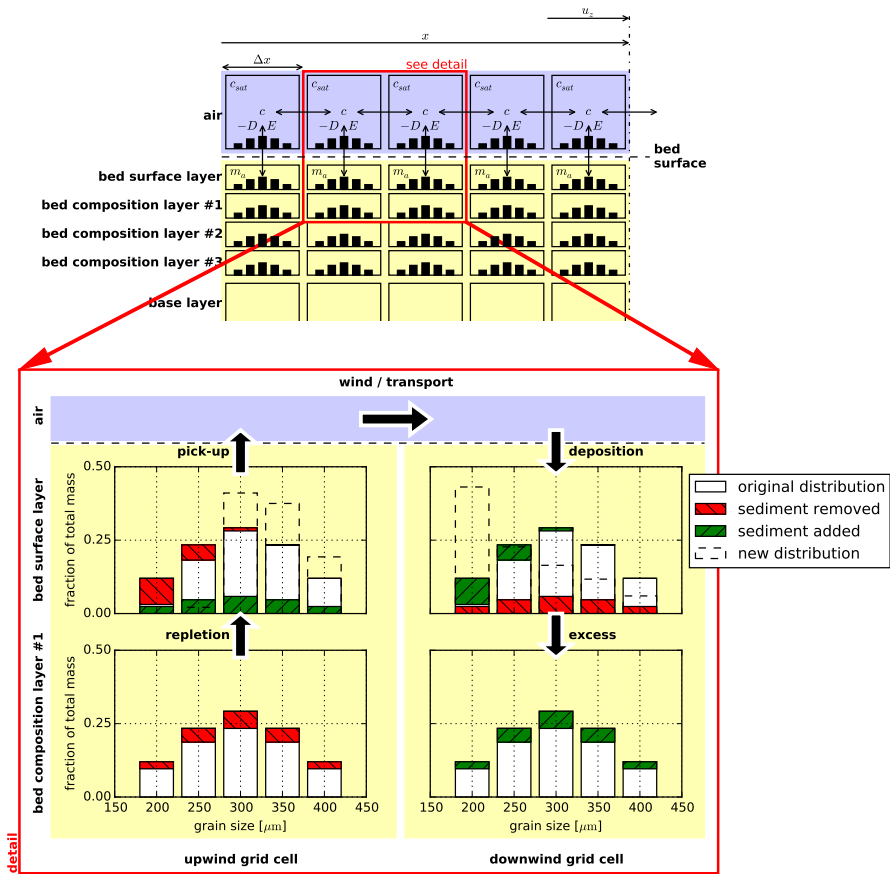


Figure 4.2: Schematic of bed composition discretisation and advection scheme. Horizontal exchange of sediment may occur solely through the air that interacts with the *bed surface layer*. The detail presents the simulation of sorting and beach armoring where the bed surface layer in the upwind grid cell becomes coarser due to non-uniform erosion over the sediment fractions, while the bed surface layer in the downwind grid cell becomes finer due to non-uniform deposition over the sediment fractions. Symbols refer to Equations 4.6 and 4.7.

1966 4.4.5 *Simulation of the Hydraulic Mixing, Infiltration and Evaporation*

1967 As sediment sorting due to aeolian processes can lead to armoring of a beach sur-
 1968 face, mixing of the beach surface or erosion of course material may undo the effects
 1969 of armoring. To ensure a proper balance between processes that limit and enhance
 1970 sediment availability in the model both types of processes need to be sufficiently repre-
 1971 sented when simulating spatiotemporal varying bed surface properties and sediment
 1972 availability.

1973 A typical upwind boundary in coastal environments during onshore winds is the
 1974 water line. For aeolian sediment transport the water line is a zero-transport bound-
 1975 ary. In the presence of tides, the intertidal beach is flooded periodically. Hydraulic
 1976 processes like wave breaking mix the bed surface layer of the intertidal beach, break
 1977 the beach armoring and thereby influence the availability of sediment. Moreover, the
 1978 hydraulic processes periodically wet the intertidal beach temporally increasing the
 1979 shear velocity threshold. Infiltration and evaporation subsequently dry the beach.

1980 In the model the mixing of sediment is simulated by averaging the sediment dis-
 1981 tribution over the depth of disturbance (Δz_d). The depth of disturbance is linearly
 1982 related to the breaker height (e.g. King, 1951; Williams, 1971; Masselink et al., 2007).
 1983 Masselink et al. (2007) proposes an empirical factor $f_{\Delta z_d}$ [-] that relates the depth of
 1984 disturbance directly to the local breaker height according to:

$$\Delta z_d = f_{\Delta z_d} \cdot \min(H ; \gamma \cdot d) \quad (4.15)$$

1985 in which the offshore wave height H [m] is taken as the local wave height maximized
 1986 by a maximum wave height over depth ratio γ [-]. d [m] is the water depth that is
 1987 provided to the model through an input time series of water levels. Typical values for
 1988 $f_{\Delta z_d}$ are 0.05 to 0.4 and 0.5 for γ .

1989 The drying of the beach is simulated by simplified functions for infiltration and
 1990 evaporation. Infiltration is represented by an exponential decay function that is gov-
 1991 erned by a drying time scale T_{dry} . Evaporation is simulated using an adapted version
 1992 of the Penman-Monteith equation (Shuttleworth, 1993) that is governed by meteoro-
 1993 logical time series of solar radiation, temperature and humidity.

1994 4.5 RESULTS

1995 The model is applied to a series of prototype cases to illustrate the processes de-
 1996 scribed by the model, two wind tunnel experiments to illustrate the capabilities of the
 1997 model to simulate spatiotemporal variations in bed surface properties and sediment
 1998 availability and a sensitivity analysis.

1999 4.5.1 *Prototype cases*

2000 The four prototype cases P1 to P4 are intended to illustrate the capabilities of the
 2001 presented model to simulate processes of sediment sorting (van der Wal, 2000; Arens
 2002 et al., 2002) and beach armoring (van der Wal, 1998). The prototype cases are con-
 2003 structed using a 120 m schematized linear beach with a 1:20 slope, a wind velocity
 2004 of 12 or 30 m/s, a drying time scale T_{dry} of 3 h, constant evaporation and a simula-

2005 tion time of 30 days. The prototype cases are initialized with lognormally distributed
 2006 sediment with $d_{50} = 335 \mu\text{m}$ (Φ – scale = 1.6, $\sigma_\Phi = 0.4$), which is representative
 2007 for nourished poorly sorted beaches along the Dutch coast. Parameterizations for
 2008 shells and shell fragments in Equation 4.13 are based on experiments described by
 2009 McKenna Neuman et al. (2012) and chosen as $m = 0.5$, $\sigma = 4.2$ and $\beta = 130$. The four
 2010 scenarios described by the prototype cases are:

- 2011 P1 This scenario is used as reference for normalization and involves sand only and no
 tidal movement. The model is forced by a constant wind of 12 m/s. Sediment
 sorting occurs due to the presence of a wide range of sediment fractions. How-
 ever, beach armoring does not occur due to the absence of shells, resulting in an
 almost constant sediment transport rate at the downwind end of the domain.
- 2016 P2 This scenario involves 5% of shells and shell fragments ranging from 2 to 30 mm
 and no tidal movement. The model is forced by a constant wind of 12 m/s. The
 presence of shells means that beach armoring occurs that causes spatiotemporal
 variations in sediment availability and a decrease in sediment transport.
- 2020 P3 This scenario involves 5% of shells and shell fragments and a sinusoidal tide with
 a 2 m tidal range and a tidal period of 12 h. The tide periodically floods a 40 m
 intertidal beach area. The model is forced by a constant wind of 12 m/s. The
 tidal movement causes mixing of the bed surface layer in the intertidal beach
 area reducing the effects of beach armoring.
- 2025 P4 This scenario is equal to scenario P3, but the model is forced by a wind of 12
 m/s that is increased twice to 30 m/s to simulate the effect of higher energy
 wind events that (partially) reset the composition of the bed surface layer and
 temporarily increase the sediment availability in the dry beach area.

2029 Figure 4.3 presents the simulated aeolian sediment transport rates at the downwind
 2030 end of the domain for cases P2 to P4 over the course of 30 days of simulation time.
 2031 The results are normalized using the transport rate in case P1. The reference case
 2032 P1 shows an almost constant transport rate over the entire course of the simulation.
 2033 The presence of shells in case P2 results in a reduction of sediment availability. As
 2034 a result, the transport rates in case P2 are lower compared to case P1. The transport
 2035 rate decreases as more shells emerge from the bed and a beach armor layer develops.
 2036 In case P2 there are no processes that break the armoring and the transport rates
 2037 asymptotically reach zero. The beach armor layer develops in direction of the wind.
 2038 Therefore, the relative contribution of the downwind part of the beach ($x \geq 40$) to the
 2039 total sediment transport increases over time.

2040 Case P3 includes tidal movement and hydraulic mixing. At the high water line the
 2041 sediment transport is zero during high tide and maximized during low tide. Initially,
 2042 transport is not saturated at the high water line and entrainment of sediment contin-
 2043 ues over the dry beach. As shells emerge from the bed, a beach armor layer develops
 2044 that reduces sediment availability. The reduction of sediment availability progresses
 2045 slower at the intertidal beach compared to the dry beach due to hydraulic mixing.
 2046 After 8 days the sediment transport rates at the high water line start to exceed the
 2047 sediment transport rates at the dune foot during low water. Sediment that is eroded
 2048 from the intertidal beach during low water is partially trapped at the dry beach due to

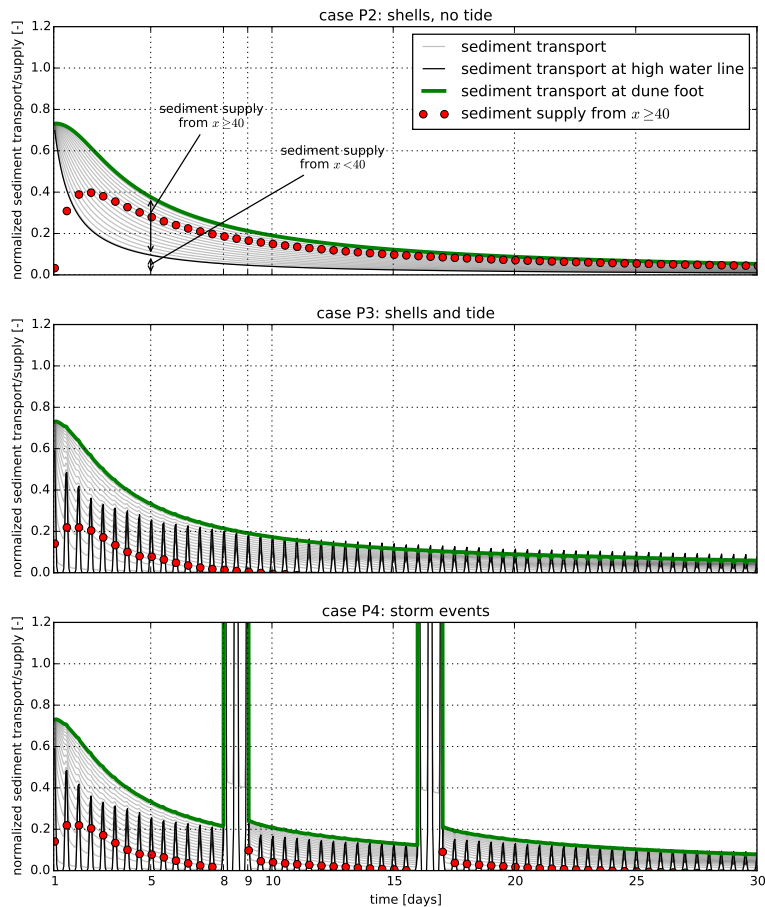


Figure 4.3: Sediment transport in time and over the model domain for three scenarios with constant wind. Each line depicts a different location along the beach, starting from $x = 40$ m, which coincides with the high water line in cases P₃ and P₄, and ends at the dune foot. Results are normalized using the transport rate in case P₁ with almost constant transport (not shown). The difference between the sediment transport at dune foot (green) and the sediment transport at $x = 40$ m is visualized by the red dots and represents the sediment supply from the dry beach. In cases P₃ and P₄ the sediment transport at the high water line periodically exceeds the sediment transport at the dune foot, indicating local deposition of sediments originating from the intertidal beach.

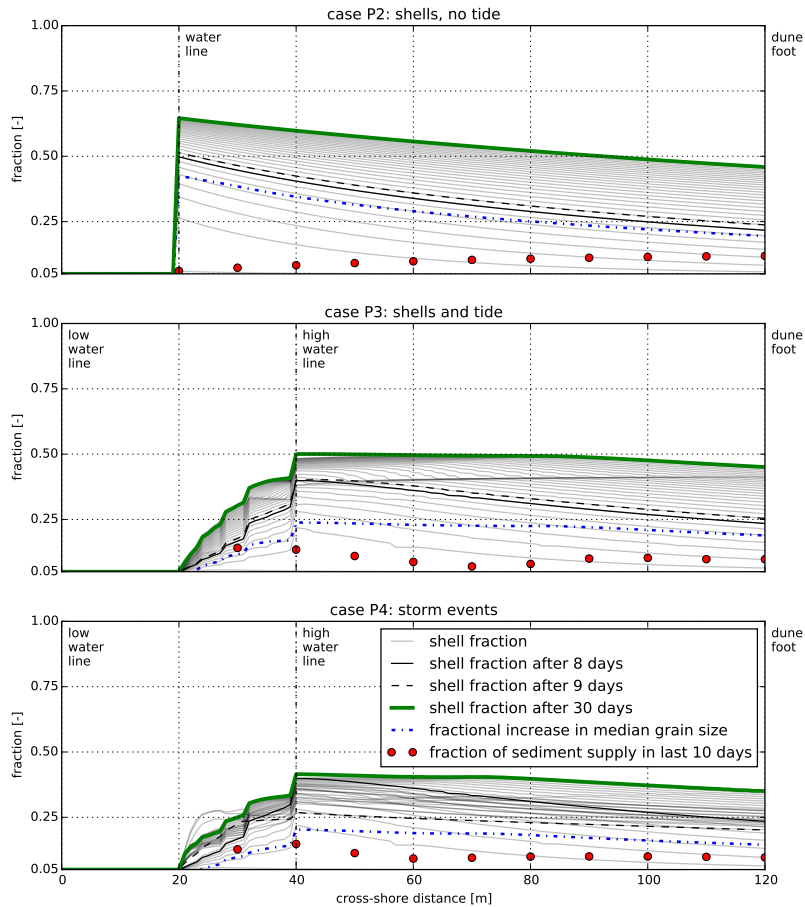


Figure 4.4: Distribution of the shell fraction over the model domain and in time. Sediment supply is inversely related to the degree of beach armoring, indicated by the shell fraction. Median grain size increases with the increase in shell fraction indicating erosion of predominantly fines. High-energy wind events in case P₄ even mobilize shell fractions resulting in a decrease in beach armoring and an increase in sediment availability.

2049 differences in roughness. During subsequent high water, when the sediment supply
 2050 from the intertidal beach ceases, these deposits are again entrained and blown down-
 2051 wind. The net erosion from the dry beach ultimately approaches zero as armoring
 2052 of the dry beach progresses. At this point all sediment deposited downwind origi-
 2053 nates directly from the intertidal beach. However, due to the spatial differences in
 2054 roughness, sediment is temporally deposited at the dry beach and cause the sediment
 2055 transport rates at the dune foot to be only weakly correlated with the tidal movement.

2056 Case P4 shows a pattern similar to case P3, but after 8 and 16 days a relatively high-
 2057 energy wind event passes for 24 hours. As a result, the transport rate spikes, but an
 2058 elevated transport rate is also visible after the wind velocity drops. During the high-
 2059 energy wind event even small shell fragments are mobilized. The beach armoring
 2060 is therefore (partially) removed and more sediment is available for transportation
 2061 afterwards. This leads to a prolonged peak in sediment transport and an increase of
 2062 the relative contribution of the dry beach to the total sediment transport at the dune
 2063 foot. After the beach armoring is re-established over time the transport rates approach
 2064 the rates of case P3 again.

2065 The differences in transport rate between the prototype cases are directly related
 2066 to sediment availability, since the wind is constant in all cases but case P4. Figure
 2067 4.4 shows the fractions of shells and shell fragments in the bed surface layer for case
 2068 P2 to P4. The shell fraction increases over time in all simulations. In case P2 the
 2069 shell fraction peaks at the water line as the beach armor layer develops in downwind
 2070 direction. Consequently, at the end of the simulation most sediment originates from
 2071 the downwind end of the beach where the beach armoring is least developed. In
 2072 case P3 and P4 hydraulic mixing causes the shell fraction in the intertidal beach to
 2073 remain low resulting in a different distribution of shells compared to case P2 and
 2074 hence a difference in sediment availability. Consequently, at the end of the simulation
 2075 most sediment originates from the intertidal beach. In reality, the contribution of the
 2076 intertidal beach to the total sediment transport is likely to be higher as more marine
 2077 processes counteract the local development of a beach armor layer than currently
 2078 simulated, like marine deposits and buoyancy of shells. In case P4 the drop in shell
 2079 fraction from day 8 to day 9 is related to the first high-energy wind event. At the end
 2080 of the simulation, the fraction of sediment that originates from the intertidal beach is
 2081 relatively low compared to case P3. In all cases also the median grain size in the bed
 2082 surface layer increases, indicating that predominantly fine sediment is eroded from
 2083 the bed. The unbalanced sediment transport over the fractions cause sediment sorting
 2084 in downwind direction.

2085 The contribution to the instantaneous sediment transport of the specific processes
 2086 described by the model can be distinguished in the prototype cases P1 to P4 because
 2087 a constant wind velocity is imposed. If a more realistic variable wind velocity time
 2088 series is used, the contributions of the specific processes are obscured by the wind-
 2089 related variance. To show that the simulation of spatiotemporal bed surface properties
 2090 and sediment are also important in variable wind conditions, prototype cases P1 to
 2091 P3 are repeated using an synthetic variable wind time series (P1b to P3b). The time
 2092 series is generated using a Markov Chain Monte Carlo (MCMC) simulation following
 2093 a Weibull distribution with a mean wind velocity of 12 m/s.

2094 Figure 4.5 shows the sediment transport rate in case P3b normalized by the sedi-
 2095 ment transport rate in case P1b depending on the hourly averaged wind velocity. To

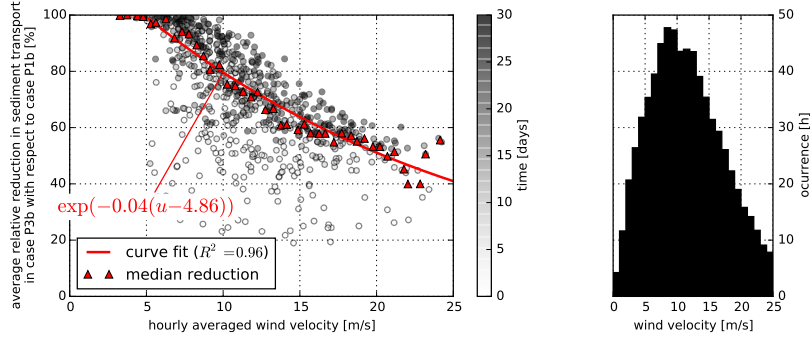


Figure 4.5: Average reduction in sediment transport in prototype case P3b compared to case P1b depending on the hourly averaged wind velocity (left panel). The results are obtained using a synthetic variable wind time series following a Weibull distribution with a mean wind velocity of 12 m/s (right panel). The sediment transport reduction (scatter) is binned according to the wind velocity using 0.5 m/s bins. The median reduction per bin (triangles) is used to fit an exponential curve (line). The reduction tends to increase during the simulation (scatter colors).

remove the influence of the wind variability, the normalized sediment transport time series obtained from the simulations are binned according to the hourly averaged wind velocity in 0.5 m/s bins. The median transport rate in each bin is subsequently determined to obtain a relation between instantaneous normalized sediment transport and wind velocity. The reduction is close to 100% up to wind velocities of 5 m/s and subsequently decreases according to an exponential function. The median reduction for 12 m/s wind velocity is 74%, which is less than the maximum reduction of 95.0% with a constant 12 m/s wind velocity in case P3. The reduction tends to increase during the simulation as beach armoring progresses.

4.5.2 Wind tunnel experiments

To illustrate the applicability of the model approach, two unrelated wind tunnel experiments obtained from literature are simulated that involve either temporal ([Nickling and McKenna Neuman, 1995](#)) or spatial ([Dong et al., 2004b](#)) variations in bed surface properties as discussed in section 4.2.

[Nickling and McKenna Neuman \(1995\)](#) describe an experiment in a wind tunnel with a 4.5 m working section in which a grid of 18 mm marbles was buried in sandy material with $d_{50} = 270 \mu\text{m}$. During the experiment with constant wind of 8 m/s, measured at 25 cm above the bed, the sand is winnowed from in between the marbles resulting in the emergence of the marbles over time. The emergence of the marbles cause the bed to become armored. The effect of armoring of a marble extends beyond the marble dimensions due to shadowing effects in the lee of the marble described by Equation 4.13. All parameter values, including z' , are obtained from [Nickling and](#)

2118 McKenna Neuman (1995) and hence no further calibration of parameters is performed
 2119 for this simulation.

2120 Figure 4.6 shows the modeled normalized sediment transport rate in comparison
 2121 with the measurements described in Nickling and McKenna Neuman (1995). Where
 2122 the measurements start with a relatively constant transport and even a slight increase
 2123 in transport, the model predicts an immediate decrease in transport. The marbles
 2124 are modeled as a large sediment fraction for which its presence in a bed composition
 2125 layer is described by a mass fraction rather than a location. Therefore, it is possible
 2126 to define the marble density, but not the exact marble locations. Consequently, from
 2127 the start of the simulation marbles start to emerge from the bed resulting in an im-
 2128 mediate decrease in sediment transport. In contrast, in the wind tunnel the marbles
 2129 are covered with a thin layer of sand that was removed first before the marbles start
 2130 to emerge. The initial emergence of the marbles coincided with a slight increase in
 2131 sediment transport. Nickling and McKenna Neuman (1995) attributes this rise to a
 2132 pronounced change in boundary conditions and turbulence. Since these small scale
 2133 variations in the wind shear are not represented in the model the rise in transport
 2134 is not visible in the model results. However, the decrease in sediment transport due
 2135 to the emergence of the marbles for the three different grid spacings described in
 2136 Nickling and McKenna Neuman (1995), is qualitatively represented by the model.

2137 Dong et al. (2004b) describe an experiment in a wind tunnel with a 21 m working
 2138 section in which a patch of gravel with diameter 10 – 40 mm was positioned down-
 2139 wind of a sandy bed with $d_{50} = 180 \mu\text{m}$. The length of the gravel patch was varied
 2140 between the experiments from 0.5 – 12 m and the wind velocity from 8 – 22 m/s,
 2141 measured at 60 cm above the bed. The free-flow wind velocities are converted to
 2142 shear velocities assuming $z' = 6 \text{ mm}$. The gravel patch traps saltating grains. In the
 2143 model the entrapment of grains is simulated as an exchange of momentum between
 2144 the sandy fractions and the immobile gravel fraction. This exchange is governed by
 2145 the bed interaction parameter, which is calibrated for this simulation and found to be
 2146 0.05.

2147 Figure 4.7 shows the modeled sediment transport rate in comparison with the mea-
 2148 surements described in Dong et al. (2004b). The increase in sediment transport with
 2149 increasing wind velocity is well represented by the model given the uniform RMSE
 2150 among the different wind velocities. The decrease in sediment transport rate with in-
 2151 creasing gravel patch length is represented by the model with a relative RMSE of less
 2152 than 10% for all except the lowest and highest wind velocities. Significant surpassing
 2153 of sediment over the sediment trap during the measurements with 22 m/s wind veloc-
 2154 ity is reported by Dong et al. (2004b), which explains the consistent overprediction of
 2155 the sediment fluxes by the model. The discrepancy between the model and the mea-
 2156 surements for the 8 and 10 m/s wind velocities is less consistent and is expected to
 2157 be a result of a low signal-to-noise ratio related to the small sediment fluxes. Also for
 2158 short gravel patch lengths the model deviates from the measurements. The relatively
 2159 high variability over the 0.5 to 2 m gravel patch lengths is attributed to a change in
 2160 transport characteristics (Dong et al., 2004b) due to fully elastic collisions between the
 2161 sand grains and the gravel. A bed interaction parameter that is not constant is needed
 2162 to capture this behavior in the model.

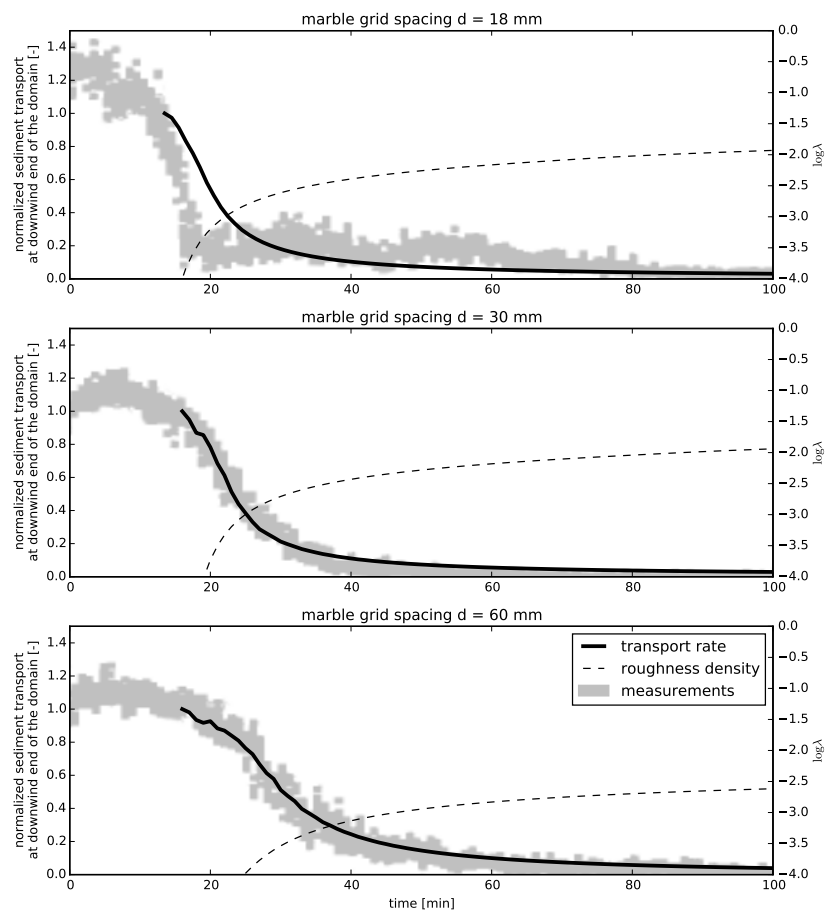


Figure 4.6: Comparison between modeled and measured normalized sediment transport rates from wind tunnel experiments described in [Nickling and McKenna Neuman \(1995\)](#). The dashed line depicts the emergence of marbles in terms of increasing roughness density. The visualization of the measurement results is copied from Figure 4 in the original publication without digitization.

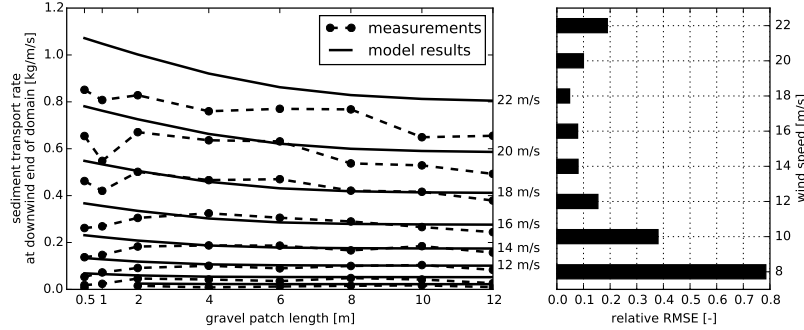


Figure 4.7: Comparison between model results and measurements from wind tunnel experiments described in Dong et al. (2004b) (left panel) and RMS errors relative to the mean measured transport rate (right panel). The measured transport rates with a wind velocity of 22 m/s are underestimated due to surpassing of sediment over the sediment trap (Dong et al., 2004b).

2163 4.5.3 Sensitivity

2164 The sensitivity of the model to four newly introduced parameters and the wind velocity
 2165 is determined to obtain insight in the importance of these parameters to the model
 2166 results. The newly introduced parameters are the bed interaction parameter, depth of
 2167 disturbance factor, the drying time scale and the grain size distribution standard devi-
 2168 ation. Case P3 as presented in section 4.5.1 is used as starting point for the sensitivity
 2169 analysis. Figure 4.8 shows the change in normalized total sediment transport given
 2170 variations of each of the four model parameters and the wind velocity.

2171 The bed interaction parameter, the depth of disturbance factor and the drying time
 2172 scale affect the source area of aeolian sediment (Figure 4.8a, b and c). In absence
 2173 of bed interaction all sediment entrained in the intertidal beach area is being trans-
 2174 ported to the downwind end of the domain unhindered. In contrast, in the presence
 2175 of bed interaction sediment from the intertidal beach area may be trapped in the beach
 2176 armor layer that is being developed in the dry beach area during the simulation. Con-
 2177 sequently, the total sediment transport reduces with increasing bed interaction. The
 2178 bed interaction parameter parameterizes the exchange between sediment fractions,
 2179 which is an aspect of saltation that is still poorly understood. In particular situations
 2180 with a large spatial variability in bed surface properties the bed interaction parameter
 2181 is expected to show a more significant sensitivity (e.g. Dong et al., 2004b). Therefore
 2182 calibration of the bed interaction parameter is necessary in such situations.

2183 The depth of disturbance factor shows no significant sensitivity as aeolian sediment
 2184 supply from the intertidal beach is concentrated close to the water line where wave
 2185 heights are negligible. Lower parts of the intertidal beach are continuously too moist
 2186 for sediment to be entrained. The sensitivity to the depth of disturbance factor in-
 2187 creases with decreasing drying time scale, but typically only for values smaller than
 2188 0.5 m. The sensitivity to the drying time scale shows that for time scales larger than
 2189 several hours the intertidal beach is continuously too moist for sediment to be en-

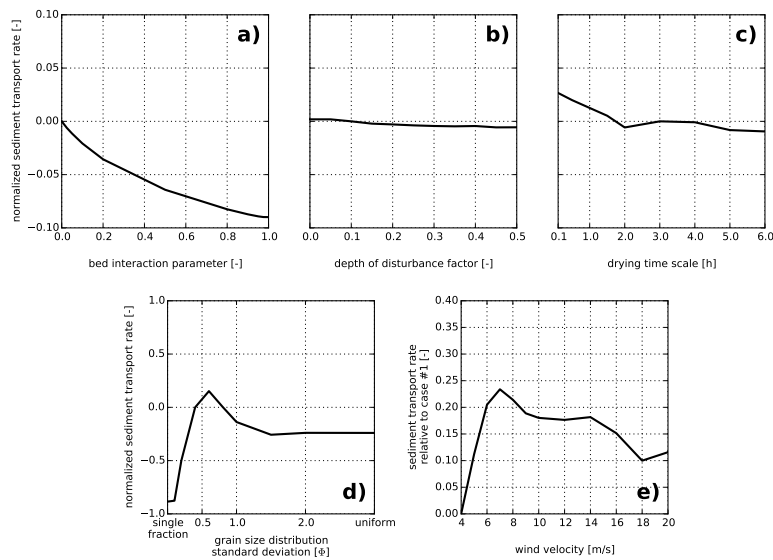


Figure 4.8: Sensitivity of the total normalized sediment transport with respect to case P₃ for four newly introduced parameters and the wind velocity. The sensitivity of the wind velocity is expressed with respect to the transport rate in case P₁.

2190 trained. For small drying time scales the intertidal beach supplies aeolian sediment
 2191 that contains relatively many fines, resulting in a slight increase in total sediment
 2192 transport.

2193 From the sensitivity of the grain size distribution width, represented by the grain
 2194 size distribution standard deviation and strictly speaking not a model parameter, it
 2195 can be concluded that the introduction of multiple sediment fractions has a signifi-
 2196 cant impact on the sediment transport rate (Figure 4.8d). However, for poorly sorted
 2197 sediments the sensitivity of the model to the distribution width is limited. Beyond a
 2198 standard deviation of $\sigma_\Phi = 1.5$ the development of the sediment rate is similar to the
 2199 transport rate with a uniform distribution.

2200 The rate of armoring depends on the presence of non-erodible sediment fractions.
 2201 Whether a sediment fraction is erodible depends on the wind transport capacity.
 2202 Therefore the rate of armoring and consequently the instantaneous sediment avail-
 2203 ability depends on the wind velocity. Figure 4.8e depicts the sediment transport rate
 2204 in case P3 with respect to the almost constant transport rate in case P1 for different
 2205 wind velocities. For low wind velocities all shell fractions can contribute to the es-
 2206 tablishment of a beach armor layer, but the beach armor layer develops slowly as
 2207 the winnowing of fines is dependent on the entrainment rate. For high wind veloc-
 2208 ities even shell fragments may be mobilized, but the beach armor layer consisting of
 2209 larger shells is developed quickly. Consequently, the reduction of sediment transport
 2210 is present over all wind velocities and 83% on average.

2211 4.6 DISCUSSION

2212 Process-based simulation of bed surface properties and sediment supply provides
 2213 an alternative for complex spatiotemporal parameterizations. Nevertheless, process-
 2214 based simulation itself requires parameterization, calibration and validation. These
 2215 parameterizations are generally less complex as they describe static properties rather
 2216 than spatiotemporal varying processes.

2217 4.6.1 Parameterization

2218 Compared to existing models for availability-limited aeolian sediment transport the
 2219 need for complex parameterization has been reduced in the presented model. The
 2220 adoption of the advection model of [de Vries et al. \(2014b\)](#) makes parameterization of
 2221 spatiotemporal variations in the shear velocity threshold, like attempted by [Nickling](#)
 2222 and [McKenna Neuman \(1995\)](#), [Dong et al. \(2004b\)](#) and others, unnecessary. In addi-
 2223 tion, process-based simulation of bed surface properties makes parameterization of
 2224 the inherently time-varying sediment availability m_a unnecessary. Existing param-
 2225 terizations for the shear velocity threshold under influence of moisture, vegetation,
 2226 sediment sorting and other bed surface properties are still valid for the instantaneous
 2227 shear velocity threshold.

2228 Despite the efforts to minimize complex parameterizations that are difficult to gen-
 2229 eralize, the model also introduces new parameterizations that are specifically related
 2230 to the process-based simulation of sediment availability, i.e. the bed interaction pa-
 2231 rameter, depth of disturbance and soil drying time scale. The depth of disturbance
 2232 and soil drying time scale could easily be replaced by process-based simulation as

2233 there is thorough knowledge on near-shore morphodynamics and beach hydrology.
2234 Moreover, the presented model framework allows for spatiotemporal variations of pa-
2235 rameters that are known not to be constant (e.g. z'). However, these considerations
2236 are outside the scope of this paper and will be part of future research.

2237 *4.6.2 Calibration*

2238 The calibration of the parameters involved in process-based simulation of sediment
2239 availability is a relatively new field of research. In this paper a pragmatic approach
2240 to calibration of these parameters is adopted, but there are various opportunities for
2241 improvement. For example, the depth of disturbance is used to approximate the
2242 mixing of the intertidal beach surface by waves. [Masselink et al. \(2007\)](#) shows how
2243 the depth of disturbance can be determined based on a linear relation with the local
2244 wave height. The mixing of the intertidal beach surface is particularly important as it
2245 breaks beach armoring. The depth of disturbance does not provide any information
2246 about how the bed is disturbed, just over which depth. Moreover, aspects like ma-
2247 rine deposits and shell buoyancy also affect the sediment availability in the intertidal
2248 beach area. [Gallagher et al. \(2011\)](#) presented detailed measurements of spatiotemporal
2249 variations in the bed surface grain size at Truc Vert, France. The intertidal beach ap-
2250 pears to be consistently finer than the upper beach. The measurements are obtained
2251 using macrophotography ([Buscombe et al., 2010](#)) ensuring that the measurements
2252 solely involve the beach surface. These type of measurements may provide a much
2253 more detailed calibration of the hydraulic mixing simulated in the model, although it
2254 might be questioned if such detailed hydraulic calibration is still within the scope of
2255 an aeolian sediment transport model. Alternatively, the calibration of the hydraulic
2256 mixing could be left to dedicated near-shore models (e.g. XBeach; [Roelvink et al.,](#)
2257 [2009; Reniers et al., 2013](#)) and online model coupling could be used to incorporate
2258 detailed near-shore hydro- and morphodynamics in the proposed aeolian modeling
2259 framework.

2260 Similarly, an exponential decay function with a constant drying time scale is cur-
2261 rently used to approximate the influence of the hydrological process of infiltration.
2262 The exponential decay is a simplified approach that was adopted after it appeared to
2263 be a reasonable approximation of numerical model results obtained with the HYDRUS
2264 model ([Šimůnek et al., 1998](#)) that simulates the soil moisture contents in the unsatu-
2265 rated zone following [van Genuchten \(1978\)](#). Detailed measurements for calibration
2266 of the instantaneous soil moisture can be obtained relatively easy using either in-situ
2267 or remote infra-red or microwave measurements (e.g. [Edwards et al., 2013; Hoonhout](#)
2268 [et al., 2014a](#)). Again, it might be questioned if the amount of detail involved in using
2269 these kind of data for estimates of the bed surface moisture is still within the scope of
2270 an aeolian sediment transport model.

2271 In contrast to the depth of disturbance and the drying rate, the bed interaction
2272 parameter has little relation with existing literature. In essence, the bed interaction
2273 parameter describes the exchange of momentum between grain size fractions along
2274 the fetch distance. Specifically it describes whether impacting grains eject other grains
2275 from the bed or that they are rebounded due to fully elastic collisions with large, non-
2276 erodible elements. A low value for the bed interaction parameter would indicate a
2277 large number of rebounding grains, while a high value would indicate a low num-

ber of rebounding grains. Typically, the number of rebounded grains increases with an increasing number of non-erodible, large elements in the bed. Consequently, the bed interaction parameter is not uniform over the fractions. Moreover, due to beach armoring the bed interaction is neither constant over time nor in space. In this paper the bed interaction parameter is pragmatically assumed to be uniform and constant since no basis for differentiation of the parameter is currently available. Thorough calibration of the bed interaction parameter would require detailed, spatiotemporal measurements of grain size distributions in the bed and the saltation cascade. It would require a series of sediment traps along the fetch that are regularly emptied and sieved as to determine the change of the grain size distribution in the saltation cascade in space and over time. Concurrently the grain size distribution at the bed surface over the entire fetch needs to be monitored without disturbing the bed significantly. In a laboratory environment the change in grain size distribution could be monitored using sediment that is colored per fraction. Visual observation of the change in coloring then provides insight in the change in grain size distribution. However, the experiment should be performed at such scale that the trapping of sediment by upwind traps does not significantly influence the saltation cascade downwind over the period that the armor layer develops.

2296 4.6.3 Validation

2297 Validation of the proposed model is ongoing. Initially, validation will be focused on
2298 gross sediment transport rates in availability-limited systems. Few holistic measure-
2299 ments are available that monitor both the spatiotemporal variations in the sediment
2300 transport rate and the availability-limiting factors like moisture content and beach ar-
2301 moring concurrently (e.g. [Delgado-Fernandez et al., 2012](#); [Hoonhout et al., 2013](#)). Sites
2302 with detailed and frequent topographic measurements and hydrodynamic boundary
2303 conditions available can be found worldwide. These sites would be a good starting
2304 point for assessing the performance of the model compared to existing models. Using
2305 simplified, but generic descriptions of the hydraulic mixing and drying rate the model
2306 should already provide time series of aeolian sediment transport that adhere much
2307 better to the true nature of aeolian sediment transport events than existing models.
2308 [Delgado-Fernandez and Davidson-Arnott \(2011\)](#) and [de Vries et al. \(2014a\)](#) already
2309 indicated that the true nature of these events is not solely related to wind velocity
2310 and direction, but also to surges, seasons, spring/neap cycles, rain showers and other
2311 events that influence sediment availability. The variations in aeolian sediment trans-
2312 port due to these event-driven changes in sediment availability are not well captured
2313 by models that rely solely on the wind transport capacity. The model has added value
2314 if it improves the prediction of transport rates under such circumstances.

2315 4.7 CONCLUSIONS

2316 The AEOLiS model presented in this paper is the first aeolian sediment transport
2317 model that simulates spatiotemporal variations in bed surface properties and sedi-
2318 ment availability. Simulation of sediment availability is necessary as sediment avail-
2319 ability cannot be determined a-priori due to its recurrence relation with sediment
2320 transport. The presented model approach is a generalization of existing modeling

2321 concepts for aeolian sediment transport that include the influence of bed surface
2322 properties and limitations in sediment availability, like the shear velocity threshold
2323 and critical fetch, and is compatible with these concepts. The model uses an ad-
2324 vvection scheme following [de Vries et al. \(2014b\)](#) and a bed composition module that
2325 discretizes the bed in horizontal grid cells and vertical bed layers to account for spatial
2326 variations in bed surface properties. Temporal variations in sediment availability are
2327 not parameterized, but simulated using the bed composition module. The simulation
2328 of sediment availability reduces the need for complex spatiotemporal parameteriza-
2329 tions and consequently calibration. In this paper the influence of sediment sorting
2330 and beach armoring and the reversed process of hydraulic mixing on aeolian sedi-
2331 ment transport are illustrated using four prototype cases. The model can reproduce
2332 patterns in aeolian sediment availability and transport as observed in wind tunnel
2333 experiments that involve spatiotemporal variations in bed surface properties ([Nick-](#)
2334 [ling and McKenna Neuman, 1995](#); [Dong et al., 2004b](#)). Further, the model provides a
2335 generic framework to incorporate additional spatiotemporal varying processes that ei-
2336 ther influence sediment availability or the wind transport capacity with a minimum of
2337 parameterization. The framework allows relatively straightforward implementation
2338 of the effects of infiltration, evaporation, vegetation, buildings, and morphological
2339 feedback with the wind.

2340 From this paper the following conclusions can be drawn:

- 2341 1. A model for aeolian sediment transport was presented that simulates the pro-
2342 cesses of sediment sorting and beach armoring, the reversed process of hy-
2343 draulic mixing, interaction between sediment fractions in the air with sediment
2344 fractions in the bed and thereby the influence of spatiotemporal variations in
2345 sediment availability;
- 2346 2. The model can be seen as a generalization of existing approaches to incorporate
2347 limitations in sediment availability and the wind transport capacity in aeolian
2348 transport estimates and is compatible with approaches based on either shear
2349 velocity thresholds or critical fetch;
- 2350 3. The process of beach armoring can be a governing factor in aeolian sediment
2351 transport modeling and may reduce the estimated transport rates significantly
2352 and up to 95.0% in the presented prototype cases;
- 2353 4. The model can reproduce typical patterns in aeolian sediment transport with
2354 spatiotemporal variations in sediment availability obtained from measure-
2355 ments from the unrelated wind tunnel experiments described in [Nickling and](#)
2356 [McKenna Neuman \(1995\)](#) and [Dong et al. \(2004b\)](#), with a minimum parameteri-
2357 zation and calibration.

5

2358

2359

2360 SAND MOTOR HINDCAST

2361 *This chapter is intended to be published separately and was written accordingly, but has not*
2362 *been submitted to a particular journal yet.*

2363 **5.1 INTRODUCTION**

2364 In availability-limited coastal systems, the aeolian sediment transport rate is governed
2365 by the sediment availability rather than the wind transport capacity. Aeolian sediment
2366 transport models typically incorporate the sediment availability through the shear
2367 velocity threshold. However, the determination of appropriate threshold values in
2368 practice appears to be challenging as the shear velocity threshold tends to vary both
2369 spatially and temporally (Barchyn et al., 2014b). For example, soil moisture in the
2370 intertidal beach area fluctuates with the tidal phase and causes a local modulation of
2371 the shear velocity threshold. Moreover, a recurrence relation between sediment avail-
2372 ability, and thus the shear velocity threshold, and sediment transport exists that com-
2373 plicates the a-priori determination of an appropriate threshold value. Consequently,
2374 aeolian sediment transport models tend to perform poorly in availability-limited sys-
2375 tems.

2376 Sherman et al. (1998) and Sherman and Li (2012) summarized the performance
2377 of eight aeolian sediment transport models compared to field measurements on a
2378 sandy beach. Although it is unknown whether this coastal system was availability-
2379 limited, all models systematically overpredicted the measured aeolian sediment trans-
2380 port rates. This finding is in correspondence with an abundance of coastal field stud-
2381 ies in which aeolian sediment transport rates are overestimated by numerical models
2382 (e.g. Jackson and Cooper, 1999; Lynch et al., 2008; Davidson-Arnott and Bauer, 2009;
2383 Aagaard, 2014).

2384 In an attempt to explain the poor performance of aeolian sediment transport mod-
2385 els in coastal environments, many authors emphasized the importance of sediment
2386 availability and bed surface properties. Typical bed surface properties that are found
2387 along the coast and known to affect sediment availability are high moisture contents
2388 (e.g. Wiggs et al., 2004; Davidson-Arnott et al., 2008; Darke and McKenna Neuman,
2389 2008; McKenna Neuman and Sanderson, 2008; Udo et al., 2008; Bauer et al., 2009; Ed-
2390 wards and Namikas, 2009; Namikas et al., 2010; Scheidt et al., 2010), salt crusts (e.g.
2391 Nickling and Ecclestone, 1981), vegetation (e.g. Arens, 1996; Lancaster and Baas, 1998;
2392 Okin, 2008; Li et al., 2013; Dupont et al., 2014), shell pavements (e.g. van der Wal, 1998;
2393 McKenna Neuman et al., 2012) and sorted and armored beach surfaces (e.g. Gillette
2394 and Stockton, 1989; Gillies et al., 2006; Tan et al., 2013; Cheng et al., 2015). The influ-

ence of these bed surface properties on aeolian sediment availability and transport has been investigated and typically resulted in relations between bed surface properties and the shear velocity threshold (e.g. Howard, 1977; Dyer, 1986; Belly, 1964; Johnson, 1965; Hotta et al., 1984; Nickling and Ecclestone, 1981; Arens, 1996; King et al., 2005).

Modeling rather than parameterization of spatiotemporal variations in aeolian sediment availability can improve coastal aeolian sediment transport estimates. As tides only affect the intertidal beach area, lag deposits and salt crusts typically emerge from the dry beach area, and vegetation is often restricted to the dune area, sediment availability varies spatially. In addition, temporal variations in sediment availability are induced by tidal spring/neap cycles, rain showers, storm surges, seasonal variations in vegetation and progressive armoring of the beach. Due to self-grading of the sediment, progressive beach armoring creates a recurrence relation between sediment availability and transport that challenges the a-priori determination of the spatiotemporal variations in sediment availability. Process-based modeling of the instantaneous shear velocity threshold field can address these challenges and improve coastal aeolian sediment transport estimates.

This paper presents the first application of a two-dimensional (2DH) aeolian sediment availability and transport model (Hoonhout and de Vries, 2016d) to hindcast the development of the sub-aerial topography of an availability-limited coastal system. The model is unique in that it describes both spatial and temporal variations in aeolian sediment availability induced by the combined influence of sediment sorting, beach armoring and soil moisture content. The influence of spatiotemporal variations in aeolian sediment availability and the model performance are illustrated by a comparison between model results and a large scale sediment budgets analysis that identifies and quantifies the main sources and sinks for aeolian sediment in the coastal system (Hoonhout and de Vries, 2016a).

5.2 FIELD SITE

The Sand Motor (or Sand Engine) is an artificial 21 Mm^3 sandy peninsula protruding into the North Sea off the Delfland coast in The Netherlands (Figure 5.1, Stive et al., 2013). The Sand Motor was constructed in 2011 and its bulged shoreline initially extended about 1 km seaward and stretched over approximately 2 km along the original coastline. The original coast was characterized by an alongshore uniform profile with a vegetated dune with an average height of 13 m and a linear beach with a 1:40 slope. The dune foot is located at a height of approximately 5 m+MSL.

Due to natural sediment dynamics the Sand Motor distributes about 1 Mm^3 of sand per year to the adjacent coasts (Figure 5.1). The majority of this sand volume is transported by tides and waves. However, the Sand Motor is constructed up to 5 m+MSL and locally up to 7 m+MSL, which is in either case well above the maximum surge level of 3 m+MSL (Figure 5.2c). Therefore, the majority of the Sand Motor area is uniquely shaped by wind.

The Sand Motor comprises both a dune lake and a lagoon that act as large traps for aeolian sediment (Figure 5.1). The lagoon is affected by tidal forcing, although the tidal amplitude quickly diminished over time as the entry channel elongated. The tidal range of about 2 m that is present at the Sand Motor periphery (Figure 5.2c), is nowadays damped to less than 20 cm inside the lagoon (de Vries et al., 2015). Con-

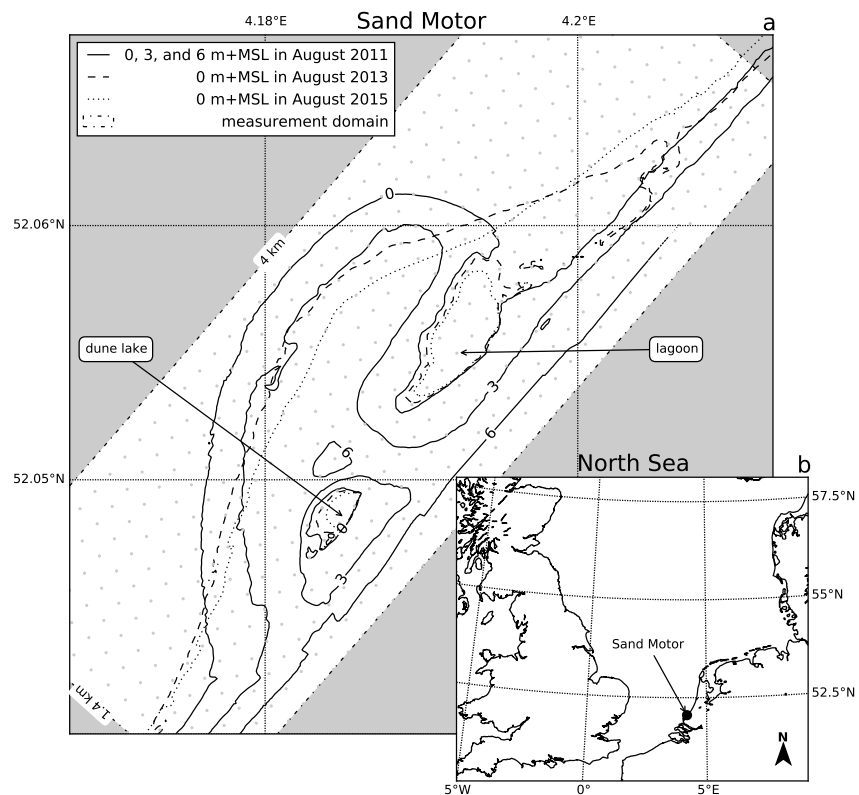


Figure 5.1: Location, orientation, appearance and evolution of the Sand Motor between construction in 2011 and 2015. The box indicates the measurement domain used in the remainder of this paper. A 100 x 100 m grid aligned with the measurement domain is plotted in gray as reference.

2440 subsequently, the tidal currents at the closed end of the lagoon, where most aeolian
 2441 sediment is trapped, are negligible.

2442 The dominant wind direction at the Sand Motor is south to southwest (Figure 5.2a).
 2443 However, during storm conditions the wind direction tends to be southwest to northwest.
 2444 During extreme storm conditions the wind direction tends to be northwest.
 2445 Northwesterly storms are typically accompanied by significant surges as the fetch is
 2446 virtually unbounded to the northwest, while surges from the southwest are limited
 2447 due to the presence of the narrowing of the North Sea at the Strait of Dover (Figure
 2448 5.1, inset).

2449 5.3 MODEL APPROACH

2450 A two-dimensional (2DH) model of the Sand Motor that includes limitations in sediment
 2451 availability is constructed and calibrated based on four years of field measurements
 2452 on wind, tides, waves and topography. The calibrated model is used to investigate
 2453 the influence of spatiotemporal variations in aeolian sediment availability on
 2454 sediment accumulation in the Sand Motor domain.

2455 To test that the Sand Motor mega nourishment is indeed an availability-limited
 2456 coastal system, the measured long-term sediment accumulation volumes (Hoonhout
 2457 and de Vries, 2016a) are first compared to a reference model that assumes no limitations
 2458 in sediment availability exist.

2459 5.3.1 Reference model

2460 A selection of equilibrium sediment transport formulations is used as reference model.
 2461 An equilibrium sediment transport formulation describes the wind transport capacity
 2462 in given conditions. In conjunction with a shear velocity threshold based on only a
 2463 constant uniform median grain size, an estimate of the potential aeolian sediment
 2464 accumulation in absence of availability-limitations can be obtained. The potential
 2465 aeolian sediment accumulation or cumulative wind transport capacity Q [m^3] in the
 2466 Sand Motor domain is estimated based on hourly averaged time series of the wind
 2467 speed u_z [m/s] and direction θ_u [$^\circ$] obtained from the KNMI meteorological station
 2468 in Hoek van Holland following:

$$Q = \sum q \cdot \frac{\Delta t \cdot \Delta y}{(1-p) \cdot \rho_p} \cdot f_{\theta_u} \quad (5.1)$$

2469 where the temporal resolution $\Delta t = 1$ h, the alongshore span of the domain $\Delta y = 4$
 2470 km, the porosity $p = 0.4$, the particle density $\rho_p = 2650 \text{ kg/m}^3$, the sediment transport
 2471 rate q is given by the equilibrium sediment transport formulation (Table 5.1) and f_{θ_u}
 2472 is a factor to account for the wind direction. The wind direction can be accounted for
 2473 by only including the onshore wind component with respect to the original coastline
 2474 orientation. However, given the typical Sand Motor geometry (Figure 5.1), sediment
 2475 is likely to be trapped in the dune lake and lagoon even with alongshore wind. There-
 2476 fore it can be assumed that the onshore wind component will provide a lower limit of
 2477 the cumulative wind transport capacity. Similarly, an upper limit can be obtained by
 2478 assuming that all onshore wind directions contribute equally to the cumulative wind
 2479 transport capacity. For the upper limit the factor f_{θ_u} is defined as:

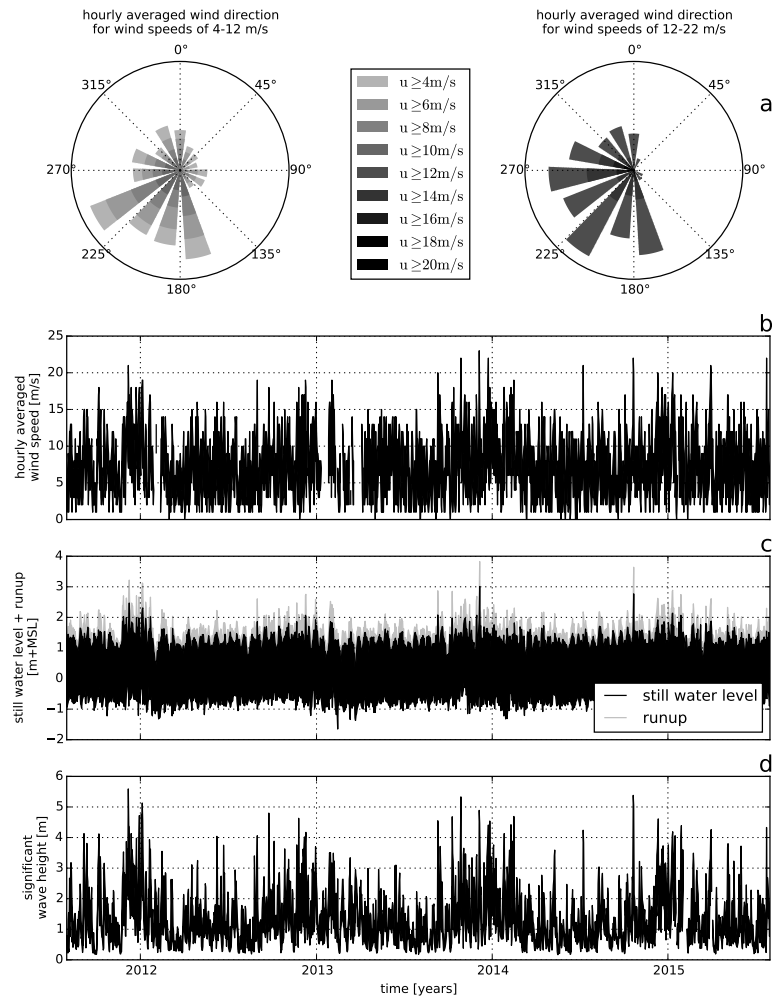


Figure 5.2: Wind and hydrodynamic time series from 2011 to 2015. Hourly averaged wind speeds and directions are obtained from the KNMI meteorological station in Hoek van Holland (upper panels). Offshore still water levels, wave heights and wave periods are obtained from the Europlatform (lower panels). Runup levels are estimated following Stockdon et al. (2006).

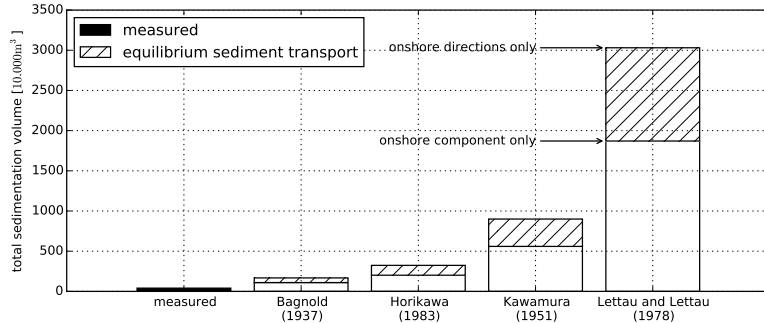


Figure 5.3: Comparison of the cumulative wind transport capacity according to a selection of equilibrium sediment transport formulations and measured total sedimentation in the Sand Motor domain. The equilibrium sediment transport is based on an hourly averaged wind speed and direction time series from September 1, 2011 until September 1, 2015. Offshore wind directions are discarded. For the upper boundary of each estimate all wind directions are weighted equally. For the lower boundary of each estimate the wind directions are weighted according to the magnitude of the onshore component.

$$f_{\theta_u} = \begin{cases} 1 & \text{if } \cos(312^\circ - \theta_u) \geq 0 \\ 0 & \text{if } \cos(312^\circ - \theta_u) < 0 \end{cases} \quad (5.2)$$

while for the lower limit the factor f_{θ_u} is defined as:

$$f_{\theta_u} = \max(0 ; \cos(312^\circ - \theta_u)) \quad (5.3)$$

where 312° accounts for orientation of the original coastline. Figure 5.3 presents an overview of the cumulative wind transport capacity in the Sand Motor domain over the period between September 1, 2011 and September 1, 2015 according to a selection of equilibrium sediment transport formulations and in comparison with the measured accumulation volumes. The estimates of the wind transport capacity show a large variation between formulations that are mainly due to the incorporation of the shear velocity threshold. However, all formulations overestimate the measured sediment accumulation in the Sand Motor domain with at least a factor 3–4. The large variation and consistent overestimation is in accordance with the review of aeolian sediment transport models presented by Sherman and Li (2012). The consistent overestimation of the measured sedimentation volumes in the Sand Motor domain suggest that the Sand Motor is indeed an availability-limited coastal system.

5.3.2 Schematization

A two-dimensional (2DH) aeolian sediment availability and transport model for the Sand Motor mega nourishment is constructed for the four years between September

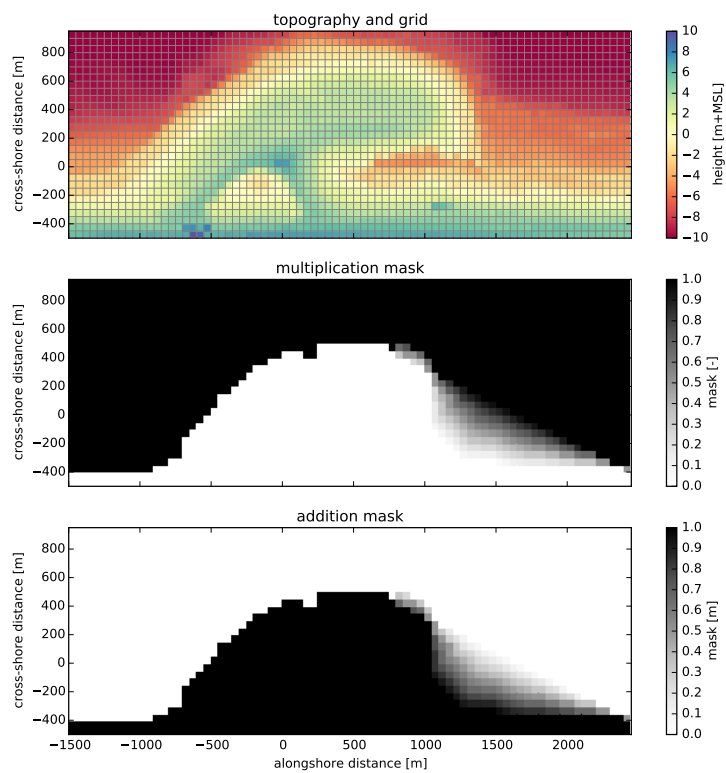


Figure 5.4: Model grid and topography based on the topographic survey of August 3, 2011 (upper panel) and hydrodynamic mask used to limit tidal and wave motions in the dune lake and lagoon (middle and lower panels). Water levels and wave heights are uniformly imposed to the model and multiplied by the multiplication mask and subsequently increased with the addition mask.

Table 5.1: Equilibrium sediment transport formulations, coefficient values* and the ratio between measurements and model results.

Reference	Equation	C	Ratio
Bagnold (1937b)	$q = C \frac{\rho_a}{g} \sqrt{\frac{d_n}{D_n}} (u_* - u_{*th})^3$	1.8	3 – 4
Horikawa et al. (1983)	$q = C \frac{\rho_a}{g} (u_* + u_{*th})^2 (u_* - u_{*th})$	1.0	5 – 8
Kawamura (1951)	$q = C \frac{\rho_a}{g} (u_* - u_{*th})^2 (u_* - u_{*th})$	2.78	14 – 22
Lettau and Lettau (1978)	$q = C \frac{\rho_a}{g} \sqrt{\frac{d_n}{D_n}} (u_* - u_{*th}) u_*^2$	6.7	46 – 75

* Other values are the shear velocity $u_* = \alpha \cdot u_z$ m/s, the shear velocity threshold $u_{*th} = \alpha \cdot 3.87$ m/s, the conversion factor from free-flow wind velocity to shear velocity $\alpha = 0.058$, the air density $\rho_a = 1.25$ kg/m³, the particle density $\rho_p = 2650.0$ kg/m³, the gravitational constant $g = 9.81$ m/s², the nominal grain size $d_n = 335$ µm, a reference grain size $D_n = 250$ µm and the height above the bed of the wind measurement $z = 10$ m.

2496 1, 2011 and September 1, 2015, which is shortly after the nourishment was placed.
2497 The model's topography and grid are based on the measured topographies of August
2498 3, 2011 and later. The topographies are rotated 48° and interpolated to a 50 × 50 m
2499 grid spanning 1.5 km cross-shore and 4 km alongshore with respect to the original
2500 coastline, not including the dunes (Figure 5.4, upper panel).

2501 Four years of hourly wind speed and direction data measured at 10 m above the bed
2502 is obtained from the KNMI meteorological station at Hoek van Holland (Figure 5.2a,b).
2503 Hourly offshore water levels and wave heights are obtained from the Europlatform
2504 for the same period (Figure 5.2c,d).

2505 An average lognormal grain size distribution with a median diameter $d_{50} = 335$ µm
2506 is used as measured at the Sand Motor field site. The sand fractions cover a range
2507 from 0.1 to 2 mm. The amount of shells and other roughness elements in the origi-
2508 nally nourished sand is estimated to be 5%. The estimate is based on three sediment
2509 samples obtained from the field site 0.5 m below the bed surface. Additional fractions
2510 ranging from 2 to 32 mm are added according to a lognormal distribution to account
2511 for the presence of roughness elements in the bed. The grain size distribution is used
2512 to populate the initial bed that consists of 10 bed composition layers with a thickness
2513 of 1 cm each.

2514 The hindcast aims at the large scale and long term sedimentation volumes as pre-
2515 sented by Hoonhout et al. (2016a). Therefore an efficient, but diffusive, implicit Euler
2516 Backward scheme with a timestep of 1 h is used that does not resolve high frequency
2517 variations in wind or sediment transport. Consequently, the model produces smooth
2518 solutions that describe hourly steady states based on the instantaneous average wind
2519 speed and sediment availability.

2520 Bagnold (1937b) is selected as equilibrium sediment transport formulation as it is
2521 derived separately for different grain sizes and therefore suitable for multi-fraction
2522 aeolian sediment transport. Alternative formulations (Table 5.1) are derived for wider
2523 grain size distributions that do not necessarily result in a monotonic relation between
2524 the grain size and the sediment transport rate (e.g. Kawamura, 1951; Horikawa et al.,
2525 1983). Such non-monotonic relation is unrealistic in a multi-fraction context as it
2526 would result in a preference to transport both fine sediment and large elements that
2527 are considered non-erodible. Moreover, the formulation of Bagnold (1937b) overesti-

2528 mates the measured aeolian sediment transport rates in the Sand Motor domain less
 2529 compared to alternative formulations (Table 5.1, rightmost column).

2530 Water levels and wave heights are initially uniformly imposed to the model. Con-
 2531 sequently, the tidal range, mean water level and wave heights that are present at the
 2532 Sand Motor periphery are also present in the dune lake and lagoon. In reality the
 2533 tidal range and wave heights in the dune lake and lagoon are much lower, while the
 2534 mean water level in the dune lake and lagoon is elevated compared to mean sea level
 2535 (de Vries et al., 2015). To account for these spatial differences in hydrodynamics a
 2536 hydrodynamic mask is applied (Figure 5.4, middle and lower panel; Appendix B.3.4)

2537 Subtidal changes in topography are not simulated by the model. The subtidal
 2538 changes can be important to aeolian sediment transport as the location and size of
 2539 aeolian sediment erosion and deposition areas might change. To account for these
 2540 changes, measured topographies are imposed to the model through a Basic Model
 2541 Interface (BMI, Peckham et al., 2013, Appendix B.4).

2542 All measured topographies in the period between September 1, 2011 and Septem-
 2543 ber 1, 2015 are linearly interpolated in time as to obtain daily updates of the Sand
 2544 Motor's topography. The hydrodynamic mask is updated along with the topography.
 2545 The presented aeolian sediment transport rates are based on the time-integrated en-
 2546 trainment and deposition rates that are computed by the model rather than differences
 2547 in topography.

2548 5.3.3 Calibration

2549 The model is calibrated on the shape of roughness elements that emerge from the bed
 2550 and shelter the sand surface from wind erosion, the drying rate of the soil and the
 2551 time needed for the sediment transport to adapt to changing wind conditions. These
 2552 processes are represented in the model by parameters for which data or literature can
 2553 only provide approximate values:

- 2554 1. σ , as used in the formulation of Raupach et al. (1993, Equation 4.2), is the ratio
 2555 between the basal and frontal area of the roughness elements that constitute the
 2556 beach armor layer.
- 2557 2. T_{dry} is the time scale at which the beach dries out after flooding (Equation B.26).
 2558 It represents the time in which the soil moisture content halves in case the beach
 2559 is not inundated and no evaporation occurs.
- 2560 3. T is the adaptation time scale in the right-hand side of the advection equation
 2561 (Equation 4.7). It represents the time scale to which the sediment transport
 2562 adapts to variations in the wind conditions and sediment availability.

2563 The implementation of roughness elements is characterized by three calibration pa-
 2564 rameters: m , β and σ (Equation 4.13). m is a factor to account for the difference
 2565 between the mean and maximum shear stress and is usually chosen as 0.5 for field
 2566 applications (Raupach et al., 1993; McKenna Neuman et al., 2012). Numerically it is
 2567 irrelevant if β or σ is calibrated as they only appear as a ratio $\frac{\beta}{\sigma}$ in the model imple-
 2568 mentation. As β is the ratio between the drag coefficient of the roughness elements
 2569 alone and the drag coefficient of the unarmored sandy bed, the value can be assumed

2570 to be reasonably generic. In contrast, σ depends on the shape and protrusion of the
 2571 roughness elements and therefore depends on the field site and varies in time. For
 2572 example, a spherical object placed on top of the bed would be represented by $\sigma = 1$,
 2573 while a spherical object protruding halfway through the bed (hemisphere) would be
 2574 represented by $\sigma = 2$. Consequently, calibration of σ seems to be preferable as it is
 2575 less certain. Wind tunnel experiments presented by McKenna Neuman et al. (2012)
 2576 investigated the influence of a lag deposits, consisting of shells and shell fragments,
 2577 on aeolian sediment transport. Values for the calibration coefficients m and β were
 2578 found to be 0.5 and 130 respectively and are adopted for the Sand Motor hindcast. An
 2579 optimal average value for σ is obtained by systematic variation between 2 and 20.

2580 The drying rate of the beach (T_{dry}) depends on many factors, like grain size, soil
 2581 moisture content, groundwater level, wind speed and solar radiation. The use of
 2582 a single time scale as aggregate for these processes is an oversimplification of reality.
 2583 Therefore a wide range of parameter values is covered in the calibration. T_{dry} is varied
 2584 between 0.1 and 10 hours where the former results in virtually instant drying and the
 2585 latter results in an intertidal beach that is permanently too moist for aeolian sediment
 2586 transport to be initiated.

2587 The adaptation time scale (T), that represents the swiftness of aeolian sediment
 2588 transport to adapt to changing wind conditions, is in the order of seconds (Davidson-
 2589 Arnott et al., 2008; de Vries et al., 2014b). As the model time step is orders of mag-
 2590 nitude larger, the model effectively solves steady states and the value for T will not
 2591 affect temporal variations in sediment transport. However, the adaptation time scale
 2592 also affects the development of the saltation cascade in space. Sediment transport
 2593 increases in downwind direction from a zero-flux boundary, like the water line in
 2594 case of onshore wind, with a rate that is governed by the value of T . Consequently, T
 2595 influences the width of the source area in case of abundant sediment availability. T is
 2596 varied between 1 and 10 seconds.

2597 The calibration is performed based on the bi-monthly erosion and deposition vol-
 2598 umes as measured in the Sand Motor domain (Hoonhout and de Vries, 2016a). The
 2599 erosion and deposition volumes are determined within seven predefined zones (Fig-
 2600 ure 5.5) that aim to separate areas with marine influences from areas without marine
 2601 influences, and separate areas with net aeolian erosion from areas with net aeolian de-
 2602 position. The zonation is based on the 0, 3 and 5 m+MSL contour lines that roughly
 2603 correspond with the mean water level, maximum runup level or berm edge and the
 2604 dune foot respectively. The average R^2 value of the time series for erosion and deposi-
 2605 tion is used as benchmark. The R^2 value represents the fraction of explained variance
 2606 and is defined as:

$$R^2 = \frac{\sum_n [V_{\text{measured}}^n - \bar{V}_{\text{measured}}^n]^2}{\sum_n [V_{\text{measured}}^n - \bar{V}_{\text{measured}}^n]^2} \quad (5.4)$$

2607 where V^n is the measured or modeled sediment volume in time period n . The overbar
 2608 denotes time-averaging. In addition the root-mean-square error (RMSE) is presented
 2609 as absolute measure for the model accuracy, which is defined as:

$$\text{RMSE} = \sqrt{\sum_n [V_{\text{measured}}^n - V_{\text{model}}^n]^2} \quad (5.5)$$

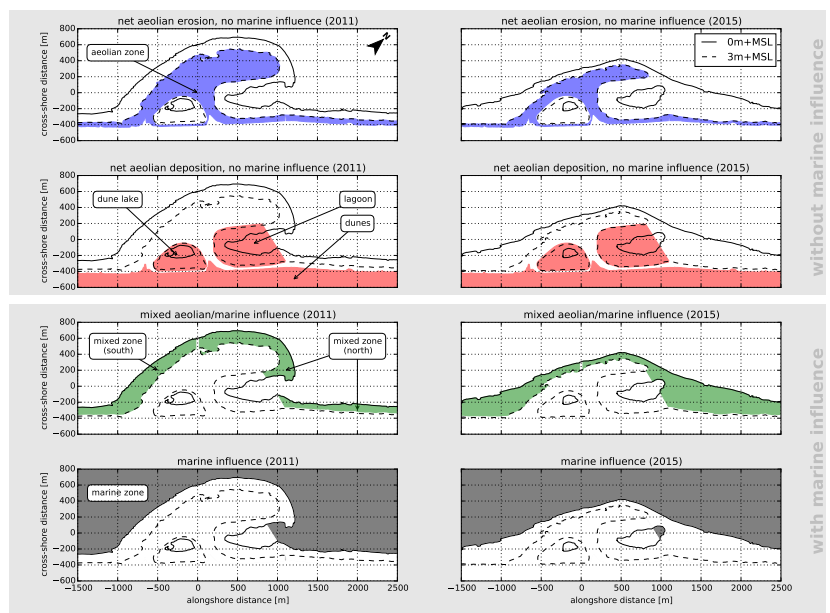


Figure 5.5: Zonation of the Sand Motor domain into zones with net aeolian erosion and no marine influence, net aeolian deposition and no marine influence, mixed aeolian/marine influence and marine influence. Zonation is based on the 0, 3 and 5 m+MSL contour lines that roughly correspond with the mean water level, maximum runup level or berm edge and the dune foot respectively. Left panels: 2011. Right panels: 2015. Source: [Hoonhout and de Vries \(2016a\)](#).

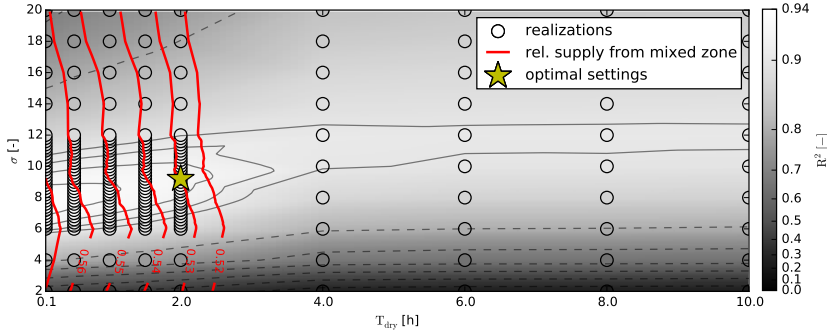


Figure 5.6: Systematic variation of calibration parameters σ and T_{dry} with $T = 1$ s. The circles indicate the realizations made. The colored background depicts a linear interpolation of the R^2 values with respect to the data presented in Figure 2.6. The solid isolines depict R^2 values from 0.90 to 0.93, while the dashed isolines depict R^2 values from 0.0 to 0.9. The red lines depict the relative supply from the mixed zones ranging from 52% to 57%. The yellow star indicates the optimal value model settings.

2610 The calibration itself is performed in three steps:

- 2611 1. A coarse calibration on σ and T_{dry} .
 2612 2. A calibration on T using the provisional optimal settings for σ and T_{dry} .
 2613 3. A fine calibration on σ and T_{dry} using the optimal setting for T .

2614 5.4 RESULTS

2615 The optimal model settings were chosen from 150 realizations (Figure 5.6). The opti-
 2616 mal realization has an R^2 value of 0.93 and a RMSE of $3 \cdot 10^4$ m³. The corresponding
 2617 optimal parameter settings are found to be $\sigma = 9.2$, $T_{\text{dry}} = 2$ h and $T = 1$ s. These
 2618 settings were ultimately selected from a cluster of realizations with comparable R^2
 2619 values based on the relative sediment supply from the mixed zones (Figure 5.5, third
 2620 row) at the end of the simulation. An overview of all model settings for the calibrated
 2621 model is given in Appendix C.

2622 Figure 5.7 shows that erosion from the aeolian zone (Figure 5.5, first row) is most
 2623 pronounced in the first year and least in the second year in both the measurements
 2624 and the model results. Also the deposition of aeolian sediment in the dune lake and
 2625 lagoon (Figure 5.5, second row) is observed in both the measurements and model
 2626 results, although the model underestimates these deposited volumes. The deposition
 2627 in the dune lake and lagoon is also more localized in the measurements than in the
 2628 model results. The spatial variability in the erosion of the aeolian zone is larger in the
 2629 measurements than in the model results. The large variability measured in the mixed
 2630 zone is not present in the model results as hydrodynamic sediment transport is not
 2631 simulated.

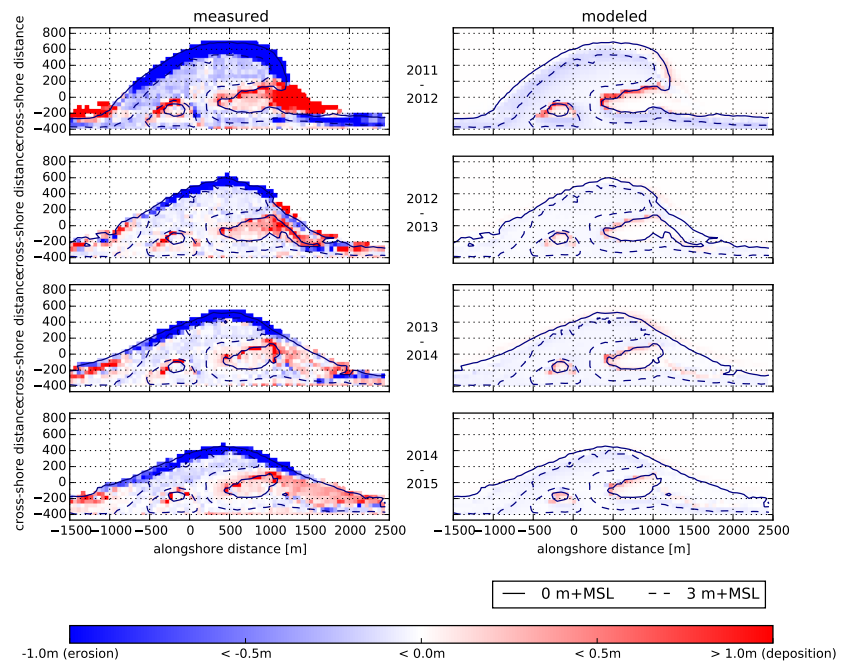


Figure 5.7: Measured and modeled yearly sedimentation and erosion above 0 m+MSL. Model results only include aeolian sediment transport as hydrodynamic sediment transport is not computed. Comparisons are made between the September surveys of each year.

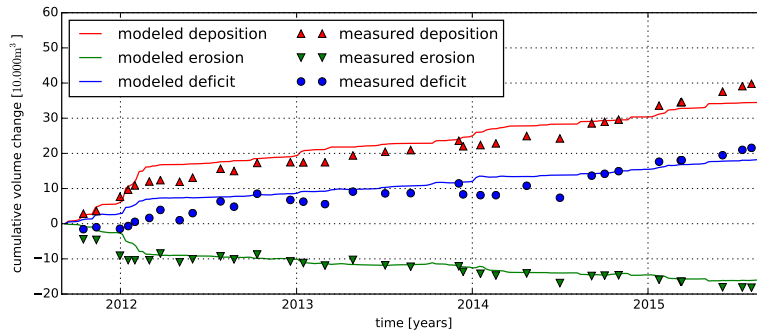


Figure 5.8: Measured and simulated net volume change of erosion and deposition volumes as presented in Figure 2.6.

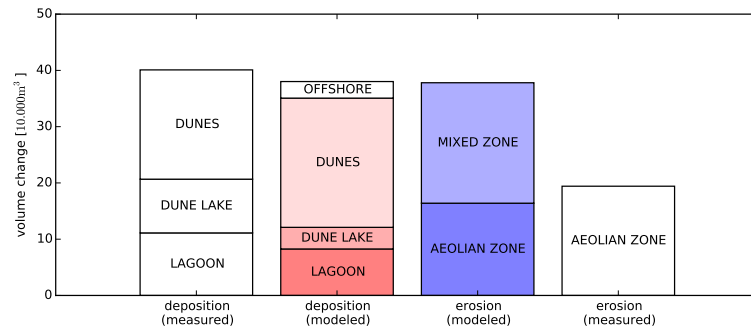


Figure 5.9: Total erosion and deposition volumes at the end of the simulation and measured total erosion and deposition volumes as presented in Figure 2.5.

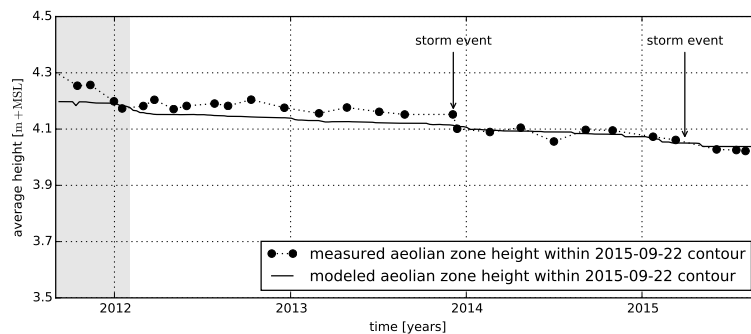


Figure 5.10: Measured and simulated average beach height in the aeolian zone as presented in Figure 2.8.

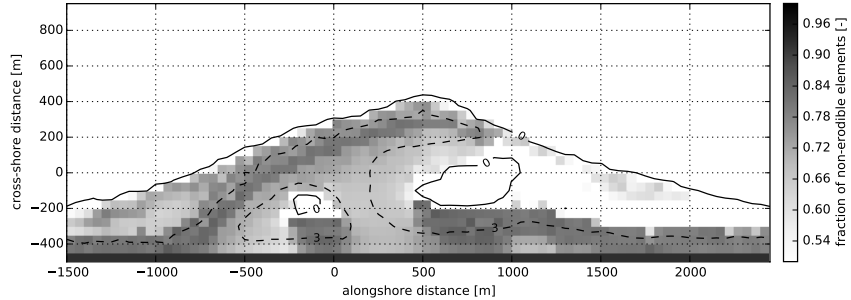


Figure 5.11: Simulated shell fraction in the aeolian zone at the end of the simulation.

2632 The development of the total erosion and deposition volumes in the Sand Motor
 2633 domain in the four year period is represented well by the model (Figure 5.8). The
 2634 dune accumulation volume is overestimated at the expense of the sediment volumes
 2635 deposited in the dune lake and lagoon (Figure 5.9). As the dune area is not included in
 2636 the model domain, the sediment flux over the onshore boundary is assumed to settle
 2637 in the dunes entirely. The total sediment accumulation at the end of the simulation is
 2638 underestimated by 12% as the offshore sediment deposits are not included in the large
 2639 scale sediment budget analysis that are used for comparison. The underestimation is
 2640 unique for the last nine months of the simulation as the model overestimates the total
 2641 sediment accumulation with 5% on average (Figure 5.8). The relative importance of
 2642 the mixed zone as supplier of aeolian sediment is well captured.

2643 The change in beach height within the most recent 3 m+MSL contour, that marks
 2644 the aeolian zone, is represented by the model as the R^2 value is 0.71 and the RMSE
 2645 is about 4 cm or 12% of the average bed level change (Figure 5.10). As the change in
 2646 beach height is computed within the most recent 3 m+MSL contour, the discrepancy is
 2647 illustrative for the differences in spatial variability in erosion between measurements
 2648 and model results. The lowering of the beach in the aeolian zone in the first half year
 2649 of the simulation is particularly underestimated, while the accelerated erosion in this
 2650 period is well captured in the total sediment transport. This indicates that sediment
 2651 is eroded from outside the most recent 3 m+MSL contour.

2652 The coverage of non-erodible elements $\sigma\lambda$ [-] (Equation 4.14) in the aeolian zone
 2653 varies between 60% and 80% at the end of the simulation (Figure 5.11). The coverage
 2654 is high compared to the 10% – 20% shell coverage estimated to be present at the Sand
 2655 Motor above 3 m+MSL based on gridded photographs.

2656 Both the spatial and temporal variations in aeolian sediment availability are crucial
 2657 for an accurate description of total sedimentation and erosion volumes as well as an
 2658 accurate prediction of the aeolian sediment source and deposition areas. Figure 5.12
 2659 compares the total sedimentation volume according to measurements, the calibrated
 2660 model and additional simulations, that are variations of the calibrated model in which
 2661 spatial and/or temporal variations in the shear velocity threshold are averaged out.
 2662 During these additional simulations the shear velocity threshold is not computed by
 2663 the model, but space- and/or time-averaged thresholds based on the model results

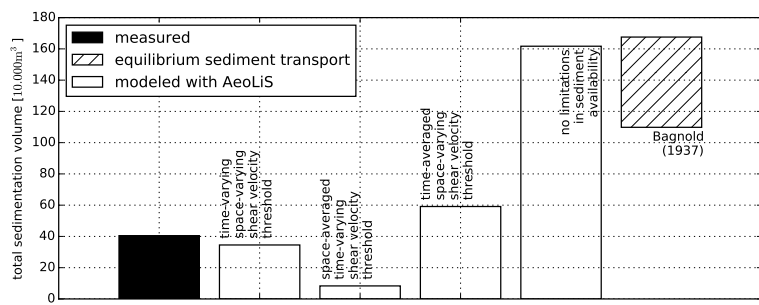


Figure 5.12: The influence of time-varying and space-varying shear velocity thresholds on the total sedimentation volume. The two leftmost bars depict the measured and modeled sedimentation volume as obtained from the calibrated model (Figure 5.9). The middle two bars depict results from two separate model simulations in which a space-averaged threshold time series or a time-averaged threshold field is imposed respectively. The threshold averages are based on the result from the calibrated model. The two rightmost columns depict a result from a separate model simulation with a constant uniform threshold based on only a constant uniform median grain size and the estimated equilibrium sediment transport following [Bagnold \(1937b\)](#) respectively (Table 5.1).

2664 of the calibrated model are imposed. Negligence of the spatial variations results in
2665 a 79% underestimation of the total sedimentation volume and a relative contribution
2666 of 8% of the mixed zones. The negligence of the temporal variations results in a 46%
2667 overestimation of the total sedimentation volume and a relative contribution of 86%
2668 of the mixed zones. In addition, a simulation without limitations in sediment avail-
2669 ability overestimates the measured total sedimentation volumes with 400%, which is
2670 comparable to the wind transport capacity following [Bagnold \(1937b, Figure 5.3\)](#).

2671 **5.5 DISCUSSION**

2672 The model results show that multi-annual aeolian sediment erosion and deposition
2673 volumes, and the relative importance of the mixed zones as source of aeolian sedi-
2674 ment are reproduced with reasonable accuracy. This suggests that indeed significant
2675 limitations in sediment availability, due to soil moisture content and beach armoring,
2676 govern aeolian sediment transport in the Sand Motor domain. A comparison with a
2677 simulation without limitation in sediment availability suggests that aeolian sediment
2678 availability in the Sand Motor domain is limited to about 25% – 35% of the wind
2679 transport capacity.

2680 The negligence of spatial variations causes the model to underestimate the mea-
2681 sured total sedimentation volume. The sediment supply from the relatively small
2682 mixed zone is marginalized as the imposed space-averaged shear velocity threshold
2683 is relatively high. In contrast, the negligence of temporal variations causes the model
2684 to overestimate the measured total sedimentation volume. The sediment supply from
2685 the mixed zones is increased as the effect of its periodic flooding is averaged out. At
2686 the same time, the sediment supply from the aeolian zone is decreased as the influ-
2687 ence of beach armoring affects sediment availability from the start of the simulation
2688 rather than after the development of the beach armor layer. Therefore, the total sed-
2689 imentation volume is not only overestimated, but also the importance of the mixed
2690 zones as supplier of aeolian sediment.

2691 **5.5.1 Seasonal and local variations in sedimentation and erosion**

2692 The model can reproduce multi-annual trends in sedimentation volume, which is the
2693 aim of the hindcast, but seasonal and local variations are sometimes not represented
2694 by the model. An analysis of these variations is interesting as they influence the
2695 accuracy of specific model results.

2696 Average wind speeds tend to be elevated in December and January (Figure 5.2),
2697 which leads to short periods of accelerated sediment accumulation in the beginning
2698 of 2012, 2013 and 2015 that are captured well by the model. Early 2014 no accelerated
2699 sediment accumulation is measured, while the model simulation shows an increase
2700 in sediment accumulation originating from the mixed zones similar to other years.

2701 The discrepancy early 2014 might be explained by topographic changes induced
2702 by hydrodynamic forces. On December 5th, 2013 an exceptional storm hit the Dutch
2703 coast. During this storm a significant decrease in aeolian deposits in the lagoon was
2704 observed, while deposits in the dunes and dune lake increased only marginally. The
2705 assumption that the closed end of the lagoon is mainly governed by aeolian sediment
2706 transport might be violated in these exceptional conditions. At the same time, the

erosion of the aeolian zone that day equaled the total erosion of the aeolian zone that year. Consequently, the total subaerial sediment volume decreased that day with about $1 \cdot 10^4 \text{ m}^3$, possibly caused by hydrodynamic forces. This suggests that the simplified hydrodynamics, despite the use of a hydrodynamic mask, are a limiting factor in describing the Sand Motor's subaerial morphodynamics during extreme storms.

In the first months of the simulation, the total sediment accumulation is well represented, but erosion of the aeolian zone is underestimated. As beach armoring is the most important availability limitation in the aeolian zone, this suggests that the armoring rate is overestimated by the model. The armoring rate is mainly influenced by initial shell fraction of 5%, which might be overestimated. Alternatively, the initially uniform distribution of shells in the bed is not an accurate representation of reality.

Measured erosion and deposition rates exceed modeled erosion and deposition rates in the final nine months of the simulation. In this period dune growth seems to accelerate, while neither the deposition in the dune lake and lagoon did accelerate nor did the wind speed increase. The apparent acceleration is therefore solely found in the half yearly lidar measurements of the dune area (Hoonhout and de Vries, 2016a) and is consequently based on a single data point. Despite the uncertainty involved in the measured acceleration, also precipitation rates, that were up to 70% lower in this period compared to the same period in other years, might explain the discrepancy at the end of the simulation (Jackson and Nordstrom, 1998). For the hindcast no precipitation time series are imposed as the effect on the aeolian sediment transport rate is not properly understood yet. Consequently, the calibration of the model might have resulted in an overestimated importance of beach armoring to compensate for the negligence of precipitation.

The distribution of the aeolian sediment deposits over the dune lake, lagoon and dunes is not represented well as deposits in the dune lake and lagoon are underrepresented. Additional hydrodynamic and hydrologic processes, like wind setup and groundwater seepage, might cause the entrapment area in reality to be larger than modeled. But more importantly, the dune lake and lagoon are positioned in the lee of the Sand Motor crest with respect to the predominant southwesterly wind direction. The height difference between the Sand Motor crest and the water level in the lagoon and dune lake is several meters, which is likely to influence the local wind field significantly. The probable decrease in wind shear in the lee of the Sand Motor crest promotes deposition of aeolian sediment and likely hampers supply to the dunes. These local variations in wind shear are not included in the simulations.

5.5.2 Beach armoring, sediment availability and the shear velocity threshold

The influence of beach armoring is reflected in the model by both σ and the roughness density λ (Equation 4.13 and 4.14). The optimal value for σ was found to be 9.2, which is high compared to the value of 4.2 found by McKenna Neuman et al. (2012). The difference suggests that the roughness elements at the Sand Motor protrude less from the bed compared to what was found in the wind tunnel experiments. Consequently, the importance of beach armoring would be relatively low at the Sand Motor. However, the low σ value is largely compensated by the roughness density λ reflected in a shell coverage $\sigma\lambda$ that is high compared to what was found in the wind tunnel experiments (12% – 43% on average) and what is found at the Sand Motor field site

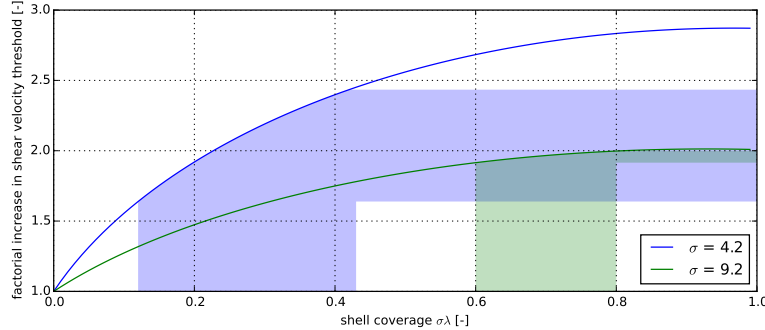


Figure 5.13: Relation between shear velocity threshold, shell coverage and σ according to Raupach et al. (1993, Equation 4.13). The shaded areas indicate the relevant parameter ranges from McKenna Neuman et al. (2012) (blue) and the model results (green).

(10% – 20%). Figure 5.13 shows that the combination of high shell coverage and σ value results in a very similar increase of the shear velocity threshold compared to the wind tunnel experiments presented by McKenna Neuman et al. (2012).

The reason that the model calibration resulted in this particular value for σ is that the model does not differentiate between the fluid and impact velocity threshold. Therefore, the roughness elements in the model affect the initiation of sediment transport equal to the continuation of sediment transport. The potential reduction in sediment availability increases with a decreasing value for σ (if $m = 0.5$, Figure 5.13) and is implemented through an increase in shear velocity threshold. The shear velocity threshold also affects aeolian sediment already in transport and originating from upwind, unarmored beach areas, like the mixed zones. Sediments from upwind areas are therefore partially deposited in the aeolian zone as soon a beach armor layer develops. For low values for σ the local deposition of sediment from upwind areas is already significant with low shell coverage. Low σ values therefore reduce the total sediment accumulation in the dunes quickly. In order for the model to provide reasonable total sediment transport rates, a higher value for σ was found in the calibration that ultimately induces a higher shell coverage. The value for σ therefore does not only represent a spatiotemporal averaged emergence of roughness elements, but also a compromise between its effect on the fluid and impact velocity threshold.

5.6 CONCLUSIONS

The Sand Motor hindcast shows that the reduction of aeolian sediment availability due to soil moisture and beach armoring can largely explain the low accumulation volumes in the Sand Motor domain. The AeoliS model has shown to be quantitatively valuable and practically applicable. The model provides a framework for the description of complex spatiotemporal variations in aeolian sediment availability and its relation to sediment transport that has not yet been exploited in full.

2778 From the hindcast the following conclusions can be drawn:

- 2779 • The AEOLiS model is able to reproduce multi-annual aeolian sediment transport
2780 rates in the Sand Motor domain in the four years after its construction with a
2781 RMSE of $3 \cdot 10^4$ m³ and R² of 0.93 when time series of measured and modeled
2782 total aeolian sediment transport volumes are compared.
- 2783 • The AEOLiS model is able to reproduce large scale spatial patterns in aeolian
2784 sediment transport in the Sand Motor domain in the four years after its con-
2785 struction, but underestimates the deposition in the dune lake and lagoon.
- 2786 • The AEOLiS model overestimates the total sedimentation volume with 5% on
2787 average, but underestimates the total sedimentation volume with 12% at the end
2788 of the simulation. The discrepancy at the end of the simulation might be caused
2789 by a particularly dry season as precipitation is not included in the simulations.
- 2790 • The AEOLiS model is able to capture the seasonal variations in sediment trans-
2791 port in all years, except for early 2014 when significant morphological change is
2792 possibly related to hydrodynamic sediment transport that is not included in the
2793 simulations.
- 2794 • The AEOLiS model overestimates the shell coverage, which compensates the
2795 high value for σ. The high σ value is a compromise between the fluid and
2796 impact threshold that are currently assumed to be equal.
- 2797 • The combination of spatial and temporal variations in aeolian sediment avail-
2798 ability, due to the combined influence of soil moisture, sediment sorting and
2799 beach armoring, and the feedback between aeolian sediment availability and
2800 transport is essential for an accurate estimate of the total sedimentation volume
2801 and the corresponding aeolian sediment source areas in the Sand Motor domain.

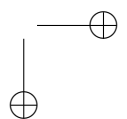
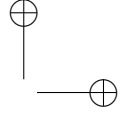
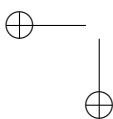
2802

Part III

2803

DISCUSSION AND CONCLUSIONS

2804



6

2805
2806

2807 DISCUSSION

2808 This thesis explored the nature of aeolian sediment availability. Aeolian sediment
2809 availability is generally associated with the shear velocity threshold. Alternatively,
2810 sediment availability can be expressed in terms of critical fetch (Bauer and Davidson-
2811 Arnott, 2002) or explicitly following de Vries et al. (2014a). The latter two approaches
2812 deviate rather radically from the legacy of aeolian research. Both discard the abund-
2813 antly available relations between bed surface properties, sediment availability and
2814 the shear velocity threshold. Instead, they describe sediment availability in new terms
2815 for which no quantification is known. In Chapter 4 it is argued that the new ap-
2816 proaches have a right to exist as they allow for an increased complexity in situations
2817 that can be described by models. Ultimately, the approach of de Vries et al. (2014a)
2818 is adopted for this thesis and adapted to support multi-fraction sediment transport
2819 in order to simulate sediment sorting and beach armoring that introduces feedback
2820 between aeolian sediment availability and transport in aeolian sediment transport
2821 modeling.

2822 The model approach presented in this thesis is a unification of the classic approach
2823 based on the shear velocity threshold and the approach of de Vries et al. (2014a).
2824 Whereas de Vries et al. (2014a) use a user-defined value for the sediment availabil-
2825 ity m_a (or S_e) to truncate the instantaneous sediment transport in their model, the
2826 approach presented in this thesis uses simulation to determine the local sediment
2827 availability $m_{a,k}$. The weighting factor \hat{w}_k is subsequently adapted to the local sedi-
2828 ment availability (Equation 4.9). Since the weighting factor \hat{w}_k is essentially a space-
2829 and time-dependent modification to the shear velocity threshold, this new approach
2830 connects the field of availability-limited aeolian sediment transport modeling with the
2831 long history of aeolian research.

2832 Availability-limited aeolian sediment transport modeling can be further improved
2833 by distinguishing between the fluid and impact threshold in future versions of the pre-
2834 sented model. The presented model provides a framework in which such distinction
2835 can be made rather naturally. The bed interaction parameter essentially implements
2836 this distinction already for armored beach surfaces, but a more generic implemen-
2837 tation is required for coastal systems with large spatial variations in sediment avail-
2838 ability. A key issue is still that relations between bed surface properties, sediment
2839 availability and the shear velocity threshold are typically derived as bulk formula-
2840 tion for the fluid and impact threshold together. A proper implementation of the
2841 fluid and impact threshold in the presented model therefore depends on a substantial
2842 investment in data collection (e.g. Martin and Kok, 2016).

2843 The presented model for availability-limited aeolian sediment transport can also be
2844 applied to availability-abundant coastal systems. However, much of the complexity in
2845 coastal aeolian sediment transport modeling is related to aeolian sediment availabil-
2846 ity. The approach might be considered too complex for more regular situations where
2847 sediment availability is abundant. A key issue is that assessing whether a coastal
2848 environment is availability-limited or not is not trivial. In this thesis established for-
2849 mulations for equilibrium aeolian sediment transport are used to roughly estimate the
2850 sediment availability of coastal systems. However, if the presented model is proven
2851 to be sufficiently accurate in availability-abundant coastal systems, it might be used
2852 to formulate rules of thumb to assess coastal systems on their sediment availabil-
2853 ity more accurately. Subsequently, the model might be used to assess these coastal
2854 systems that are found to be availability-limited or facilitate the formulation of aggre-
2855 gated relations between aeolian sediment availability and transport that would serve
2856 a more rapid assessment.

2857 In hindsight, the chapters in this thesis reveal a certain chronology in understand-
2858 ing the phenomenon of aeolian sediment availability. Deducing the significance of
2859 sediment availability from the large scale sediment budget analysis or the small scale
2860 sediment transport measurements was not trivial as sediment availability appeared
2861 to be rather intangible. This started with the slightly ambiguous use of terminology
2862 in literature where, for example, *sediment supply* is often mistaken to be equal to *sediment*
2863 *availability* or the *shear velocity threshold*. In addition, various aeolian, marine and
2864 meteorological processes affect aeolian sediment availability and/or the shear veloc-
2865 ity threshold differently and on various temporal and spatial scales. Consequently,
2866 significant time was spent to narrow down the essence of sediment availability and
2867 define a distinctive terminology accordingly. The phenomenon of aeolian sediment
2868 availability was made tangible in a numerical model for aeolian sediment availability
2869 and transport that is unique in that it describes aspects essential to aeolian sediment
2870 availability and transport modeling that have previously been subject to research, but
2871 never been combined in a comprehensive model approach. The main contribution of
2872 the model is the *combined* simulation of:

- 2873 1. Temporal variations in aeolian sediment availability and transport.
- 2874 2. Spatial variations in aeolian sediment availability and transport.
- 2875 3. Recurrence relation between aeolian sediment availability and transport through
2876 self-grading of sediment.
- 2877 4. Simulation of multiple availability-limiting processes and their combined influ-
2878 ence on aeolian sediment transport.
- 2879 5. Natural differentiation between fluid and impact shear velocity threshold (not
2880 implemented).

2881 As illustrated by the Sand Motor hindcast presented in Chapter 5, the combined
2882 influence of various aspects of aeolian sediment availability is essential to obtain reli-
2883 able estimates of aeolian sediment transport and dune growth for which the presented
2884 model provides a general framework. Notwithstanding that model development just
2885 started and needs further extension, calibration and validation to make it generally
2886 applicable.

2887 Based on the Sand Motor hindcast several opportunities for future model improvement
 2888 have been identified:

- 2889 • Support for local variations in wind shear due to morphological feedback.

2890 Neither deposition in front of the dunes nor deposition in the lee of the Sand
 2891 Motor crest is currently simulated as morphological feedback with the wind
 2892 is not taken into account. Given the discrepancy in the spatial distribution of
 2893 aeolian sediment deposits between measurements and model result, it seems
 2894 advisable to provide the model with local variations in wind shear. The model
 2895 of [Kroy et al. \(2002\)](#) based on the derivation of the local wind field by [Weng](#)
 2896 [et al. \(1991\)](#) might provide a description of the local variations in wind shear for
 2897 which the computational effort relates well to the presented model.

- 2898 • Support for the effect of wind gusts.

2899 The calibrated model is forced by an hourly averaged wind time series. The use
 2900 of hourly averaged values for wind speed neglects the gustiness of the wind.
 2901 Wind gusts might influence sediment transport significantly as the relation be-
 2902 tween wind speed and sediment transport is nonlinear. However, providing
 2903 the model with high resolution wind time series would not be beneficial in
 2904 combination with the diffusive implicit numerical scheme. To solve for the ef-
 2905 fect of gustiness an explicit or semi-implicit numerical scheme can be used, but
 2906 such scheme would not be computationally feasible for long-term simulations.
 2907 Moreover, since saltation is not purely an advective mode of transport, the as-
 2908 sumption of advection might be violated for very short time scales as interaction
 2909 with the bed becomes dominant.

2910 As an alternative, the influence of gusts can be parameterized. It can be argued
 2911 that some persistence is needed for gusts to influence sediment transport, re-
 2912 sulting in a lower boundary of the temporal resolution of the wind time series.
 2913 The distribution of the wind speed with respect to the hourly average can then
 2914 provide a basis for a gustiness factor that increases the global wind shear.

- 2915 • Support for differentiation between the fluid and impact shear velocity thresh-
 2916 olds.

2917 The sediment transport capacity is currently implemented identical for the initia-
 2918 tion and continuation of motion as no distinction between the fluid and impact
 2919 threshold is made. The Sand Motor hindcast illustrates how this restriction af-
 2920 fects the influence of roughness elements on aeolian sediment availability. Sim-
 2921 ilar to the implementation of the bed interaction parameter, that distinguishes
 2922 between the grain size distribution in the bed and the air, a distinction between
 2923 fluid and impact threshold can be implemented.

2924 The right-hand side of the advection equation (Equation 4.9) can be modified
 2925 according to:

$$E_k - D_k = \min \left(\frac{\partial m_{a,k}}{\partial t} ; \frac{\hat{w}_k}{T} \cdot [(1 - S_k) \cdot c_{sat,k}^{fluid} + S_k \cdot c_{sat,k}^{impact} - c_k] \right) \quad (6.1)$$

2926 where $c_{\text{sat},k}^{\text{fluid}}$ [kg/m²] and $c_{\text{sat},k}^{\text{fluid}}$ [kg/m²] are the sediment transport capacity associated with the fluid and impact threshold respectively and S_k [-] is the degree of saturation defined as:

$$S_k = \sum_{k=1}^{n_k} \frac{c_k}{c_{\text{sat},k}^{\text{impact}}} \quad (6.2)$$

2929 Note that the weighting factor \hat{w}_k already distinguishes between sediment in
2930 the air and in the bed, depending on the saturation and the bed interaction
2931 parameter and therefore appears outside the brackets.

2932 Although the presented model conceptually allows to differentiate between the
2933 impact and fluid threshold, empirical data to quantify the differentiation is lack-
2934 ing. This model improvement is therefore hypothetical at the current stage of
2935 development.

- 2936 • Support for independent definition of the active bed layer.

2937 The top bed composition layer currently acts as active bed layer, but at the same
2938 time defines the vertical resolution of the sorting and armoring processes. As
2939 these are two fundamentally different properties of the model, it is advisable
2940 to define the active bed layer separate from the numerical resolution. A prob-
2941 ability distribution can be defined that describes the probability of sediment to
2942 be eroded from a specific layer, which would logically decrease with the depth.
2943 The bed composition layer thickness would than uniquely determine the vertical
2944 resolution of sorting and armoring.

- 2945 • Online model coupling

2946 The Sand Motor hindcast showed the importance of an accurate description of
2947 the hydrodynamics for accurate estimates of the development of the aeolian sed-
2948 imentation and erosion volumes. Similarly, groundwater seepage might influ-
2949 ence the aeolian sediment deposition around the lagoon and dune lake, which
2950 would require a description of the groundwater level to be implemented.

2951 It can be questioned if such detailed descriptions of hydrodynamic and hydro-
2952 logical processes are still within the scope of an aeolian sediment transport
2953 model. Alternatively, online model coupling with dedicated models for near-
2954 shore hydrodynamics and hydrology through the Basic Model Interface (BMI)
2955 can be pursued.

7

2956

2957

2958 CONCLUSIONS

2959 This thesis concludes with addressing the research questions formulated in the intro-
2960 ductory chapter (Chapter 1). Each question is addressed with relevant references to
2961 the four main chapters 2 to 5.

2962 **RESEARCH OBJECTIVE #1** Identify the main sources for aeolian sediment in coastal
2963 environments and particularly at the Sand Motor mega nourishment.

2964 The research questions and answers related to objective #1 are:

2965 1.1 What is the total aeolian sediment supply at the Sand Motor mega nour-
2966 ishment?

2967 The total aeolian sediment supply accumulated to 400.000 m³ in the first
2968 four years after construction of the Sand Motor (Section 2.4.2). About
2969 120.000 m³ accumulated in the first half year after construction. From
2970 January 2012 the accumulation rate of aeolian sediment reduced with two-
2971 third to about 80.000 m³/yr.

2972 1.2 What are the main deposition areas of aeolian sediment at the Sand Motor
2973 mega nourishment?

2974 Aeolian sediment in the Sand Motor region is deposited in the dunes (50%),
2975 dune lake (25%) and lagoon (25%, Section 2.4.1). The deposits in the dunes
2976 increased with respect to the dune lake and lagoon over the course of four
2977 years since construction of the Sand Motor. In addition, aeolian sediment
2978 is likely to be deposited offshore as well. The associated sediment volume
2979 is unknown, but estimated by the numerical model as 10% of the measured
2980 deposition volume (Section 5.4).

2981 1.3 What are the main source areas of aeolian sediment at the Sand Motor
2982 mega nourishment?

2983 Aeolian sediment in the Sand Motor region originates from the dry beach
2984 area (aeolian zone, 33%) and the intertidal and low-lying supratidal beach
2985 areas (mixed zones, 67%, Section 2.5). The relative importance of the mixed
2986 zones is notable as it is periodically flooded and the majority of the north-
2987 ern mixed zone is oriented unfavorable with respect to the wind.

2988 1.4 What bed surface characteristics can explain any spatial variations in aeo-
2989 lian sediment supply at the Sand Motor mega nourishment?

2990 Aeolian sediment supply from the Sand Motor's dry beach area (aeolian
2991 zone) is likely to be reduced due to beach armoring. However, beach ar-
2992 moring is probably not the only relevant bed surface characteristic as the
2993 formation of salt crusts has a similar limiting effect on aeolian sediment
2994 supply (Section 2.5.2).

2995 The reduction of aeolian sediment supply from the aeolian zone makes the
2996 intertidal and low-lying supratidal beach areas (mixed zones) relatively
2997 important as supplier of aeolian sediment. The periodic flooding and high
2998 moisture contents are known to limit aeolian sediment supply, but appar-
2999 ently to a lesser extent than beach armoring (Section 2.5.2).

3000 1.5 What is the relevance of these bed surface characteristics for coastal sys-
3001 tems in general?

3002 While high moisture contents are found at any tidal beach, beach armor-
3003 ing is especially relevant to large scale nourishments constructed above
3004 storm surge level. Sand borrowed from the sea bottom and used to widen
3005 or strengthen the coast tends to contain many shells and other roughness
3006 elements. As these elements tend to emerge from the bed due to win-
3007 nowing of fine sediment, beach armoring is an inherent process on such
3008 beaches. In case beach armoring occurs, aeolian sediment supply from
3009 the intertidal and low-lying supratidal beach areas (mixed zones) becomes
3010 more important and consequently also soil moisture content, infiltration
3011 and evaporation rates.

3012 1.6 What characteristics of a coastal system determine aeolian sediment supply
3013 and dune growth?

3014 The intertidal and low-lying supratidal beach areas seem to be a more reli-
3015 able indicator for aeolian sediment supply and dune growth along coasts
3016 with beach armoring than (dry) beach fetch (Section 3.4.2).

3017 **RESEARCH OBJECTIVE #2** Identify the main processes that govern aeolian sediment
3018 availability and supply in coastal environments and particularly at the Sand
3019 Motor mega nourishment.

3020 The research questions and answers related to objective #2 are:

3021 2.1 What bed surface characteristics are related to aeolian sediment supply?

3022 Significant changes in spatial gradients in aeolian sediment transport at
3023 the Sand Motor coincide with the presence of a beach armor layer. This
3024 suggests that beach armoring is a dominant process in the reduction of ae-
3025 olian sediment supply (Section 3.4.3). Spatial gradients in aeolian sediment
3026 transport also seem to be related to topographic features, like the transition
3027 from berm slope to berm flat. Such features seem to promote deposition
3028 of aeolian sediment (negative supply).

3029 2.2 What processes govern the supply of aeolian sediment from the source
3030 areas?

Aeolian sediment supply at the Sand Motor is governed by the development of a beach armor layer (Section 3.5). The reduction of aeolian sediment supply from the dry beach area increases the importance of aeolian sediment supply from the intertidal beach areas. Aeolian sediment supply from the mixed zone is governed by the periodic flooding of the intertidal beach. The timescales involved in the flooding and drying of the intertidal beach seems to be short, resulting in an swift response of the sediment supply to the instantaneous waterline position. Local deposits on the berm flat seem to act as temporary sediment source during high water or high moisture contents resulting in a continuous supply from the intertidal beach (Section 3.5).

2.3 What processes govern the deposition of aeolian sediment in the deposition areas?

Aeolian sediment deposits at the Sand Motor are found in typical areas with either low shear velocities, due to the presence of vegetation (dunes) or morphological feedback with the wind (lee of the Sand Motor crest), or high shear velocity threshold, due to high moisture contents or free water surfaces (dune lake, lagoon and offshore). Local deposits on the berm flat seem to act as temporary sediment source during high water or high moisture contents resulting in a continuous supply from the intertidal beach (Section 3.5). Alongshore variations in sediment deposition seem to be caused by blockage of aeolian sediment transport pathways (Section 2.4.3).

RESEARCH OBJECTIVE #3 Develop a numerical model approach to describe the influence of spatiotemporal variations in aeolian sediment availability on aeolian sediment transport and harmonize existing model approaches to aeolian sediment availability where possible.

The research questions and answers related to objective #3 are:

3.1 What are existing model approaches to describe the influence of aeolian sediment availability on aeolian sediment transport, what are the similarities and differences among them and which approaches are mutually exclusive?

Three approaches can be distinguished in literature: the shear velocity threshold, the critical fetch and the explicit formulation of sediment availability (Section 4.3). All approaches are related, but differ in the amount of spatiotemporal variability in sediment availability they can allow. The approach based on critical fetch is mutually exclusive with the approach based on the explicit formulation of sediment availability as the latter provides the critical fetch as model result. The approach based on an explicit formulation of sediment availability is, in the form presented in this thesis, a spatiotemporal advection framework for the shear velocity threshold that in addition allows for feedback between aeolian sediment availability and transport as well as differentiation between the impact and fluid threshold.

3074 3.2 What processes that were identified to be relevant to aeolian sediment
3075 availability are not covered with sufficient accuracy by existing model ap-
3076 proaches?

3077 Spatiotemporal variations in beach armoring is shown to be a governing
3078 process at the Sand Motor mega nourishment and likely other nourished
3079 beaches. Especially the spatiotemporal variations are not sufficiently accu-
3080 rately described in existing models for aeolian sediment transport (Section
3081 4.2).

3082 3.3 What are the requirements for a model approach that harmonizes existing,
3083 mutual inclusive model approaches and is conceptually able to describe all
3084 processes relevant to aeolian sediment availability and transport?

3085 The approach is based on the legacy of aeolian research, being the abun-
3086 dantly available relations between aeolian sediment availability and trans-
3087 port. It describes feedback between wind and transport as well as sediment
3088 availability and transport (Section 4.3). It distinguishes between the fluid
3089 and impact threshold (Section 6).

3090 **RESEARCH OBJECTIVE #4** Validate the numerical model approach to reproduce the
3091 location and size of sources for aeolian sediment in coastal environments and
3092 particularly at the Sand Motor mega nourishment.

3093 The research questions and answers related to objective #4 are:

3094 4.1 Can the calibrated numerical model reproduce the total aeolian sediment
3095 supply at the Sand Motor mega nourishment with any statistical signifi-
3096 cance?

3097 Yes. The total aeolian sediment supply over the course of 4 years is rep-
3098 resented with an R^2 value of 0.93 and an RMSE of $3 \cdot 10^4 \text{ Mm}^3$ (Section
3099 5.4).

3100 4.2 Can the calibrated numerical model reproduce the main source and depo-
3101 sition areas at the Sand Motor mega nourishment?

3102 Yes. the relative contribution of the intertidal beach was estimated to be
3103 55% based on the large scale sediment budget analysis, which is well rep-
3104 resented by the calibrated model.

3105 4.3 What implemented processes are in retrospect significant to the model re-
3106 sult?

3107 Both the drying of the intertidal beach and sediment sorting and beach
3108 armoring are crucial for the model result. Moreover, both the spatial and
3109 temporal variations affect the model result significantly (Section 5.4).

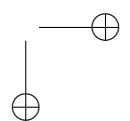
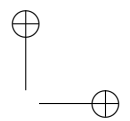
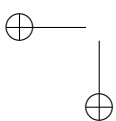
3110

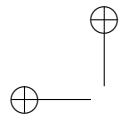
Part IV

3111

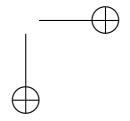
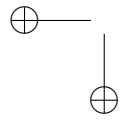
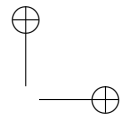
APPENDICES

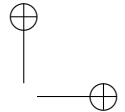
3112





"thesis" — 2016/12/13 — 10:12 — page 106 — #134





A

3113
3114

3115 THEORETICAL SEDIMENT TRANSPORT VOLUMES

3116 The cumulative theoretical sediment transport volume Q [m^3] in the Sand Motor do-
3117 main between September 1, 2011 and September 1, 2015 is estimated from hourly
3118 averaged measured wind speed u_{10} [m/s] and direction θ_u [$^\circ$] measured at 10 m
3119 height by the KNMI meteorological station in Hoek van Holland (Figure 2.2). The
3120 wind time series are used in conjunction with the formulation of [Bagnold \(1937b\)](#) to
3121 obtain the instantaneous theoretical sediment transport rate q [$\text{kg}/\text{m}/\text{s}$] following:

$$q = C \frac{\rho_a}{g} \sqrt{\frac{d_n}{D_n}} (u_* - u_{*th})^3 \quad (\text{A.1})$$

3122 with the shear velocity $u_* = \alpha \cdot u_{10}$ m/s , the shear velocity threshold $u_{*th} = \alpha \cdot 3.87$
3123 m/s , the conversion factor from free-flow wind velocity to shear velocity $\alpha = 0.058$,
3124 the air density $\rho_a = 1.25 \text{ kg}/\text{m}^3$, the particle density $\rho_p = 2650.0 \text{ kg}/\text{m}^3$, the gravita-
3125 tional constant $g = 9.81 \text{ m}/\text{s}^2$, the nominal grain size $d_n = 335 \mu\text{m}$ and a reference
3126 grain size $D_n = 250 \mu\text{m}$.

3127 The cumulative theoretical sediment transport volumes in onshore (Q_{os} [m^3]) and
3128 alongshore (Q_{as} [m^3]) direction are computed by time integration and conversion
3129 from mass to volume following:

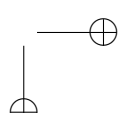
$$\begin{aligned} Q_{os} &= \sum q \cdot \frac{\Delta t \cdot \Delta y}{(1-p) \cdot \rho_p} \cdot f_{\theta_u, os} = 110 \cdot 10^4 \text{ m}^3 \\ Q_{as} &= \sum q \cdot \frac{\Delta t \cdot \Delta x}{(1-p) \cdot \rho_p} \cdot f_{\theta_u, as} = 3 \cdot 10^4 \text{ m}^3 \end{aligned} \quad (\text{A.2})$$

3130 where the temporal resolution $\Delta t = 1 \text{ h}$, the alongshore span of the measurement
3131 domain $\Delta y = 4 \text{ km}$, the approximate lateral beach width $\Delta x = 100 \text{ m}$, the porosity
3132 $p = 0.4$ and $f_{\theta_u, os}$ and $f_{\theta_u, as}$ are factors to account for respectively the onshore and
3133 alongshore wind directions only, defined as:

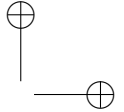
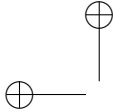
$$\begin{aligned} f_{\theta_u, os} &= \max(0 ; \cos(312^\circ - \theta_u)) \\ f_{\theta_u, as} &= \sin(312^\circ - \theta_u) \end{aligned} \quad (\text{A.3})$$

3134 where θ_u [$^\circ$] is the hourly averaged wind direction and 312° accounts for orientation
3135 of the original coastline.

3136 Note that the difference between the onshore and alongshore cumulative theoretical
3137 sediment transport volumes (Equation A.2) of a factor 40 is determined solely by
3138 the difference between the onshore and alongshore cross-sections of 4 km and 100
3139 m respectively. The sediment transport volumes per meter width in onshore and
3140 alongshore direction are of the same order of magnitude ($275 \text{ m}^3/\text{m}$ and $267 \text{ m}^3/\text{m}$
3141 respectively).



"thesis" — 2016/12/13 — 10:12 — page 108 — #136



B

3142

3143

3144 NUMERICAL IMPLEMENTATION

3145 The numerical implementation of the equations presented in Chapter 4 is explained
 3146 in this appendix. The implementation is available as Python package through the
 3147 OpenEarth GitHub repository at: github.com/openearth/aeolis-python/

3148 **B.1 ADVECTION EQUATION**

3149 The advection equation (Equation 4.6) is implemented in two-dimensional form fol-
 3150 lowing:

$$\frac{\partial c}{\partial t} + u_{z,x} \frac{\partial c}{\partial x} + u_{z,y} \frac{\partial c}{\partial y} = \frac{c_{\text{sat}} - c}{T} \quad (\text{B.1})$$

3151 in which c [kg/m^2] is the sediment mass per unit area in the air, c_{sat} [kg/m^2] is the
 3152 maximum sediment mass in the air that is reached in case of saturation, $u_{z,x}$ and $u_{z,y}$
 3153 are the x- and y-component of the wind velocity at height z [m], T [s] is an adaptation
 3154 time scale, t [s] denotes time and x [m] and y [m] denote cross-shore and alongshore
 3155 distances respectively.

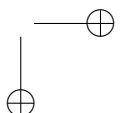
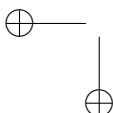
3156 The formulation is discretized following a first order upwind scheme assuming that
 3157 the wind velocity u_z is positive in both x-direction and y-direction:

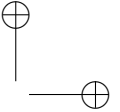
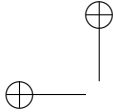
$$\begin{aligned} \frac{c_{i,j,k}^{n+1} - c_{i,j,k}^n}{\Delta t^n} + u_{z,x}^n \frac{c_{i,j,k}^n - c_{i-1,j,k}^n}{\Delta x_{i,j}} + u_{z,y}^n \frac{c_{i,j,k}^n - c_{i,j-1,k}^n}{\Delta y_{i,j}} \\ = \frac{\hat{w}_{i,j,k}^n \cdot c_{\text{sat},i,j,k}^n - c_{i,j,k}^n}{T} \end{aligned} \quad (\text{B.2})$$

3158 in which n is the time step index, i and j are the cross-shore and alongshore spatial
 3159 grid cell indices and k is the grain size fraction index. w [-] is the weighting factor de-
 3160 fined in Equation 4.10a and used for the weighted addition of the saturated sediment
 3161 concentrations over all grain size fractions.

3162 The discretization can be generalized for any wind direction as:

$$\begin{aligned} \frac{c_{i,j,k}^{n+1} - c_{i,j,k}^n}{\Delta t^n} + u_{z,x+}^n c_{i,j,k,x-}^n + u_{z,y+}^n c_{i,j,k,y-}^n \\ + u_{z,x-}^n c_{i,j,k,x+}^n + u_{z,y-}^n c_{i,j,k,y+}^n = \frac{\hat{w}_{i,j,k}^n \cdot c_{\text{sat},i,j,k}^n - c_{i,j,k}^n}{T} \end{aligned} \quad (\text{B.3})$$





3163 in which:

$$\begin{aligned} u_{z,x+}^n &= \max(0, u_{z,x}^n) & ; \quad u_{z,y+}^n &= \max(0, u_{z,y}^n) \\ u_{z,x-}^n &= \min(0, u_{z,x}^n) & ; \quad u_{z,y-}^n &= \min(0, u_{z,y}^n) \end{aligned} \quad (\text{B.4})$$

3164 and

$$\begin{aligned} c_{i,j,k,x+}^n &= \frac{c_{i+1,j,k}^n - c_{i,j,k}^n}{\Delta x} & ; \quad c_{i,j,k,y+}^n &= \frac{c_{i,j+1,k}^n - c_{i,j,k}^n}{\Delta y} \\ c_{i,j,k,x-}^n &= \frac{c_{i,j,k-1}^n - c_{i,j,k}^n}{\Delta x} & ; \quad c_{i,j,k,y-}^n &= \frac{c_{i,j,k}^n - c_{i,j-1,k}^n}{\Delta y} \end{aligned} \quad (\text{B.5})$$

3165 Equation B.3 is explicit in time and adheres to the Courant-Friedrich-Lewis (CFL) condition for numerical stability. Alternatively, the advection equation can be discretized implicitly in time for unconditional stability:

$$\begin{aligned} \frac{c_{i,j,k}^{n+1} - c_{i,j,k}^n}{\Delta t^n} + u_{z,x+}^{n+1} c_{i,j,k,x-}^{n+1} + u_{z,y+}^{n+1} c_{i,j,k,y-}^{n+1} \\ + u_{z,x-}^{n+1} c_{i,j,k,x+}^{n+1} + u_{z,y-}^{n+1} c_{i,j,k,y+}^{n+1} = \frac{\hat{w}_{i,j,k}^{n+1} \cdot c_{\text{sat},i,j,k}^{n+1} - c_{i,j,k}^{n+1}}{\Gamma} \end{aligned} \quad (\text{B.6})$$

3168 Equation B.3 and B.6 can be rewritten as:

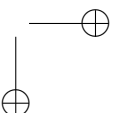
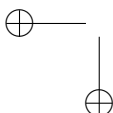
$$\begin{aligned} c_{i,j,k}^{n+1} = c_{i,j,k}^n - \Delta t^n \left[u_{z,x+}^n c_{i,j,k,x-}^n + u_{z,y+}^n c_{i,j,k,y-}^n \right. \\ \left. + u_{z,x-}^n c_{i,j,k,x+}^n + u_{z,y-}^n c_{i,j,k,y+}^n - \frac{\hat{w}_{i,j,k}^n \cdot c_{\text{sat},i,j,k}^n - c_{i,j,k}^n}{\Gamma} \right] \end{aligned} \quad (\text{B.7})$$

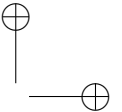
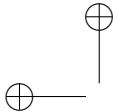
3169 and

$$\begin{aligned} c_{i,j,k}^{n+1} + \Delta t^n \left[u_{z,x+}^{n+1} c_{i,j,k,x-}^{n+1} + u_{z,y+}^{n+1} c_{i,j,k,y-}^{n+1} \right. \\ \left. + u_{z,x-}^{n+1} c_{i,j,k,x+}^{n+1} + u_{z,y-}^{n+1} c_{i,j,k,y+}^{n+1} - \frac{\hat{w}_{i,j,k}^{n+1} \cdot c_{\text{sat},i,j,k}^{n+1} - c_{i,j,k}^{n+1}}{\Gamma} \right] = c_{i,j,k}^n \end{aligned} \quad (\text{B.8})$$

3170 and combined using a weighted average:

$$\begin{aligned} c_{i,j,k}^{n+1} + \Gamma \Delta t^n \left[u_{z,x+}^{n+1} c_{i,j,k,x-}^{n+1} + u_{z,y+}^{n+1} c_{i,j,k,y-}^{n+1} \right. \\ \left. + u_{z,x-}^{n+1} c_{i,j,k,x+}^{n+1} + u_{z,y-}^{n+1} c_{i,j,k,y+}^{n+1} - \frac{\hat{w}_{i,j,k}^{n+1} \cdot c_{\text{sat},i,j,k}^{n+1} - c_{i,j,k}^{n+1}}{\Gamma} \right] \\ = c_{i,j,k}^n - (1 - \Gamma) \Delta t^n \left[u_{z,x+}^n c_{i,j,k,x-}^n + u_{z,y+}^n c_{i,j,k,y-}^n \right. \\ \left. + u_{z,x-}^n c_{i,j,k,x+}^n + u_{z,y-}^n c_{i,j,k,y+}^n - \frac{\hat{w}_{i,j,k}^n \cdot c_{\text{sat},i,j,k}^n - c_{i,j,k}^n}{\Gamma} \right] \end{aligned} \quad (\text{B.9})$$





3171 in which Γ is a weight that ranges from 0 – 1 and determines the implicitness of the
 3172 scheme. The scheme is implicit with $\Gamma = 0$, explicit with $\Gamma = 1$ and semi-implicit
 3173 otherwise. $\Gamma = 0.5$ results in the semi-implicit Crank-Nicolson scheme.

3174 Equation B.5 is back-substituted in Equation B.9:

$$\begin{aligned} c_{i,j,k}^{n+1} + \Gamma \Delta t^n & \left[u_{z,x+}^{n+1} \frac{c_{i,j,k}^{n+1} - c_{i-1,j,k}^{n+1}}{\Delta x} + u_{z,y+}^{n+1} \frac{c_{i,j,k}^{n+1} - c_{i,j-1,k}^{n+1}}{\Delta y} \right. \\ & \left. + u_{z,x-}^{n+1} \frac{c_{i+1,j,k}^{n+1} - c_{i,j,k}^{n+1}}{\Delta x} + u_{z,y-}^{n+1} \frac{c_{i,j+1,k}^{n+1} - c_{i,j,k}^{n+1}}{\Delta y} - \frac{\hat{w}_{i,j,k}^{n+1} \cdot c_{\text{sat},i,j,k}^{n+1} - c_{i,j,k}^{n+1}}{\Gamma} \right] \\ & = c_{i,j,k}^n - (1 - \Gamma) \Delta t^n \left[u_{z,x+}^n \frac{c_{i,j,k}^n - c_{i-1,j,k}^n}{\Delta x} + u_{z,y+}^n \frac{c_{i,j,k}^n - c_{i,j-1,k}^n}{\Delta y} \right. \\ & \left. + u_{z,x-}^n \frac{c_{i+1,j,k}^n - c_{i,j,k}^n}{\Delta x} + u_{z,y-}^n \frac{c_{i,j+1,k}^n - c_{i,j,k}^n}{\Delta y} - \frac{\hat{w}_{i,j,k}^n \cdot c_{\text{sat},i,j,k}^n - c_{i,j,k}^n}{\Gamma} \right] \quad (\text{B.10}) \end{aligned}$$

3175 and rewritten:

$$\begin{aligned} & \left[1 + \Gamma \left(u_{z,x+}^{n+1} \frac{\Delta t^n}{\Delta x} + u_{z,y+}^{n+1} \frac{\Delta t^n}{\Delta y} - u_{z,x-}^{n+1} \frac{\Delta t^n}{\Delta x} - u_{z,y-}^{n+1} \frac{\Delta t^n}{\Delta y} + \frac{\Delta t^n}{\Gamma} \right) \right] c_{i,j,k}^{n+1} \\ & - \Gamma \left(u_{z,x+}^{n+1} \frac{\Delta t^n}{\Delta x} c_{i-1,j,k}^{n+1} + u_{z,y+}^{n+1} \frac{\Delta t^n}{\Delta y} c_{i,j-1,k}^{n+1} - u_{z,x-}^{n+1} \frac{\Delta t^n}{\Delta x} c_{i+1,j,k}^{n+1} - u_{z,y-}^{n+1} \frac{\Delta t^n}{\Delta y} c_{i,j+1,k}^{n+1} \right) \\ & = \left[1 - (1 - \Gamma) \left(u_{z,x+}^n \frac{\Delta t^n}{\Delta x} + u_{z,y+}^n \frac{\Delta t^n}{\Delta y} - u_{z,x-}^n \frac{\Delta t^n}{\Delta x} - u_{z,y-}^n \frac{\Delta t^n}{\Delta y} + \frac{\Delta t^n}{\Gamma} \right) \right] c_{i,j,k}^n \\ & + (1 - \Gamma) \left(u_{z,x+}^n \frac{\Delta t^n}{\Delta x} c_{i-1,j,k}^n + u_{z,y+}^n \frac{\Delta t^n}{\Delta y} c_{i,j-1,k}^n - u_{z,x-}^n \frac{\Delta t^n}{\Delta x} c_{i+1,j,k}^n - u_{z,y-}^n \frac{\Delta t^n}{\Delta y} c_{i,j+1,k}^n \right) \\ & \quad + \Gamma \hat{w}_{i,j,k}^{n+1} \cdot c_{\text{sat},i,j,k}^{n+1} \frac{\Delta t^n}{\Gamma} + (1 - \Gamma) \hat{w}_{i,j,k}^n \cdot c_{\text{sat},i,j,k}^n \frac{\Delta t^n}{\Gamma} \quad (\text{B.11}) \end{aligned}$$

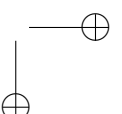
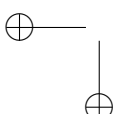
3176 and simplified:

$$a_{i,j}^{0,0} c_{i,j,k}^{n+1} + a_{i,j}^{1,0} c_{i+1,j,k}^{n+1} + a_{i,j}^{0,1} c_{i,j+1,k}^{n+1} - a_{i,j}^{-1,0} c_{i-1,j,k}^{n+1} - a_{i,j}^{0,-1} c_{i,j-1,k}^{n+1} = y_{i,j,k} \quad (\text{B.12})$$

3177 where the implicit coefficients are defined as:

$$\begin{aligned} a_{i,j}^{0,0} &= \left[1 + \Gamma \left(u_{z,x+}^{n+1} \frac{\Delta t^n}{\Delta x} + u_{z,y+}^{n+1} \frac{\Delta t^n}{\Delta y} - u_{z,x-}^{n+1} \frac{\Delta t^n}{\Delta x} - u_{z,y-}^{n+1} \frac{\Delta t^n}{\Delta y} + \frac{\Delta t^n}{\Gamma} \right) \right] \\ a_{i,j}^{1,0} &= \Gamma u_{z,x+}^{n+1} \frac{\Delta t^n}{\Delta x} \\ a_{i,j}^{0,1} &= \Gamma u_{z,y+}^{n+1} \frac{\Delta t^n}{\Delta y} \\ a_{i,j}^{-1,0} &= \Gamma u_{z,x-}^{n+1} \frac{\Delta t^n}{\Delta x} \\ a_{i,j}^{0,-1} &= \Gamma u_{z,y-}^{n+1} \frac{\Delta t^n}{\Delta y} \end{aligned} \quad (\text{B.13})$$

3178 and the explicit right-hand side as:



$$\begin{aligned}
 y_{i,j,k}^n = & \left[1 - (1 - \Gamma) \left(u_{z,x+} \frac{\Delta t^n}{\Delta x} + u_{z,y+} \frac{\Delta t^n}{\Delta y} - u_{z,x-} \frac{\Delta t^n}{\Delta x} - u_{z,y-} \frac{\Delta t^n}{\Delta y} + \frac{\Delta t^n}{\Gamma} \right) \right] c_{i,j,k}^n \\
 & + (1 - \Gamma) \left(u_{z,x+} \frac{\Delta t^n}{\Delta x} c_{i-1,j,k}^n + u_{z,y+} \frac{\Delta t^n}{\Delta y} c_{i,j-1,k}^n - u_{z,x-} \frac{\Delta t^n}{\Delta x} c_{i+1,j,k}^n - u_{z,y-} \frac{\Delta t^n}{\Delta y} c_{i,j+1,k}^n \right) \\
 & + \Gamma \hat{w}_{i,j,k}^{n+1} \cdot c_{\text{sat},i,j,k}^{n+1} \frac{\Delta t^n}{\Gamma} + (1 - \Gamma) \hat{w}_{i,j,k}^n \cdot c_{\text{sat},i,j,k}^n \frac{\Delta t^n}{\Gamma} \quad (\text{B.14})
 \end{aligned}$$

3179 The offshore boundary is defined to be zero-flux, the onshore boundary has a constant
3180 transport gradient and the lateral boundaries are circular:

$$\begin{aligned}
 c_{1,j,k}^{n+1} &= 0 \\
 c_{n_x+1,j,k}^{n+1} &= 2c_{n_x,j,k}^{n+1} - c_{n_x-1,j,k}^{n+1} \\
 c_{i,1,k}^{n+1} &= c_{i,n_y+1,k}^{n+1} \\
 c_{i,n_y+1,k}^{n+1} &= c_{i,1,k}^{n+1}
 \end{aligned} \quad (\text{B.15})$$

3181 These boundary conditions can be combined with Equation B.12, B.13 and B.14 into a
3182 linear system of equations:

$$\left[\begin{array}{cccccc} A_1^0 & A_1^1 & \mathbf{0} & \cdots & \mathbf{0} & A_1^{n_y+1} \\ A_2^{-1} & A_2^0 & \ddots & \ddots & & \mathbf{0} \\ \mathbf{0} & \ddots & \ddots & \ddots & & \vdots \\ \vdots & \ddots & \ddots & \ddots & & \mathbf{0} \\ \mathbf{0} & \ddots & \ddots & & A_{n_y}^0 & A_{n_y}^1 \\ A_{n_y+1}^{-n_y-1} & \mathbf{0} & \cdots & \mathbf{0} & A_{n_y+1}^{-1} & A_{n_y+1}^0 \end{array} \right] \left[\begin{array}{c} \vec{c}_1 \\ \vec{c}_2 \\ \vdots \\ \vdots \\ \vec{c}_{n_y} \\ \vec{c}_{n_y+1} \end{array} \right] = \left[\begin{array}{c} \vec{y}_1 \\ \vec{y}_2 \\ \vdots \\ \vdots \\ \vec{y}_{n_y} \\ \vec{y}_{n_y+1} \end{array} \right] \quad (\text{B.16})$$

3183 where each item in the matrix is again a matrix A_j^l and each item in the vectors is
3184 again a vector \vec{c}_j and \vec{y}_j respectively. The form of the matrix A_j^l depends on the
3185 diagonal index l and reads:

$$A_j^0 = \left[\begin{array}{ccccccc} 0 & 0 & 0 & 0 & \cdots & \cdots & 0 \\ a_{2,j}^{0,-1} & a_{2,j}^{0,0} & a_{2,j}^{0,1} & \ddots & & & \vdots \\ 0 & a_{3,j}^{0,-1} & a_{3,j}^{0,0} & a_{3,j}^{0,1} & \ddots & & \vdots \\ \vdots & \ddots & \ddots & \ddots & \ddots & \ddots & \vdots \\ \vdots & & \ddots & a_{n_x-1,j}^{0,-1} & a_{n_x-1,j}^{0,0} & a_{n_x-1,j}^{0,1} & 0 \\ \vdots & & & 0 & a_{n_x,j}^{0,-1} & a_{n_x,j}^{0,0} & a_{n_x,j}^{0,1} \\ 0 & \cdots & \cdots & 0 & 1 & -2 & 1 \end{array} \right] \quad (\text{B.17})$$

3186 for $l = 0$ and

$$A_j^l = \begin{bmatrix} 1 & 0 & \cdots & \cdots & \cdots & \cdots & 0 \\ 0 & a_{2,j}^{l,0} & \ddots & & & & \vdots \\ \vdots & \ddots & a_{3,j}^{l,0} & \ddots & & & \vdots \\ \vdots & & \ddots & \ddots & \ddots & & \vdots \\ \vdots & & & \ddots & a_{n_x-1,j}^{l,0} & \ddots & \vdots \\ \vdots & & & & \ddots & a_{n_x,j}^{l,0} & 0 \\ 0 & \cdots & \cdots & \cdots & \cdots & 0 & 1 \end{bmatrix} \quad (B.18)$$

for $l \neq 0$. The vectors $\vec{c}_{j,k}$ and $\vec{y}_{j,k}$ read:

$$\vec{c}_{j,k} = \begin{bmatrix} c_{1,j,k}^{n+1} \\ c_{2,j,k}^{n+1} \\ c_{3,j,k}^{n+1} \\ \vdots \\ c_{n_x-1,j,k}^{n+1} \\ c_{n_x,j,k}^{n+1} \\ c_{n_x+1,j,k}^{n+1} \end{bmatrix} \quad \text{and} \quad \vec{y}_{j,k} = \begin{bmatrix} 0 \\ y_{2,j,k}^n \\ y_{3,j,k}^n \\ \vdots \\ y_{n_x-1,j,k}^n \\ y_{n_x,j,k}^n \\ 0 \end{bmatrix} \quad (B.19)$$

n_x and n_y denote the number of spatial grid cells in x- and y-direction.

3189 B.2 IMPLICIT SOLVER

3190 The linear system defined in Equation B.16 is solved by a sparse matrix solver for each
 3191 sediment fraction separately in ascending order of grain size. Initially, the weights
 3192 $\hat{w}_{i,j,k}^{n+1}$ are chosen according to the grain size distribution in the bed and the air fol-
 3193 lowing Equation 4.10b. The sediment availability constraint based on Equation 4.9 is
 3194 checked after each solve:

$$m_{a,k} \geq \frac{\hat{w}_{i,j,k}^{n+1} c_{sat,i,j,k}^{n+1} - c_{i,j,k}^{n+1}}{\Delta t^n} \quad (B.20)$$

3195 If the constraint is violated, a new estimate for the weights is back-calculated follow-
 3196 ing:

$$\hat{w}_{i,j,k}^{n+1} = \frac{c_{i,j,k}^{n+1} + m_{a,k} \frac{\Delta t^n}{\Gamma}}{c_{sat,i,j,k}^{n+1}} \quad (B.21)$$

3197 The system is solved again using the new weights. This procedure is repeated until
 3198 a weight is found that does not violate the sediment availability constraint. If the
 3199 time step is not too large, the procedure typically converges in only a few iterations.
 3200 Finally, the weights of the larger grains are increased proportionally as to ensure that
 3201 the sum of all weights remains unity. If no larger grains are defined, not enough
 3202 sediment is available for transport and the grid cell is truly availability-limited. This

3203 situation should only occur occasionally as the weights in the next time step are com-
 3204 puted based on the new bed composition and thus will be skewed towards the large
 3205 fractions. If the situation occurs regularly, the time step is chosen too large compared
 3206 to the rate of armoring.

3207 **B.3 SHEAR VELOCITY THRESHOLD**

3208 The shear velocity threshold represents the influence of bed surface properties in the
 3209 saturated sediment transport equation (Equation 4.8). The shear velocity threshold
 3210 is computed for each grid cell and sediment fraction separately based on local bed
 3211 surface properties, like moisture, roughness elements and salt content. For each bed
 3212 surface property supported by the model a factor is computed to increase the initial
 3213 shear velocity threshold:

$$u_{*th} = f_{u_{*th},M} \cdot f_{u_{*th},R} \cdot f_{u_{*th},S} \cdot u_{*th,o} \quad (\text{B.22})$$

3214 The initial shear velocity threshold $u_{*th,o}$ [m/s] is computed based on the grain size
 3215 following [Bagnold \(1937a\)](#):

$$u_{*th,o} = A \sqrt{\frac{\rho_p - \rho_a}{\rho_a} \cdot g \cdot d_n} \quad (\text{B.23})$$

3216 where A [-] is an empirical constant, ρ_p [kg/m³] is the grain density, ρ_a [kg/m³] is the
 3217 air density, g [m/s²] is the gravitational constant and d_n [m] is the nominal grain size
 3218 of the sediment fraction.

3219 **B.3.1 Moisture content**

3220 The shear velocity threshold is updated based on moisture content following [Belly](#)
 3221 ([1964](#)):

$$f_{u_{*th},M} = \max(1 ; 1.8 + 0.6 \cdot \log(p_g)) \quad (\text{B.24})$$

3222 where $f_{u_{*th},M}$ [-] is a factor in Equation B.22, p_g [-] is the geotechnical mass content of
 3223 water, which is the percentage of water compared to the dry mass. The geotechnical
 3224 mass content relates to the volumetric water content p_V [-] according to:

$$p_g = \frac{p_V \cdot \rho_w}{\rho_p \cdot (1 - p)} \quad (\text{B.25})$$

3225 where ρ_w [kg/m³] and ρ_p [kg/m³] are the water and particle density respectively and
 3226 p [-] is the porosity. Values for p_g smaller than 0.005 do not affect the shear velocity
 3227 threshold ([Pye and Tsoar, 1990](#)). Values larger than 0.064 (or 10% volumetric content)
 3228 cease transport ([Delgado-Fernandez, 2010](#)), which is implemented as an infinite shear
 3229 velocity threshold.

3230 Exploratory model runs of the unsaturated soil with the HYDRUS1D ([Šimůnek](#)
 3231 [et al., 1998](#)) hydrology model show that the increase of the volumetric water content
 3232 to saturation is almost instantaneous with rising tide. The drying of the beach surface
 3233 through infiltration shows an exponential decay. In order to capture this behavior the
 3234 volumetric water content is implemented according to:

$$p_V^{n+1} = \begin{cases} p & \text{if } \eta > z_b \\ p_V^n \cdot e^{\frac{\log(0.5)}{T_{dry}} \cdot \Delta t^n} - E_v \cdot \frac{\Delta t^n}{\Delta z} & \text{if } \eta \leq z_b \end{cases} \quad (\text{B.26})$$

where η [m+MSL] is the instantaneous water level, z_b [m+MSL] is the local bed elevation, p_V^n [-] is the volumetric water content in time step n , Δt^n [s] is the model time step and Δz is the bed composition layer thickness. T_{dry} [s] is the beach drying time scale, defined as the time in which the beach moisture content halves. E_v [m/s] is the evaporation rate that is implemented through an adapted version of the Penman equation (Shuttleworth, 1993):

$$E_v = \frac{m_v \cdot R_n + 6.43 \cdot \gamma_v \cdot (1 + 0.536 \cdot u_2) \cdot \delta e}{\lambda_v \cdot (m_v + \gamma_v)} \cdot 9 \cdot 10^7 \quad (\text{B.27})$$

where m_v [kPa/K] is the slope of the saturation vapor pressure curve, R_n [MJ/m²/day] is the net radiance, γ_v [kPa/K] is the psychrometric constant, u_2 [m/s] is the wind speed at 2 m above the bed, δe [kPa] is the vapor pressure deficit (related to the relative humidity) and λ_v [MJ/kg] is the latent heat vaporization. To obtain an evaporation rate in [m/s], the original formulation is multiplied by $9 \cdot 10^7$.

3246 B.3.2 Roughness elements

3247 The shear velocity threshold is updated based on the presence of roughness elements
3248 following Raupach et al. (1993):

$$f_{u_{*th,R}} = \sqrt{(1 - m \cdot \sum_{k=k_0}^{n_k} \hat{w}_k^{\text{bed}})(1 + \frac{m\beta}{\sigma} \cdot \sum_{k=k_0}^{n_k} \hat{w}_k^{\text{bed}})} \quad (\text{B.28})$$

3249 by assuming:

$$\lambda = \frac{\sum_{k=k_0}^{n_k} \hat{w}_k^{\text{bed}}}{\sigma} \quad (\text{B.29})$$

3250 where $f_{u_{*th,R}}$ [-] is a factor in Equation B.22, k_0 is the sediment fraction index of the
3251 smallest non-erodible fraction in current conditions and n_k is the number of sediment
3252 fractions defined. The implementation is discussed in detail in section 4.4.4.

3253 B.3.3 Salt content

3254 The shear velocity threshold is updated based on salt content following Nickling and
3255 Ecclestone (1981):

$$f_{u_{*th,S}} = 1.03 \cdot \exp(0.1027 \cdot p_s) \quad (\text{B.30})$$

3256 where $f_{u_{*th,S}}$ [-] is a factor in Equation B.22 and p_s [-] is the salt content [mg/g].
3257 Currently, no model is implemented that predicts the instantaneous salt content. The
3258 spatial varying salt content needs to be specified by the user, for example through the
3259 BMI interface.

3260 B.3.4 Masks

3261 To account for spatial differences in hydrodynamics without the necessity to run a sep-
 3262 arate hydrodynamic model, the model supports hydrodynamic masks. Without such
 3263 mask the model imposes the still water levels and offshore wave heights uniformly
 3264 to all grid cells where the bed level is below the instantaneous water level. The tidal
 3265 range and mean water level are therefore uniform throughout the model domain. In
 3266 addition, the still water level underestimates the local water level as wave runup is
 3267 not taken into account. Only wave heights are maximized by a constant and uniform
 3268 ratio between wave height and water depth (Equation 4.15).

3269 For cases where the assumption of uniform hydrodynamics hydrodynamics, the
 3270 uniformly imposed instantaneous still water level η [m+MSL] and offshore wave
 3271 height H [m] can be converted to a local water level $\hat{\eta}$ [m+MSL] and wave height
 3272 \hat{H} [m] using a hydrodynamic mask, following:

$$\begin{aligned}\hat{H} &= H \cdot K^x \\ \hat{\eta} &= \eta \cdot K^x + K^+ + R\end{aligned}\quad (\text{B.31})$$

3273 where K is the hydrodynamic mask, consisting of a multiplication mask (K^x [-]) and
 3274 an addition mask (K^+ [m]). The multiplication mask can be used to reduce the tidal
 3275 range and the addition mask can subsequently be used to elevate the mean water
 3276 level. The hydrodynamic mask is applied before the wave height is maximized by the
 3277 maximum ratio between wave height and water depth (Equation 4.15). R [m] is an
 3278 estimate for the wave runup height following Battjes (1974):

$$\frac{R}{H} = \xi \quad (\text{B.32})$$

3279 where ξ [-] is the surf similarity parameter with a value between 1.0 and 2.3.

3280 B.4 BASIC MODEL INTERFACE (BMI)

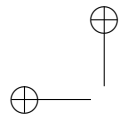
3281 A Basic Model Interface (BMI, Peckham et al., 2013) is implemented that allows inter-
 3282 action with the model during run time. The model can be implemented as a library
 3283 within a larger framework as the interface exposes the initialization, finalization and
 3284 time stepping routines. As a convenience functionality the current implementation
 3285 supports the specification of a callback function. The callback function is called at the
 3286 start of each time step and can be used to exchange data with the model, e.g. update
 3287 the topography from measurements.

3288 An example of a callback function, that is referenced in the model input file or
 3289 through the model command-line options as "callback.py:update", is:

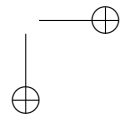
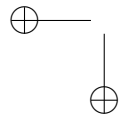
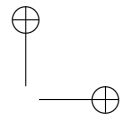
callback.py

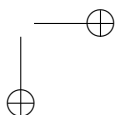
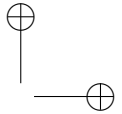
```
3290
3291 import numpy as np
3292
3293 def update(model):
3294     val = model.get_var('zb')
3295     val_new = val.copy()
3296     val_new[:, :] = np.loadtxt('measured_topography.txt')
```

329 | model.set_var('zb', val_new)



"thesis" — 2016/12/13 — 10:12 — page 118 — #146





C

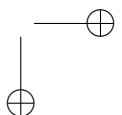
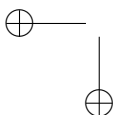
3299

3300

3301 MODEL SETTINGS

3302 Unless stated otherwise, the model schematizations presented in chapter 5 used the
3303 settings listed below. Some model settings belong to experimental features of the
3304 model and are not discussed in this thesis. These settings are listed for complete-
3305 ness only and marked with an asterisk (*). The model settings are chosen such that
3306 experimental features are disabled.

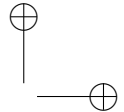
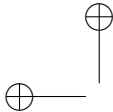
Parameter	Value
A	0.085
CFL	1.0
Cb	1.5
T	1.0
Tdry	5400.0
Tsalt*	0.0
accfac	1.0
bedupdate	False
beta	130.0
bi	0.05
boundary_lateral	circular
boundary_offshore	noflux
boundary_onshore	gradient
callback	None
cpair	0.0010035
csalt*	0.035
dt	3600.0
eps	0.001
evaporation	True
facDOD	0.1
g	9.81
gamma	0.5
grain_dist	0.005709 0.234708 0.608887 0.099666 0.001029 0.000001 0.010486 0.028503 0.010486 0.000522 0.000004
grain_size	0.000177 0.000250 0.000354 0.000500 0.000707 0.001000 0.002000 0.004000 0.008000 0.016000 0.032000
k	0.01
layer_thickness	0.01
m	0.5



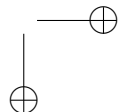
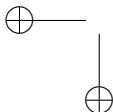
Parameter	Value	(continued)
max_error	0.000001	
max_iter	1000	
method_moist	belly_johnson	
method_transport	bagnold	
mixtoplayer	True	
nfractions	11	
nlayers	10	
output_times	604800.0	
porosity	0.4	
restart	None	
rhoa	1.25	
rhop	2650.0	
rhow	1025.0	
runup	False	
scheme	euler_backward	
sigma	11.9	
th_bedslope	False	
th_grainsize	True	
th_humidity*	False	
th_moisture	True	
th_roughness	True	
th_salt*	False	
tstart	0.0	
tstop	126230400.0	
z	10.0	

3307 BIBLIOGRAPHY

- 3308 Aagaard, T. (2014). Sediment supply to beaches: Cross-shore sand trans-
3309 port on the lower shoreface. *Journal of Geophysical Research*, 119(4):913–926.
3310 doi:[10.1002/2013JF003041](https://doi.org/10.1002/2013JF003041). 2013JF003041.
- 3311 Aagaard, T., Davidson-Arnott, R., Greenwood, B., and Nielsen, J. (2004). Sed-
3312 iment supply from shoreface to dunes: linking sediment transport measure-
3313 ments and long-term morphological evolution. *Geomorphology*, 60(1):205–224.
3314 doi:[10.1016/j.geomorph.2003.08.002](https://doi.org/10.1016/j.geomorph.2003.08.002).
- 3315 Anthony, E. J. (2013). Storms, shoreface morphodynamics, sand supply, and the accre-
3316 tion and erosion of coastal dune barriers in the southern north sea. *Geomorphology*,
3317 199:8–21. doi:[10.1016/j.geomorph.2012.06.007](https://doi.org/10.1016/j.geomorph.2012.06.007).
- 3318 Arens, S., Baas, A., Van Boxel, J., and Kalkman, C. (2001). Influence of reed stem
3319 density on foredune development. *Earth Surface Processes and Landforms*, 26(11):1161–
3320 1176.
- 3321 Arens, S., Van Boxel, J., and Abuodha, J. (2002). Changes in grain size of sand in
3322 transport over a foredune. *Earth Surface Processes and Landforms*, 27(11):1163–1175.
- 3323 Arens, S. M. (1996). Patterns of sand transport on vegetated foredunes. *Geomorphology*,
3324 17:339–350.
- 3325 Bagnold, R. (1935). The movement of desert sand. *Geographical Journal*, pages 342–365.
- 3326 Bagnold, R. (1937a). The size-grading of sand by wind. *Proceedings of the Royal Society
3327 of London. Series A, Mathematical and Physical Sciences*, pages 250–264.
- 3328 Bagnold, R. (1937b). The transport of sand by wind. *Geographical journal*, pages 409–
3329 438.
- 3330 Barchyn, T. E., Hugenholtz, C. H., Li, B., McKenna Neuman, C., and Sanderson,
3331 S. (2014a). From particle counts to flux: Wind tunnel testing and calibration
3332 of the "wenglor" aeolian sediment transport sensor. *Aeolian Research*, 15:311–318.
3333 doi:[10.1016/j.aeolia.2014.06.009](https://doi.org/10.1016/j.aeolia.2014.06.009).
- 3334 Barchyn, T. E., Martin, R. L., Kok, J. F., and Hugenholtz, C. H. (2014b). Funda-
3335 mental mismatches between measurements and models in aeolian sediment trans-
3336 port prediction: The role of small-scale variability. *Aeolian Research*, 15:245–251.
3337 doi:[10.1016/j.aeolia.2014.07.002](https://doi.org/10.1016/j.aeolia.2014.07.002).
- 3338 Battjes, J. A. (1974). *Computation of set-up, longshore currents, run-up and overtopping due
3339 to wind-generated waves*. PhD thesis, TU Delft, Delft University of Technology.
- 3340 Bauer, B. O. and Davidson-Arnott, R. G. D. (2002). A general framework for modeling
3341 sediment supply to coastal dunes including wind angle, beach geometry, and fetch
3342 effects. *Geomorphology*, 49:89–108. doi:[10.1016/S0169-555X\(02\)00165-4](https://doi.org/10.1016/S0169-555X(02)00165-4).



- 3343 Bauer, B. O., Davidson-Arnott, R. G. D., Hesp, P. A., Namikas, S. L., Oller-
3344 head, J., and Walker, I. J. (2009). Aeolian sediment transport on a beach: Sur-
3345 face moisture, wind fetch, and mean transport. *Geomorphology*, 105:106–116.
3346 doi:[10.1016/j.geomorph.2008.02.016](https://doi.org/10.1016/j.geomorph.2008.02.016).
- 3347 Belly, P. Y. (1964). Sand movement by wind. Technical Report 1, U.S. Army Corps of
3348 Engineers CERC, Vicksburg, MS. 38 pp.
- 3349 Borsje, B. W., van Wesenbeeck, B. K., Dekker, F., Paalvast, P., Bouma, T. J., van Katwijk,
3350 M. M., and de Vries, M. B. (2011). How ecological engineering can serve in coastal
3351 protection. *Ecological Engineering*, 37(2):113–122. doi:[10.1016/j.ecoleng.2010.11.027](https://doi.org/10.1016/j.ecoleng.2010.11.027).
- 3352 Buscombe, D., Rubin, D. M., and Warrick, J. A. (2010). A universal approximation
3353 of grain size from images of noncohesive sediment. *Journal of Geophysical Research*,
3354 115(F2). doi:[10.1029/2009JF001477](https://doi.org/10.1029/2009JF001477). F02015.
- 3355 Cheng, H., Liu, C., Zou, X., Li, J., He, J., Liu, B., Wu, Y., Kang, L., and Fang, Y. (2015).
3356 Aeolian creeping mass of different grain sizes over sand beds of varying length.
3357 *Journal of Geophysical Research*. doi:[10.1002/2014JF003367](https://doi.org/10.1002/2014JF003367). 2014JF003367.
- 3358 Darke, I. and McKenna Neuman, C. (2008). Field study of beach water content
3359 as a guide to wind erosion potential. *Journal of Coastal Research*, 24(5):1200–1208.
3360 doi:[10.2112/00-000.1](https://doi.org/10.2112/00-000.1).
- 3361 Davidson-Arnott, R. G. and Law, M. N. (1990). *Seasonal patterns and controls on sediment
3362 supply to coastal foredunes, Long Point, Lake Erie*, pages 177–200. Wiley Chichester.
- 3363 Davidson-Arnott, R. G., White, D. C., and Ollerhead, J. (1997). The effects of artificial
3364 pebble concentrations on eolian sand transport on a beach. *Canadian Journal of Earth
3365 Sciences*, 34(11):1499–1508.
- 3366 Davidson-Arnott, R. G. D. and Bauer, B. O. (2009). Aeolian sediment transport on
3367 a beach: Thresholds, intermittency, and high frequency variability. *Geomorphology*,
3368 105:117–126. doi:[10.1016/j.geomorph.2008.02.018](https://doi.org/10.1016/j.geomorph.2008.02.018).
- 3369 Davidson-Arnott, R. G. D., MacQuarrie, K., and Aagaard, T. (2005). The effect of wind
3370 gusts, moisture content and fetch length on sand transport on a beach. *Geomorphol-
3371 ogy*, 68:115–129. doi:[10.1016/j.geomorph.2004.04.008](https://doi.org/10.1016/j.geomorph.2004.04.008).
- 3372 Davidson-Arnott, R. G. D., Yang, Y., Ollerhead, J., Hesp, P. A., and Walker, I. J.
3373 (2008). The effects of surface moisture on aeolian sediment transport thresh-
3374 old and mass flux on a beach. *Earth Surface Processes and Landforms*, 33(1):55–74.
3375 doi:[10.1002/esp.1527](https://doi.org/10.1002/esp.1527).
- 3376 De Schipper, M., De Vries, S., Ranasinghe, R., Reniers, A., and Stive, M. (2013). Along-
3377 shore topographic variability at a nourished beach. In *Coastal Dynamics 2013: 7th
3378 International Conference on Coastal Dynamics, Arcachon, France, 24–28 June 2013*. Bor-
3379 deaux University.



- 3380 de Schipper, M. A., de Vries, S., Ruessink, G., de Zeeuw, R. C., Rutten, J., van
3381 Gelder-Maas, C., and Stive, M. J. (2016). Initial spreading of a mega feeder nourish-
3382 ment: Observations of the sand engine pilot project. *Coastal Engineering*, 111:23–38.
3383 doi:[10.1016/j.coastaleng.2015.10.011](https://doi.org/10.1016/j.coastaleng.2015.10.011).
- 3384 de Vriend, H. J., van Koningsveld, M., Aarninkhof, S. G., de Vries, M. B., and Bap-
3385 tist, M. J. (2015). Sustainable hydraulic engineering through building with nature.
3386 *Journal of Hydro-environment Research*, 9(2):159–171. doi:[10.1016/j.jher.2014.06.004](https://doi.org/10.1016/j.jher.2014.06.004).
- 3387 de Vries, S., Arens, S. M., de Schipper, M. A., and Ranasinghe, R. (2014a). Aeolian
3388 sediment transport on a beach with a varying sediment supply. *Aeolian Research*,
3389 15:235–244. doi:[10.1016/j.aeolia.2014.08.001](https://doi.org/10.1016/j.aeolia.2014.08.001).
- 3390 de Vries, S., Radermacher, M., de Schipper, M., and Stive, M. (2015). Tidal dynamics
3391 in the sand motor lagoon. In *E-proceedings of the 36th IAHR World Congress*.
- 3392 de Vries, S., van Thiel de Vries, J. S. M., van Rijn, L. C., Arens, S. M., and Ranasinghe,
3393 R. (2014b). Aeolian sediment transport in supply limited situations. *Aeolian Research*,
3394 12:75–85. doi:[10.1016/j.aeolia.2013.11.005](https://doi.org/10.1016/j.aeolia.2013.11.005).
- 3395 Delft3D-FLOW Manual (2014). *Delft3D - 3D/2D modelling suite for integral water solu-*
3396 *tions - Hydro-Morphodynamics*. Deltares, Delft. Version 3.15.34158.
- 3397 Delgado-Fernandez, I. (2010). A review of the application of the fetch ef-
3398 fect to modelling sand supply to coastal foredunes. *Aeolian Research*, 2:61–70.
3399 doi:[10.1016/j.aeolia.2010.04.001](https://doi.org/10.1016/j.aeolia.2010.04.001).
- 3400 Delgado-Fernandez, I., Davidson-Arnott, R., Bauer, B. O., Walker, I. J., Ollerhead,
3401 J., and Rhew, H. (2012). Assessing aeolian beach-surface dynamics using a re-
3402 mote sensing approach. *Earth Surface Processes and Landforms*, 37(15):1651–1660.
3403 doi:[10.1002/esp.3301](https://doi.org/10.1002/esp.3301).
- 3404 Delgado-Fernandez, I. and Davidson-Arnott, R. A. (2011). Meso-scale aeolian sedi-
3405 ment input to coastal dunes: The nature of aeolian transport events. *Geomorphology*,
3406 126(1):217–232. doi:[10.1016/j.geomorph.2010.11.005](https://doi.org/10.1016/j.geomorph.2010.11.005).
- 3407 Donchyts, G., Baart, F., Winsemius, H., Gorelick, N., Kwadijk, J., and van de Giesen, N.
3408 (2016). Earth's surface water change over the past 30 years. *Nature Climate Change*,
3409 6(9):810–813. doi:[10.1038/nclimate3111](https://doi.org/10.1038/nclimate3111).
- 3410 Dong, Z., Wang, H., Liu, X., and Wang, X. (2004a). The blown sand flux over a sandy
3411 surface: a wind tunnel investigation on the fetch effect. *Geomorphology*, 57:117–127.
3412 doi:[10.1016/S0169-555X\(03\)00087-4](https://doi.org/10.1016/S0169-555X(03)00087-4).
- 3413 Dong, Z., Wang, H., Liu, X., and Wang, X. (2004b). A wind tunnel investiga-
3414 tion of the influences of fetch length on the flux profile of a sand cloud blow-
3415 ing over a gravel surface. *Earth Surface Processes and Landforms*, 29(13):1613–1626.
3416 doi:[10.1002/esp.1116](https://doi.org/10.1002/esp.1116).
- 3417 Dupont, S., Bergametti, G., and Simoëns, S. (2014). Modeling aeolian ero-
3418 sion in presence of vegetation. *Journal of Geophysical Research*, 119(2):168–187.
3419 doi:[10.1002/2013JF002875](https://doi.org/10.1002/2013JF002875).

- 3420 Dyer, K. R. (1986). *Coastal and estuarine sediment dynamics*. Wiley, Chichester.
- 3421 Dymin (1954). quoted by Greeley and Iversen (1985).
- 3422 Edwards, B. L. and Namikas, S. L. (2009). Small-scale variability in surface moisture
3423 on a fine-grained beach: implications for modeling aeolian transport. *Earth Surface
3424 Processes and Landforms*, 34:1333–1338. doi:[10.1002/esp.1817](https://doi.org/10.1002/esp.1817).
- 3425 Edwards, B. L., Namikas, S. L., and D'Sa, E. J. (2013). Simple infrared techniques for
3426 measuring beach surface moisture. *Earth Surface Processes and Landforms*, 38(2):192–
3427 197. doi:[10.1002/esp.3319](https://doi.org/10.1002/esp.3319).
- 3428 Gallagher, E. L., MacMahan, J., Reniers, A., Brown, J., and Thornton, E. B. (2011).
3429 Grain size variability on a rip-channelled beach. *Marine Geology*, 287(1):43–53.
3430 doi:[10.1016/j.margeo.2011.06.010](https://doi.org/10.1016/j.margeo.2011.06.010).
- 3431 Gillette, D. A. and Stockton, P. H. (1989). The effect of nonerodible particles on
3432 wind erosion of erodible surfaces. *Journal of Geophysical Research: Atmospheres*,
3433 94(D10):12885–12893. doi:[10.1029/JD094iD10p12885](https://doi.org/10.1029/JD094iD10p12885).
- 3434 Gillies, J. A., Nickling, W. G., and King, J. (2006). Aeolian sediment transport through
3435 large patches of roughness in the atmospheric inertial sublayer. *Journal of Geophysical
3436 Research: Earth Surface*, 111(F2). doi:[10.1029/2005JF000434](https://doi.org/10.1029/2005JF000434). F02006.
- 3437 Grunnet, N. M. and Ruessink, B. (2005). Morphodynamic response of
3438 nearshore bars to a shoreface nourishment. *Coastal Engineering*, 52(2):119–137.
3439 doi:[10.1016/j.coastaleng.2004.09.006](https://doi.org/10.1016/j.coastaleng.2004.09.006).
- 3440 Hamm, L., Capobianco, M., Dette, H., Lechuga, A., Spanhoff, R., and Stive, M. (2002).
3441 A summary of european experience with shore nourishment. *Coastal engineering*,
3442 47(2):237–264. doi:[10.1016/S0378-3839\(02\)00127-8](https://doi.org/10.1016/S0378-3839(02)00127-8).
- 3443 Hesp, P. A. and Smyth, T. A. G. (2016). Surfzone-beach-dune interactions: Flow and
3444 sediment transport across the intertidal beach and backshore. *Journal of Coastal
3445 Research*, SI 75:8–12. doi:[10.2112/SI75-002.1](https://doi.org/10.2112/SI75-002.1).
- 3446 Hoonhout, B. M. (2013). Monitoring the process of aeolian transport. In *Proceedings of
3447 the NCK-days 2013*.
- 3448 Hoonhout, B. M. (2016a). Aeolis model setups v2.0. GIT repository.
3449 doi:[10.5281/zenodo.58837](https://doi.org/10.5281/zenodo.58837).
- 3450 Hoonhout, B. M. (2016b). Aeolis v1.1: A process-based model for sim-
3451 ulating availability-limited aeolian sediment transport. GIT repository.
3452 doi:[10.5281/zenodo.58854](https://doi.org/10.5281/zenodo.58854).
- 3453 Hoonhout, B. M., Baart, F., and Van Thiel de Vries, J. S. M. (2014a). Intertidal beach
3454 classification in infrared images. *Journal of Coastal Research*, SI 66:657–662.
- 3455 Hoonhout, B. M., Cohn, N., de Vries, S., Roelvink, J. A., Ruggiero, P., Moore, L. J.,
3456 Durán, O., and Goldstein, E. (2016a). How tides and waves enhance aeolian sedi-
3457 ment transport at the sand motor. In *Proceedings of the 35th International Conference
3458 on Coastal Engineering*.

- 3459 Hoonhout, B. M., Cohn, N., de Vries, S., Roelvink, J. A., Ruggiero, P., Moore, L. J.,
3460 Durán, O., and Goldstein, E. (2016b). How tides and waves enhance aeolian sedi-
3461 ment transport at the sand motor. In *Proceedings of the Ocean Sciences Meeting 2016*.
- 3462 Hoonhout, B. M. and de Vries, S. (2014a). Modelling and monitoring of meso-scale
3463 supply-limited aeolian transport. In *Proceedings of the NCK-days 2014*.
- 3464 Hoonhout, B. M. and de Vries, S. (2014b). Process-based modeling of supply-limited
3465 aeolian transport in coastal environments. In *Proceedings of the International Confer-
3466 ence on Aeolian Research 2014*.
- 3467 Hoonhout, B. M. and de Vries, S. (2016a). Aeolian sediment supply at a mega nour-
3468 ishment. *Coastal Engineering*. Submitted.
- 3469 Hoonhout, B. M. and de Vries, S. (2016b). Aeolis: A new model for aeolian sediment
3470 supply and transport. In *Proceedings of the NCK-days 2016*.
- 3471 Hoonhout, B. M. and de Vries, S. (2016c). Field measurements on spatial variations in
3472 aeolian sediment availability at the sand motor mega nourishment. *Aeolian Research*.
3473 Submitted.
- 3474 Hoonhout, B. M. and de Vries, S. (2016d). A process-based model for aeolian sediment
3475 transport and spatiotemporal varying sediment availability. *Journal of Geophysical
3476 Research: Earth Surface*. doi:[10.1002/2015JF003692](https://doi.org/10.1002/2015JF003692). 2015JF003692.
- 3477 Hoonhout, B. M., de Vries, S., Baart, F., van Thiel de Vries, J. S. M., van der Weerd,
3478 L., and Wijnberg, K. M. (2013). Monitoring of beach surface properties with remote
3479 sensing. In *Proceedings of Coastal Dynamics*, Arcachon, France.
- 3480 Hoonhout, B. M., de Vries, S., and Cohn, N. (2015a). The influence of spatially varying
3481 supply on coastal aeolian transport: a field experiment. In *Proceedings of Coastal
3482 Sediments*, San Diego, USA.
- 3483 Hoonhout, B. M., de Vries, S., and Cohn, N. (2015b). The influence of spatially varying
3484 supply on coastal aeolian transport: A field experiment. In *Proceedings of the NCK-
3485 days 2015*.
- 3486 Hoonhout, B. M., de Vries, S., and Cohn, N. (2016c). Field measurements on aeo-
3487 lian sediment transport at the sand motor mega nourishment during the megapex
3488 field campaign. OpenDAP server. doi:[10.4121/uuid:3bc3591b-9d9e-4600-8705-
3489 5b7eba6aa3ed](https://doi.org/10.4121/uuid:3bc3591b-9d9e-4600-8705-5b7eba6aa3ed).
- 3490 Hoonhout, B. M. and den Heijer, C. (2010). Reliability of dune erosion assessment
3491 along curved coastlines. In *Proceedings of the 32nd International Conference on Coastal
3492 Engineering*, Shanghai, China.
- 3493 Hoonhout, B. M. and Radermacher, M. (2015a). Annotated images of the dutch coast.
3494 FTP server. doi:[10.4121/uuid:08400507-4731-4cb2-a7ec-9ed2937db119](https://doi.org/10.4121/uuid:08400507-4731-4cb2-a7ec-9ed2937db119).
- 3495 Hoonhout, B. M. and Radermacher, M. (2015b). Flamingo: a coastal image analysis
3496 toolbox. GIT repository. doi:[10.5281/zenodo.14596](https://doi.org/10.5281/zenodo.14596).

- 3497 Hoonhout, B. M., Radermacher, M., Baart, F., and Van der Maaten, L. J. P. (2015c). An
3498 automated method for semantic classification of regions in coastal images. *Coastal*
3499 *Engineering*, 105:1–12. doi:[10.1016/j.coastaleng.2015.07.010](https://doi.org/10.1016/j.coastaleng.2015.07.010).
- 3500 Hoonhout, B. M. and van Thiel de Vries, J. S. M. (2012). Modeling dune erosion,
3501 overwash and inundation of barrier islands. In *Proceedings of the 33rd International*
3502 *Conference on Coastal Engineering*, Santander, Spain.
- 3503 Hoonhout, B. M., van Thiel de Vries, J. S. M., Curto, V., and Stive, M. J. F. (2014b).
3504 Monitoring supply limiting conditions using imageing techniques. In *Proceedings of*
3505 *the 34th International Conference on Coastal Engineering*.
- 3506 Horikawa, K., Hotta, S., Kubota, S., and Katori, S. (1983). On the sand transport rate
3507 by wind on a beach. *Coastal Engineering in Japan*, 26:101–120.
- 3508 Hotta, S., Kubota, S., Katori, S., and Horikawa, K. (1984). Sand transport by wind on
3509 a wet sand beach. In *Proceedings of the 19th Conference on Coastal Engineering*, pages
3510 1264–1281, Houston, TX. ASCE.
- 3511 Houser, C. (2009). Synchronization of transport and supply in beach-dune interaction.
3512 *Progress in Physical Geography*, 33(6):733–746. doi:[10.1177/0309133309350120](https://doi.org/10.1177/0309133309350120).
- 3513 Houser, C. and Ellis, J. (2013). Beach and dune interaction. *Treatise on geomorphology*.
3514 Academic, San Diego. doi:[10.1016/B978-0-12-374739-6.00283-9](https://doi.org/10.1016/B978-0-12-374739-6.00283-9).
- 3515 Howard, A. D. (1977). Effect of slope on the threshold of motion and its application
3516 to orientation of wind ripples. *Geological Society of America Bulletin*, 88(6):853–856.
3517 doi:[10.1130/0016-7606\(1977\)88;853:EOSOTT;2.0.CO;2](https://doi.org/10.1130/0016-7606(1977)88;853:EOSOTT;2.0.CO;2).
- 3518 Hsu, S.-A. (1971). Wind stress criteria in eolian sand transport. *Journal of Geophysical*
3519 *Research*, 76(36):8684–8686.
- 3520 Hugenholtz, C. H. and Barchyn, T. E. (2011). Laboratory and field performance of a
3521 laser particle counter for measuring aeolian sand transport. *Journal of Geophysical*
3522 *Research*, 116(F1). doi:[10.1029/2010JF001822](https://doi.org/10.1029/2010JF001822). F01010.
- 3523 Iversen, J. D. and Rasmussen, K. R. (2006). The effect of surface slope on saltation
3524 threshold. *Sedimentology*, 41(4):721–728. doi:[10.1111/j.1365-3091.1994.tb01419.x](https://doi.org/10.1111/j.1365-3091.1994.tb01419.x).
- 3525 Jackson, D. W. T. and Cooper, J. A. G. (1999). Beach fetch distance and aeolian sedi-
3526 ment transport. *Sedimentology*, 46:517–522. doi:[10.1046/j.1365-3091.1999.00228.x](https://doi.org/10.1046/j.1365-3091.1999.00228.x).
- 3527 Jackson, N. L. and Nordstrom, K. F. (1998). Aeolian transport of sediment on a
3528 beach during and after rainfall, wildwood, nj, usa. *Geomorphology*, 22(2):151–157.
3529 doi:[10.1016/S0169-555X\(97\)00065-2](https://doi.org/10.1016/S0169-555X(97)00065-2).
- 3530 Jackson, N. L. and Nordstrom, K. F. (2011). Aeolian sediment transport and
3531 landforms in managed coastal systems: a review. *Aeolian research*, 3(2):181–196.
3532 doi:[10.1016/j.aeolia.2011.03.011](https://doi.org/10.1016/j.aeolia.2011.03.011).
- 3533 Jackson, N. L., Nordstrom, K. F., Saini, S., and Smith, D. R. (2010). Effects of nour-
3534 ishment on the form and function of an estuarine beach. *Ecological Engineering*,
3535 36(12):1709–1718. doi:[10.1016/j.ecoleng.2010.07.016](https://doi.org/10.1016/j.ecoleng.2010.07.016).

- 3536 Johnson, J. W. (1965). Sand movement on coastal dunes. Technical Report 570, Symp.
3537 3, Paper no. 75, U.S. Department of Agriculture, Washington. pp 747-755.
- 3538 Kawamura, R. (1951). Study of sand movement by wind. Technical Report HEL-2-8,
3539 Hydraulics Engineering Laboratory, University of California, Berkeley.
- 3540 King, C. A. M. (1951). Depth of disturbance of sand on sea beaches by waves. *Journal
3541 of Sedimentary Petrology*, 21(3):131–140.
- 3542 King, J., Nickling, W. G., and Gillies, J. A. (2005). Representation of vegeta-
3543 tion and other nonerodible elements in aeolian shear stress partitioning mod-
3544 els for predicting transport threshold. *Journal of Geophysical Research*, 110(F4).
3545 doi:[10.1029/2004JF000281](https://doi.org/10.1029/2004JF000281). F04015.
- 3546 Kocurek, G. and Lancaster, N. (1999). Aeolian system sediment state: the-
3547 ory and mojave desert kelso dune field example. *Sedimentology*, 46(3):505–515.
3548 doi:[10.1046/j.1365-3091.1999.00227.x](https://doi.org/10.1046/j.1365-3091.1999.00227.x).
- 3549 Kroy, K., Sauermann, G., and Herrmann, H. J. (2002). Minimal model for sand dunes.
3550 *Physical Review Letters*, 88(5):054301. doi:[10.1103/PhysRevLett.88.054301](https://doi.org/10.1103/PhysRevLett.88.054301).
- 3551 Lancaster, N. and Baas, A. (1998). Influence of vegetation cover on sand transport by
3552 wind: field studies at owens lake, california. *Earth Surface Processes and Landforms*,
3553 23(1):69–82.
- 3554 Lettau, K. and Lettau, H. (1978). Experimental and micrometeorological field studies
3555 of dune migration.
- 3556 Li, J., Okin, G. S., Herrick, J. E., Belnap, J., Miller, M. E., Vest, K., and Draut, A. E.
3557 (2013). Evaluation of a new model of aeolian transport in the presence of vegetation.
3558 *Journal of Geophysical Research*, 118(1):288–306. doi:[10.1002/jgrf.20040](https://doi.org/10.1002/jgrf.20040).
- 3559 Lynch, K., Jackson, D. W., and Cooper, J. A. G. (2016). The fetch effect on aeolian
3560 sediment transport on a sandy beach: a case study from magilligan strand, northern
3561 ireland. *Earth Surface Processes and Landforms*. doi:[10.1002/esp.3930](https://doi.org/10.1002/esp.3930).
- 3562 Lynch, K., Jackson, D. W. T., and Cooper, J. A. G. (2008). Aeolian fetch distance
3563 and secondary airflow effects: the influence of micro-scale variables on meso-
3564 scale foredune development. *Earth Surface Processes and Landforms*, 33(7):991–1005.
3565 doi:[10.1002/esp.1582](https://doi.org/10.1002/esp.1582).
- 3566 Martin, R. L. and Kok, J. F. (2016). Field measurements demonstrate distinct initiation
3567 and cessation thresholds governing aeolian sediment transport flux. Submitted.
- 3568 Masselink, G., Auger, N., Russell, P., and O'Hare, T. (2007). Short-term morpholog-
3569 ical change and sediment dynamics in the intertidal zone of a macrotidal beach.
3570 *Sedimentology*, 54:39–53. doi:[10.1111/j.1365-3091.2006.00825.x](https://doi.org/10.1111/j.1365-3091.2006.00825.x).
- 3571 McKenna Neuman, C., Li, B., and Nash, D. (2012). Micro-topographic analysis of
3572 shell pavements formed by aeolian transport in a wind tunnel simulation. *Journal
3573 of Geophysical Research*, 117(F4). doi:[10.1029/2012JF002381](https://doi.org/10.1029/2012JF002381). F04003.

- 3574 McKenna Neuman, C. and Nickling, W. (1995). Aeolian sediment flux decay: Non-
3575 linear behaviour on developing deflation lag surfaces. *Earth Surface Processes and*
3576 *Landforms*, 20(5):423–435.
- 3577 McKenna Neuman, C. and Sanderson, S. (2008). Humidity control of par-
3578 ticle emissions in aeolian systems. *Journal of Geophysical Research*, 113(F2).
3579 doi:[10.1029/2007JF000780](https://doi.org/10.1029/2007JF000780). F02S14.
- 3580 Min. V&W (1990). A new coastal defence policy for the netherlands. Rijkswaterstaat.
- 3581 Namikas, S. L., Edwards, B. L., Bitton, M. C. A., Booth, J. L., and Zhu, Y. (2010).
3582 Temporal and spatial variabilities in the surface moisture content of a fine-grained
3583 beach. *Geomorphology*, 114:303–310. doi:[10.1016/j.geomorph.2009.07.011](https://doi.org/10.1016/j.geomorph.2009.07.011).
- 3584 Nickling, W. and McKenna Neuman, C. (1995). Development of deflation lag surfaces.
3585 *Sedimentology*, 42(3):403–414.
- 3586 Nickling, W. G. and Ecclestone, M. (1981). The effects of soluble salts on the threshold
3587 shear velocity of fine sand. *Sedimentology*, 28:505–510.
- 3588 Ojeda, E., Ruessink, B., and Guillen, J. (2008). Morphodynamic response of a two-
3589 barred beach to a shoreface nourishment. *Coastal Engineering*, 55(12):1185–1196.
3590 doi:[10.1016/j.coastaleng.2008.05.006](https://doi.org/10.1016/j.coastaleng.2008.05.006).
- 3591 Okin, G. S. (2008). A new model of wind erosion in the presence of vegetation. *Journal*
3592 *of Geophysical Research*, 113(F2). doi:[10.1029/2007JF000758](https://doi.org/10.1029/2007JF000758). F02S10.
- 3593 Owen, P. R. (1964). Saltation of uniform grains in air. *J. Fluid Mech*, 20(2):225–242.
- 3594 Peckham, S. D., Hutton, E. W. H., and Norris, B. (2013). A component-based approach
3595 to integrated modeling in the geosciences: The design of CSDMS. *Computers and*
3596 *Geosciences*, 53:3–12. doi:[10.1016/j.cageo.2012.04.002](https://doi.org/10.1016/j.cageo.2012.04.002).
- 3597 Pye, K. and Tsoar, H. (1990). *Aeolian Sand and Sand Dunes*. Unwin Hyman, London.
- 3598 Raupach, M., Gillette, D., and Leys, J. (1993). The effect of roughness elements on
3599 wind erosion threshold. *Journal of Geophysical Research: Atmospheres*, 98(D2):3023–
3600 3029. doi:[10.1029/92JD01922](https://doi.org/10.1029/92JD01922).
- 3601 Reniers, A., Gallagher, E., MacMahan, J., Brown, J., Rooijen, A., Thiel de Vries, J., and
3602 Prooijen, B. (2013). Observations and modeling of steep-beach grain-size variability.
3603 *Journal of Geophysical Research: Oceans*, 118(2):577–591.
- 3604 Roelvink, J. A., Reniers, A., van Dongeren, A. P., van Thiel de Vries, J.
3605 S. M., McCall, R. T., and Lescinski, J. (2009). Modelling storm impacts
3606 on beaches, dunes and barrier islands. *Coastal Engineering*, 56(11):1133–1152.
3607 doi:[10.1016/j.coastaleng.2009.08.006](https://doi.org/10.1016/j.coastaleng.2009.08.006).
- 3608 Scheidt, S., Ramsey, M., and Lancaster, N. (2010). Determining soil moisture and
3609 sediment availability at white sands dune field, new mexico, from apparent ther-
3610 mal inertia data. *Journal of Geophysical Research*, 115(F2). doi:[10.1029/2009JF001378](https://doi.org/10.1029/2009JF001378).
3611 F02019.

- 3612 Sherman, D. J., Jackson, D. W., Namikas, S. L., and Wang, J. (1998). Wind-
3613 blown sand on beaches: an evaluation of models. *Geomorphology*, 22(2):113–133.
3614 doi:[10.1016/S0169-555X\(97\)00062-7](https://doi.org/10.1016/S0169-555X(97)00062-7).
- 3615 Sherman, D. J. and Li, B. (2012). Predicting aeolian sand transport rates: a reevaluation
3616 of models. *Aeolian Research*, 3(4):371–378. doi:[10.1016/j.aeolia.2011.06.002](https://doi.org/10.1016/j.aeolia.2011.06.002).
- 3617 Shuttleworth, W. J. (1993). Evaporation. In Maidment, D. R., editor, *Handbook of
3618 Hydrology*, pages 4.1–4.53. McGraw-Hill, New York.
- 3619 Sørensen, M. (2004). On the rate of aeolian sand transport. *Geomorphology*, 59(1):53–62.
- 3620 Spearman, C. (1904). The proof and measurement of association between two things.
3621 *American Journal of Psychology*, 15:72–101. doi:[10.2307/1412159](https://doi.org/10.2307/1412159).
- 3622 Stive, M. J. F., de Schipper, M. A., Luijendijk, A. P., Aarninkhof, S. G. J., van
3623 Gelder-Maas, C., van Thiel de Vries, J. S. M., de Vries, S., Henriquez, M.,
3624 Marx, S., and Ranasinghe, R. (2013). A new alternative to saving our beaches
3625 from sea-level rise: the Sand Engine. *Journal of Coastal Research*, 29(5):1001–1008.
3626 doi:[10.2112/JCOASTRES-D-13-00070.1](https://doi.org/10.2112/JCOASTRES-D-13-00070.1).
- 3627 Stockdon, H. F., Holman, R. A., Howd, P. A., and Sallenger, A. H. (2006). Empirical
3628 parameterization of setup, swash, and runup. *Coastal engineering*, 53(7):573–588.
3629 doi:[10.1016/j.coastaleng.2005.12.005](https://doi.org/10.1016/j.coastaleng.2005.12.005).
- 3630 Stout, J. E. (2004). A method for establishing the critical threshold for aeolian transport
3631 in the field. *Earth Surface Processes and Landforms*, 29(10):1195–1207.
- 3632 Tan, L., Zhang, W., Qu, J., Zhang, K., An, Z., and Wang, X. (2013). Ae-
3633 olian sand transport over gobi with different gravel coverages under limited
3634 sand supply: a mobile wind tunnel investigation. *Aeolian Research*, 11:67–74.
3635 doi:[10.1016/j.aeolia.2013.10.003](https://doi.org/10.1016/j.aeolia.2013.10.003).
- 3636 Turpin, C., Badr, T., and Harion, J. L. (2010). Numerical modelling of aeolian ero-
3637 sion over rough surfaces. *Earth Surface Processes and Landforms*, 35(12):1418–1429.
3638 doi:[10.1002/esp.1980](https://doi.org/10.1002/esp.1980).
- 3639 Udo, K., Kuriyama, Y., and Jackson, D. W. T. (2008). Observations of wind-blown sand
3640 under various meteorological conditions at a beach. *Journal of Geophysical Research*,
3641 113(F4). doi:[10.1029/2007JF000936](https://doi.org/10.1029/2007JF000936). F04008.
- 3642 van der Wal, D. (1998). The impact of the grain-size distribution of nourishment sand
3643 on aeolian sand transport. *Journal of Coastal Research*, pages 620–631.
- 3644 van der Wal, D. (2000). Grain-size-selective aeolian sand transport on a nourished
3645 beach. *Journal of Coastal Research*, pages 896–908.
- 3646 van Genuchten, M. T. (1978). Mass transport in saturated-unsaturated media: one-
3647 dimensional solutions. Technical Report Research Report No. 78-WR-11, Univ.
3648 Princeton, NJ. Water Resources Program.

- 3649 Van Slobbe, E., De Vriend, H., Aarninkhof, S., Lulofs, K., De Vries, M., and Dircke, P.
3650 (2013). Building with nature: in search of resilient storm surge protection strategies.
3651 *Natural hazards*, 65(1):947–966. doi:[10.1007/s11069-012-0342-y](https://doi.org/10.1007/s11069-012-0342-y).
- 3652 Šimůnek, J., Šejna, M., and van Genuchten, M. T. (1998). *The HYDRUS-1D software*
3653 *package for simulating the one-dimensional movement of water, heat, and multiple solutes*
3654 *in variably-saturated media*. International Ground Water Modeling Center, Colorado
3655 School of Mines, Golden, Colorado, version 1.0. igwmc - tps - 70 edition. 186pp.
- 3656 Walstra, D. J. R. (2016). *On the anatomy of nearshore sandbars: a systematic exposition*
3657 *of inter-annual sandbar dynamics*. PhD thesis, Delft University of Technology, Delft.
3658 doi:[10.4233/uuid:3f86bf04-c6af-486f-b972-bd228d84ebcd](https://doi.org/10.4233/uuid:3f86bf04-c6af-486f-b972-bd228d84ebcd).
- 3659 Waterman, R. E. (2010). *Integrated coastal policy via Building with Nature*. TU Delft, Delft
3660 University of Technology.
- 3661 Weng, W. S., Hunt, J. C. R., Carruthers, D. J., Warren, A., and Wiggs, G. F. S. (1991).
3662 Air flow and sand transport over sand-dunes. *Acta Mechanica*, 2:1–22.
3663 Wiggs, G. F. S., Baird, A. J., and Atherton, R. J. (2004). The dynamic effects of mois-
3664 ture on the entrainment and transport of sand by wind. *Geomorphology*, 59:13–30.
3665 doi:[10.1016/j.geomorph.2003.09.002](https://doi.org/10.1016/j.geomorph.2003.09.002).
- 3666 Williams, A. T. (1971). An analysis of some factors involved in the depth of distur-
3667 bance of beach sand by waves. *Marine Geology*, 11(3):145–158. doi:[10.1016/0025-3227\(71\)90003-X](https://doi.org/10.1016/0025-3227(71)90003-X).

3669 ACKNOWLEDGMENTS

3670 In the spring of 2012 I was still convinced that I would never engage in a PhD research
3671 as it would be too specialized, too enduring and too lonely. Four years later, I learned
3672 that an enduring (but hardly lonely) specialization fits me rather well and is an ex-
3673 perience I would not want to have missed. Now I'm indebted to Jaap for bringing
3674 the NEMO proposal to my attention. To Roos for convincing me to apply for a PhD
3675 position after I had been rambling on about the proposal for weeks, apparently. She
3676 was also the one that finally made me accept that it was time to wrap up and finish. I
3677 thank Jaap and Sierd for their enthusiastic supervision. I thank Marcel for accepting
3678 me on the NEMO project and providing me once again with the freedom to explore.
3679 I thank Deltares for their generous support in this personal endeavor and Noor and
3680 Jolijn for not keeping me up too many nights in the final year of my research.

3681 I have a special memory towards the six week MEGAPEX field campaign at the
3682 Sand Motor, which was a surrealistic experience that illustrates how a group of
3683 overly enthusiastic scientists is able to built a beautiful scientific dataset from a huge
3684 pile of sand. Either by Meagan's state-of-the-art equipment that apparently require
3685 American-sized *Freedom Poles* for appropriate mounting, or by the elegance of simple
3686 solutions to complex problems, like Nick "Topo is My Life" Cohn walking his daily
3687 transects accumulating to the equivalent of a pilgrimage to Santiago de Compostela. I
3688 will not easily forget the first time Sierd and I deployed the nails as low-tech measure
3689 for micro-topographic changes over a single tidal cycle. Due to unfortunate planning
3690 we had to measure and retrieve the first batch nails (4 cm long, 3 mm thick) in the
3691 middle of the night in pitch-dark. Waving our torches over the beach it took us only
3692 about a few minutes to find a beautiful array of nails protruding proudly about 1
3693 cm from the bed. Priceless! We learned so much these weeks. I thank the entire
3694 MEGAPEX team for this exhausting experience, the assistance with our laborious sub-
3695 aerial measurements, the proliferation of American flags at the Sand Motor (U-S-A!)
3696 and the free pumpkins.

3697 Except for the six weeks at the Sand Motor, I shared a room at the Faculty of
3698 Civil Engineering with my fellow NEMO promovendi Saulo and Bas, and Max, our
3699 adopted son from the NatureCoast project. It has been a highly fruitful and challeng-
3700 ing environment to work in, despite our research was only superficially related. I
3701 much appreciated the discussions on what we all could do in our newly obtained and
3702 privileged position: the utter necessity of face recognition in our room, the benefits of
3703 having our own 4x4 and the possible improvements to our typical Dutch bread-and-
3704 cheese lunch. But soon we found ourselves juggling with an enormous amount of
3705 actual scientific ideas, international co-operations, measurement equipment stacked
3706 around our desks and an abundance of data. Scientific research appeared to be a
3707 very practical daily activity. Discussions started to shift accordingly: how to deploy
3708 equipment in the field, how to solder your own measurement devices, what Python
3709 package will get the most out of your data and when does data analysis become data
3710 torture? Finally, when it occurred to us that the NEMO project had produced more
3711 children than papers, the focus shifted once again to finalizing our research. I much

3712 appreciated the weekly papers & coffee meetings with Saulo regarding our writing
3713 progress. We both needed it.

3714 As said, these four years appeared not to be so lonely after all. Luckily, since the
3715 best ideas arise in conversation. Little pieces that fit together and make you under-
3716 stand. I thank Sierd de Vries, Saulo Meirelles Nunes da Rocha, Max Radermacher, Bas
3717 Huisman, Matthieu de Schipper, Martijn Henriquez, Ronald Brouwer, Marcel Stive,
3718 Jaap van Thiel de Vries, Bert van der Valk, Ad van der Spek, Arjen Luijendijk, Dano
3719 Roelvink, Fedor Baart, Kees den Heijer, Irv Elshoff, Mart Borsboom, Wiepke Jäger, Ad
3720 Reniers, Thom Bogaard, Martine Rutten, Susan Steele, Laurens van der Maaten, Thea
3721 Vuik, Duncan van der Heul, Lianne van der Weerd, Kathelijne Wijnberg, Leonardo
3722 Duarte Campos, Filipe Galiforni Silva, Isaac Williams, Gerben Ruessink, Winnie de
3723 Winter, Pam Hage, Yvonne Smit, Jasper Donker, Timothy Price, Maarten Kleinhans,
3724 Sebastian Huizer, Marc Bierkens, Corjan Nolet, Joep Keijsers, Ate Poortinga, Michel
3725 Riksen, Nick Cohn, Peter Ruggiero, Laura Moore, Orenco Durán, Evan Goldstein,
3726 Edie Gallagher, Daniel Buscombe, Andrew Cooper, Irene Delgado-Fernandez, Robert
3727 Davidson-Arnott, Tom Barchyn, Giovanni Coco, Gerd Masselink, Bonnie Ludka, Mea-
3728 gan Wengrove, Caroline Fredriksson, Bas Arens, Roeland de Zeeuw, Gideon Maillette
3729 de Buy Wenniger, Tom Janssen, Rufus Velhorst, Leon Roessen, Bert Bakker, Jos van
3730 Meurs, Henk Tiggeloven, Giel Hermans, Steve van Herk, Sander de Vree, Frank Kalk-
3731 man, Jaap van Duin and the anonymous reviewers for all the little pieces that made
3732 up this thesis.

3733
3734

Bas Hoonhout
Delft, September 2016

3735 CURRICULUM VITAE

3736 PERSONALIA

Bas Hoonhout

26-06-1983, Amsterdam, Nederland

3737 EDUCATION

1995 – 2001 Montessori Lyceum Amsterdam, VWO Natuur & Techniek (1995-2001)

2002 – 2009 Delft University of Technology, MSc Civil Engineering: Dune Erosion along Curved Coastlines (cum laude)

3738 EMPLOYMENT

2001–2009 Freelance web developer

2009– Deltares

"thesis" — 2016/12/13 — 10:12 — page 134 — #162

3739 PUBLICATIONS

3740 PEER-REVIEWED ARTICLES

- 3741 Hoonhout, B. M. and de Vries, S. (2016d). A process-based model for aeolian sediment
3742 transport and spatiotemporal varying sediment availability. *Journal of Geophysical*
3743 *Research: Earth Surface*. doi:[10.1002/2015JF003692](https://doi.org/10.1002/2015JF003692). 2015JF003692.
- 3744 Hoonhout, B. M. and de Vries, S. (2016a). Aeolian sediment supply at a mega nour-
3745 ishment. *Coastal Engineering*. Submitted.
- 3746 Hoonhout, B. M. and de Vries, S. (2016c). Field measurements on spatial variations in
3747 aeolian sediment availability at the sand motor mega nourishment. *Aeolian Research*.
3748 Submitted.
- 3749 Hoonhout, B. M., Radermacher, M., Baart, F., and Van der Maaten, L. J. P. (2015c). An
3750 automated method for semantic classification of regions in coastal images. *Coastal*
3751 *Engineering*, 105:1–12. doi:[10.1016/j.coastaleng.2015.07.010](https://doi.org/10.1016/j.coastaleng.2015.07.010).
- 3752 Hoonhout, B. M., Baart, F., and Van Thiel de Vries, J. S. M. (2014a). Intertidal beach
3753 classification in infrared images. *Journal of Coastal Research*, SI 66:657–662.

3754 CONFERENCES

- 3755 Hoonhout, B. M., Cohn, N., de Vries, S., Roelvink, J. A., Ruggiero, P., Moore, L. J.,
3756 Durán, O., and Goldstein, E. (2016a). How tides and waves enhance aeolian sedi-
3757 ment transport at the sand motor. In *Proceedings of the 35th International Conference*
3758 *on Coastal Engineering*.
- 3759 Hoonhout, B. M. and de Vries, S. (2016b). Aeolis: A new model for aeolian sediment
3760 supply and transport. In *Proceedings of the NCK-days 2016*.
- 3761 Hoonhout, B. M., Cohn, N., de Vries, S., Roelvink, J. A., Ruggiero, P., Moore, L. J.,
3762 Durán, O., and Goldstein, E. (2016b). How tides and waves enhance aeolian sedi-
3763 ment transport at the sand motor. In *Proceedings of the Ocean Sciences Meeting 2016*.
- 3764 Hoonhout, B. M., de Vries, S., and Cohn, N. (2015a). The influence of spatially varying
3765 supply on coastal aeolian transport: a field experiment. In *Proceedings of Coastal*
3766 *Sediments*, San Diego, USA.
- 3767 Hoonhout, B. M., de Vries, S., and Cohn, N. (2015b). The influence of spatially varying
3768 supply on coastal aeolian transport: A field experiment. In *Proceedings of the NCK-*
3769 *days 2015*.
- 3770 Hoonhout, B. M. and de Vries, S. (2014b). Process-based modeling of supply-limited
3771 aeolian transport in coastal environments. In *Proceedings of the International Confer-*
3772 *ence on Aeolian Research 2014*.

- 3773 Hoonhout, B. M., van Thiel de Vries, J. S. M., Curto, V., and Stive, M. J. F. (2014b).
3774 Monitoring supply limiting conditions using imageing techniques. In *Proceedings*
3775 of the 34th International Conference on Coastal Engineering.
- 3776 Hoonhout, B. M. and de Vries, S. (2014a). Modelling and monitoring of meso-scale
3777 supply-limited aeolian transport. In *Proceedings of the NCK-days 2014*.
- 3778 Hoonhout, B. M., de Vries, S., Baart, F., van Thiel de Vries, J. S. M., van der Weerd, L.,
3779 and Wijnberg, K. M. (2013). Monitoring of beach surface properties with remote
3780 sensing. In *Proceedings of Coastal Dynamics*, Arcachon, France.
- 3781 Hoonhout, B. M. (2013). Monitoring the process of aeolian transport. In *Proceedings of*
3782 the NCK-days 2013.
- 3783 Hoonhout, B. M. and van Thiel de Vries, J. S. M. (2012). Modeling dune erosion,
3784 overwash and inundation of barrier islands. In *Proceedings of the 33rd International*
3785 *Conference on Coastal Engineering*, Santander, Spain.
- 3786 Hoonhout, B. M. and den Heijer, C. (2010). Reliability of dune erosion assessment
3787 along curved coastlines. In *Proceedings of the 32nd International Conference on Coastal*
3788 *Engineering*, Shanghai, China.

3789 SOFTWARE AND DATA

- 3790 Hoonhout, B. M. (2016b). Aeolis v1.1: A process-based model for sim-
3791 ulating availability-limited aeolian sediment transport. GIT repository.
3792 doi:[10.5281/zenodo.58854](https://doi.org/10.5281/zenodo.58854).
- 3793 Hoonhout, B. M. (2016a). Aeolis model setups v2.0. GIT repository.
3794 doi:[10.5281/zenodo.58837](https://doi.org/10.5281/zenodo.58837).
- 3795 Hoonhout, B. M., de Vries, S., and Cohn, N. (2016c). Field measurements on aeo-
3796 lian sediment transport at the sand motor mega nourishment during the megapex
3797 field campaign. OpenDAP server. doi:[10.4121/uuid:3bc3591b-9d9e-4600-8705-5b7eba6aa3ed](https://doi.org/10.4121/uuid:3bc3591b-9d9e-4600-8705-5b7eba6aa3ed).
- 3799 Hoonhout, B. M. and Radermacher, M. (2015b). Flamingo: a coastal image analysis
3800 toolbox. GIT repository. doi:[10.5281/zenodo.14596](https://doi.org/10.5281/zenodo.14596).
- 3801 Hoonhout, B. M. and Radermacher, M. (2015a). Annotated images of the dutch coast.
3802 FTP server. doi:[10.4121/uuid:08400507-4731-4cb2-a7ec-9ed2937db119](https://doi.org/10.4121/uuid:08400507-4731-4cb2-a7ec-9ed2937db119).

3803

3804 COLOPHON

3805 Measurement data presented in this thesis is open-source and can be obtained through
3806 the 4TU.ResearchData initiative at:

3807 data.tu.nl

3808 The AEOLiS model presented in this thesis is open-source and can be obtained through
3809 the OpenEarth GitHub repository at:

3810 github.com/openearth/aeolis-python/

3811 The model schematizations presented in this thesis are open-source and can be ob-
3812 tained through the OpenEarth GitHub repository at:

3813 github.com/openearth/aeolis-models/

3814 The technical documentation of the AEOLiS model can be found at:

3815 aeolis.readthedocs.io

3816 All scripts that are used for analysis of measurement data, model setup and the gen-
3817 eration of figures and tables, including an ANSIBLE playbook that generates this thesis
3818 from raw data, are published through the author's private GitHub repository at:

3819 github.com/hoonhout/phd/

3820 This document was typeset using the typographical look-and-feel `classicthesis` de-
3821 veloped by André Miede.